5-2010

Microfluidic manipulation by AC Electrothermal effect

Meng Lian
The Univ of Tennessee, mlian@utk.edu

To the Graduate Council:

I am submitting herewith a dissertation written by Meng Lian entitled "Microfluidic manipulation by AC Electrothermal effect." I have examined the final electronic copy of this dissertation for form and content and recommend that it be accepted in partial fulfillment of the requirements for the degree of Doctor of Philosophy, with a major in Electrical Engineering.

Jie Wu, Major Professor

We have read this dissertation and recommend its acceptance:

Leon Tolbert, Ethan Farquhar, Frank Guess

Accepted for the Council:

Carolyn R. Hodges

Vice Provost and Dean of the Graduate School

(Original signatures are on file with official student records.)

To the Graduate Council:

I am submitting herewith a dissertation written by Meng Lian entitled "Microfluidic manipulation by AC electrothermal effect." I have examined the final electronic copy of this dissertation for form and content and recommend that it be accepted in partial fulfillment of the requirements for the degree of Doctor of Philosophy, with a major in Electrical Engineering.

Dr. Jie Wu, Major Professor

We have read this dissertation
And recommend its acceptance:

Dr. Leon Tolbert

Dr. Ethan Farquhar

Dr. Frank Guess

Accepted for the Council:

Carolyn R. Hodges
Vice Provost and Dean of the Graduate School

(Original signatures are on file with official student records.)

Microfluidic manipulation by AC electrothermal effect

A Dissertation
Presented for the
Doctor of Philosophy
Degree
The University of Tennessee, Knoxville

Meng Lian

May 2010

Abstract

AC Electrokinetics (ACEK) has attracted much research interest for microfluidic manipulation for the last few years. It shows great potential for functions such as micropumping, mixing and concentrating particles. Most of current ACEK research focuses on AC electroosmosis (ACEO), which is limited to solutions with conductivity less than 0.02 S/m, excluding most biofluidic applications. To solve for this problem, this dissertation seeks to apply AC electrothermal (ACET) effect to manipulate conductive fluids and particles within, and it is among the first demonstration of ACET devices, a particle trap and an ACET micropump. The experiments were conducted using fluid with conductivity of 0.224 S/m that is common in bio-applications and sub-micron particles were concentrated onto electrode surfaces. Such pumping and trapping were demonstrated at low voltages, reaching ~100 um/s for no more than 8 Vrms at 200 kHz. The flow velocity was measured to follow a quartic relationship with applied voltage which is in accordance with theory.

This research also studies ACET effect on low ionic strength microfluidics, since Joule heating is ubiquitous in electrokinetic devices. One contribution is that our study suggested ACET as one possible reason of flow reversal, which has intrigued the researchers in ACEK field. Electrically, a microfluidic cell can be viewed as an impedance network of capacitances and resistors. Heat dissipation in those elements varies with AC frequency and fluid properties. Of importance is the relative heat generation at the electrode/electrolyte interface and in the resistive fluid bulk, which could change the temperature gradient in the device, hence changes the flow direction.

Another contribution of this dissertation is the reaction enhanced ACET micropumping. A dramatic improvement in flow rate over conventional ac micropumps is achieved by introducing a thin fluid layer of high ionic density near the electrodes. Such an ionic layer is produced by superimposing a dc offset on ac signal that induces faradaic reaction. The pumping velocity is much faster with a dc voltage, in some cases by an order of magnitude, reaching a linear velocity of up to 2.5 mm/s with only 5.4Vrms. This discovery presents an exciting opportunity of utilizing ACET effect in microfluidic applications.

Table of Contents

List of Figures

ABBREVIATION AND ACRONYMS

AC	Alternating Current
ACEO	AC Electro-osmosis
ACET	AC Electrothermal
DC	Direct Current
DEP	Di-Electrophoresis
DI	Deionized
EK	Electro-kinetic
EOF	Electroosmosis Flow
ITO	Indium Titanium Oxide
LOC	Lab-On-a-Chip
MEMS	Microelectromechanical systems
μTAS	Micro Total Analysis and System

Chapter 1. Introduction to Microfluidics and Electrokinetics

Microfluidics is a recently emerged research area that is concerned with handling and manipulation of small amount of fluids, usually measured in nano or picoliter. Knowledge from multiple disciplines such as mechanics, chemistry, physics, biotechnology and MEMS (micro-electro-mechanical systems) are applied in microfluidic approaches.

The development of microfluidics started from inkjet printer manufacturing about three decades ago. Small tubes that are less than $100\,\mu m$ in size were designed to generate ink drops. This technique is now adopted in biotechnology to deliver reagents to microscopic reactors and deposit DNA into arrays. With recent advances and innovations, microfluidics has found wide applications in areas of pharmaceutical, life science, biotechnology, public health and even agriculture.

Microfluidic devices offer many attractive benefits for small scale fluid handing and analysis. Reducing device size means reduction of sample and reagent volumes (a few tens or hundreds of nanoliter compared to hundreds of microliter in existing plate assays) which reduces the overall cost. Reactions at small scales happen at a much faster speed due to unique physics at small fluid volumes, providing a timely access for detection/manipulation. Parallel operations are possible which shortens the time for cell sorting, analysis and treatment times. Test chips are often disposable which is important for sterility. Using microfluidic chips allows for a design of closed system and minimizes the chances of chemical exposure and other contaminants. Also microfluidic technologies can also be easily automated to perform routine tasks like sample preparation with little

human intervention. These advantages make it possible to design a miniaturized laboratory on a single chip, namely laboratory-on-a-chip (LOC), where multiple functions including purification, reaction, manipulation, separation and detection can be combined together. Such developments benefits from decreased agent consumption, reduced cost, faster and safer analysis, improved data quality and easy control over process parameters. A typical lab-on-a-chip system include channels, mixers, reservoirs, diffusion chambers, integrated electrodes and pumps, etc (Fig 1-1).

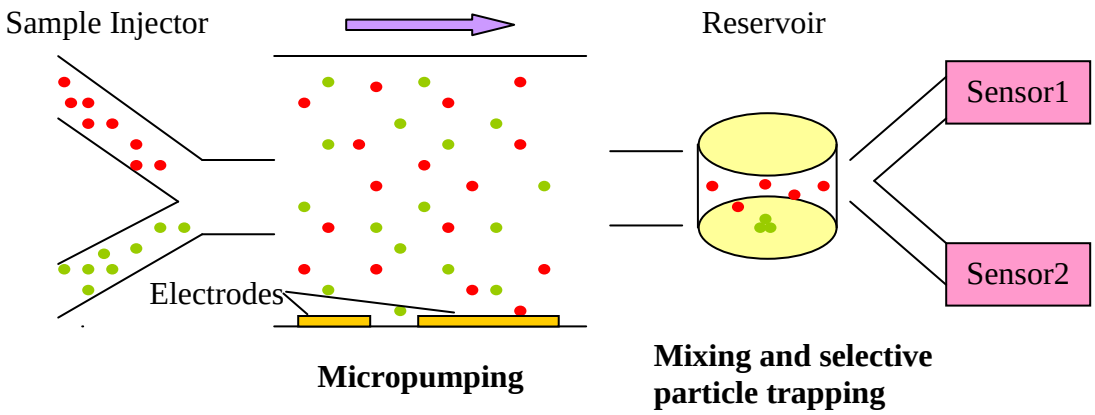

(a)

(b)

Figure 1-1 (a) Schematics of Lab-on-a-chip and (b) a fabricated LOC on glass substrate

Early stage research on microfluidics and its applications were devoted to develop microscale analogues of larger-scale components for handling fluid manipulation in a micro-channel. However, the transition from our macro instruments to their miniature counterparts are far more complicated than merely scaling down. In daily life, conventional pressure driven flow is widely used for fluid pumping. To achieve a fluid flow rate of Q, the required pressure difference ΔP between two ends of conduit is calculated as $\Delta P = \frac{8\mu L Q}{\pi a^4}$, which is inversely proportional to the fourth order of conduit radius a. In small scale devices, a much larger pressure needs to be applied in order to maintain decent flow rates, which is impractical in many cases. Hence, there rises the demand for innovative techniques.

Recent years has witnessed the fast development of Electrokinetics (EK) techniques. These techniques have shown great potentials in fluid manipulation with many advantages and are preferred at microscale. When an electric signal is present, the electric properties of fluid/electrolyte and embedded micro-particles interacts with the applied field, resulting in desired fluid or particle motion. As a comparison to mechanical approaches, EK methods are simple and reliable, especially when developments of micro-fabrication technology allow the integration of electrodes into the fluidic system. An introduction to EK techniques will be given in the following sections.

1.1 Introduction to Electrokinetics

The term “electrokinetic” refers to the motion of particles and fluids as a result of their interactions with external electric fields. With the advances in microfabrication and expanding use of microtechnology in various disciplines, there is increasing interest in

this research topic. Various microfluidic devices have been developed, targeting applications such as manipulation and concentration of cells and bio-molecules.

According to the type of applied electric signal, electrokinetics is classified into DC electrokinetics (DCEK) and AC electrokinetics (ACEK). They both are able to drive liquid flows and particle motions. When a solid is in contact with solution, a thin layer of surface charges builds up at the interface and forms what is called an electric double layer. Surface charges on solid surfaces usually come from hydration of dissolved ions in solution and absorption of neutral molecules. Solids tend to release their ions into the solution as solvated particles, so they often possess a negative surface potential. When a liquid is at the equilibrium state, this double layer serves as a leaky capacitor by blocking the passage of most dc current. In order to induce the flow in the dc case, DCEK relies on the chemical reactions happened at the interface of electrodes and electrolytes at relative high voltages. Charge transfer from electrons in the metal to dissolved ions in the electrolyte take place through faradaic current at the time of reaction. Charged particles in solution (mobile ions) are driven towards the electrode by the electrostatic (Coulomb) force. Such ion motion drags its surrounding solution along by viscosity and generates the fluid flow. A sample schematic of DCEK pump is shown below in Fig 1-2 [1]:

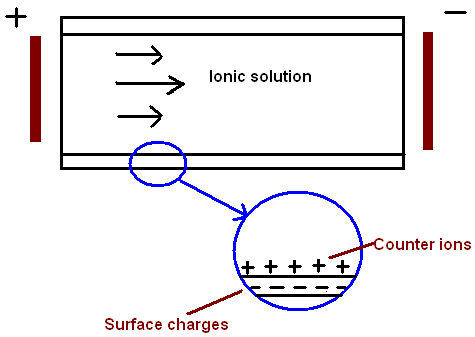

Figure 1-2 Schematic of illustration of a DC electroosmotic pump

Most of the micropumps using DCEK approaches have the configuration similar to Fig 1-2. Two electrodes are placed at the ends of the channel, which is typically of the length scale of centimeters. In order to reach the high field strength that is required to induce flow, a high dc voltage (~kV) is needed. Such a requirement for high voltages and the consequent difficulties in controlling the chemical reaction process lead to undesirable side effects from electrolysis. Unwanted gas bubble can possibly block the conducting path in micro-structure. The fluid reservoirs need to be kept open for the bubble to escape, which becomes a potential source of undesired pressure differences and sample contamination. The degradation of electrodes under such a high voltage is uncontrollable and excessive. These shortcomings prevent DCEK from wider adoption for lab-on-a-chip applications.

Lately, ACEK approaches have been attracting research interest since it alleviates these adverse effects. While DCEK relies on naturally-occurring polarization on passive interfaces, ACEK induces mobile charges and drives those mobile charges with electric field. Electrode damaging due to reactions can be avoided with a combination of low voltage (1-5 Vrms) and sufficient frequency (> 1 kHz) [2] (varies with fluid conductivity). The non-uniform streamlines in ACEK can be used to convect and mix chemical samples. Moreover, ACEK flows are induced by applying voltage to locally deposited electrodes, complex fluid flow pattern can be realized by individually addressing multiple electrodes along the channel. Such properties provide obvious benefits and offer great flexibility when adopting AC techniques into microfluidic and lap-on-a-chip applications.

Major mechanisms of DCEK and ACEK are listed in Fig 1-3. DCEK mainly includes electrophoresis (EP) and electroosmosis (EO). The EP mechanism describes the

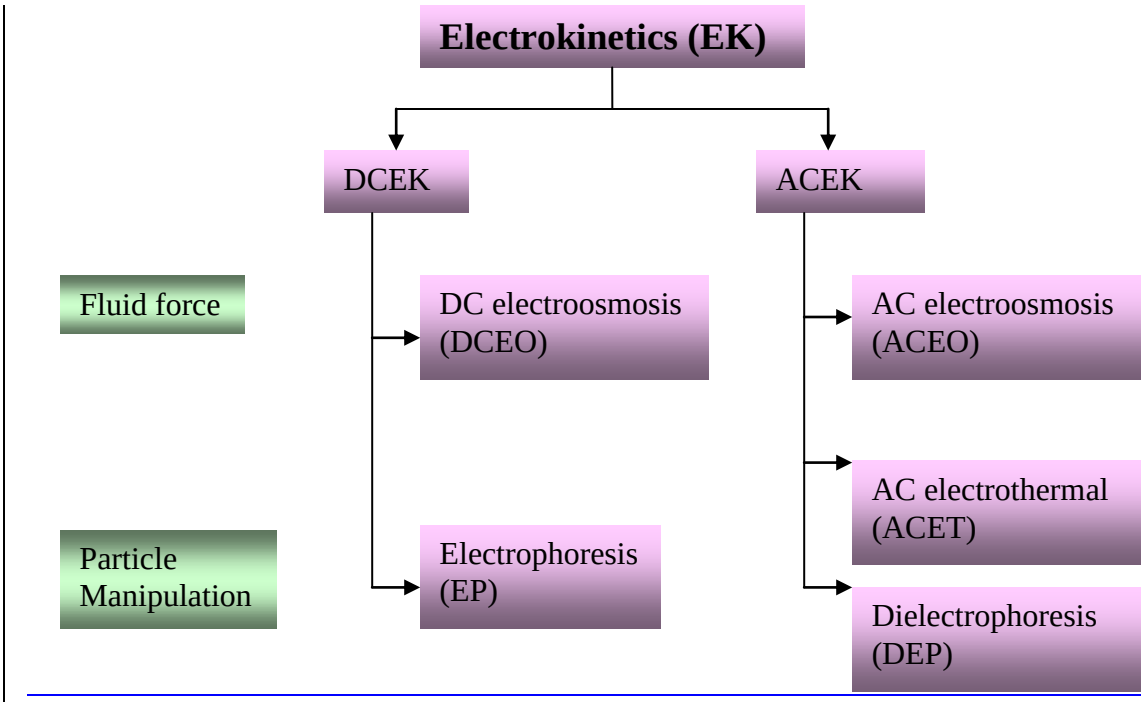

Figure 1-3 Electrokinetics Mechanisms

movement of charged colloidal particles or cells in an electrical field. Its applications in molecular biology, e.g. gel electrophoresis, are used to separate proteins, DNA or RNA on the basis of their electric charge and size [3][4]. People have also found the use of EP in designing electronic display devices which are intended to be alternatives of traditional paper [5] and DNA fingerprinting [6]. Its counterpart in AC EK is called dielectrophoresis (DEP). When there exist differences between the properties of particles and fluid, a dipole is induced at the particle. The interaction between inhomogeneous field and induced particles dipoles gives rise to a net force on the particle.

Another mechanism common to both DCEK and ACEK, is electroosmosis, which represents the fluidic motion in response to the tangential electric field. An electric double layer is formed as soon as solid surfaces are in contact with fluids. The ions in outer part of electric double layer are not tightly bound to the surface. They are mobile

and subject to migration under the influence of an electrical field tangential to the surface. The ion migrations drag the surrounding fluid by viscous force, and henceforward introduce fluid flow. An electroosmosis mechanism has been applied in various microfluidic applications to realize functions like micro-pumping, flow control, particle transport and manipulation. Its literature review will be included in section 1.2.2 and the theoretical detail of electroosmosis will be given in chapter 2.

The electrothermal effect represents another form of electrokinetics. AC current flows through the fluid and the fluid bulk can be viewed as an ideal resistor since it obeys Ohm's rule. Electric energy is consumed by resistive fluid as electric current flow through and transformed into heat (known as Joule heating). This heating process is uneven across different areas of fluid bulk. It introduces temperature gradients within fluid and modifies the local conductivity and permittivity distribution. The perturbation of charge distribution follows and net charges are generated. The Coulomb force on these net charges induces the fluid flow. Highly conductive solution is more favored for the application of ACET force because of the larger current flowing through.

1.2 Literature Review

Micropumping is one of the fundamental functions for fluid handling in micro-devices. Several extensive reviews of micropumping techniques are available [1] [5][6][7] with different emphases of applications. According to these reviews, micropumps are divided into two categories. Mechanical displacement micropumps exert oscillatory or rotational or reciprocating forces on the working fluid through a moving solid-fluid or fluid-fluid boundary. Electricity is applied to mechanical pumps usually for

the purpose of producing deformation of mechanical component and pressure difference in system. Electrokinetic micropumps, on the other hand, provide a direct energy transfer for pumping and generate a steady fluid flow by constant addition of electric signal. Section 1.2.1 reviews the non-electrokinetic methods and techniques related to electrokinetics are discussed in section 1.2.2.

1.2.1 Micropumping using non-electrokinetic approaches

A significant driving force for research on micropumps is the integration of a pumping mechanism in the micro total analysis system (μtas). A wide variety of technologies have been developed for pumping liquids while reducing the total pump volume.

The mechanical micropumps utilize moving parts to displace fluid, such as vibrating diaphragms and check valves, to convert electric energy into mechanical motions. Early stage designs of mechanical micropumps are basically microscale version of known principles from the macro scale. The pressure differences are generated by actuators to drive the fluid. One early design of mechanical pumps by [8] consists of a toothed gear in a fluidic chamber with inlets and outlets (Fig 1-4a). The fluid is entrapped between teeth and transported from inlet to outlet port. An improvement to the rotating pump is the diaphragm displacement pump. These kinds of pump have two modes. At the expansion stroke, the diaphragm deflects, expanding the fluid chamber and decreasing the chamber pressure. The fluid is “sucked” into the chamber from inlet valve. At the compression stoke, the diaphragm deflection is added at the opposite direction to compress the chamber size. The fluid is pumped due to the pressure difference between inside the

chamber and at outlet valve. Fig 1-4b and 1-4c shows the sample schematics for diaphragm pumps.

Various actuation mechanisms have been used in vibrating diaphragm pumps, include piezoelectric [10] [11] [12] [13], electrostatic [14] [15], electromagnetic [16] and thermo-pneumatic [17]. Piezoelectric materials generate an internal mechanical stress in the presence of an applied electric potential. This kind of micropump has piezoelectric materials deposited on the diaphragm for actuation and the applied AC voltage controls the open/close of check valve by polarity change. The electrostatic actuation employs the use of electrostatic forces generated between a counter electrode and diaphragm membrane. The electromagnetic actuation generally consists of a permanent magnet attached to a diaphragm. Lorentz force is produced when current flows through. The fluid

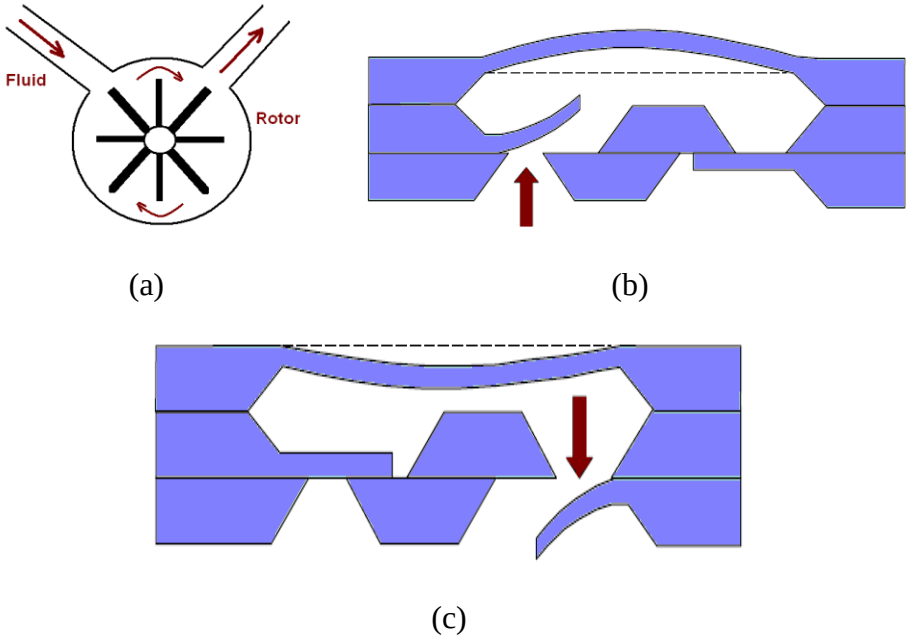

Figure 1-4 Schematics of rotary pumps (a) and diaphragm pumps (b) in suction mode (c) in compression mode [7]

is pumped towards the direction perpendicular to both electric and magnetic field. The thermal-pneumatic actuation involves the volume expansion or induced stress of a material in response to applied heat [10].

The above micropumps used check valve to control flow directions. One universal problem of using check valves in pump designs is fluid leaking. They typically exhibit poor long term reliability, as well as complex multilayer fabrication processes. There exists another mechanical pump called peristaltic pump [18]. Its actuation mechanism is similar to pumps above which utilize actuator deflection to produce pressure variation between inside and outside of fluidic chamber. The difference is that peristaltic pumps usually have three or more fluidic chambers and they do not require passive valves for the flow rectification. The peristaltic motion of a series of actuators is used to squeeze the fluid into desired direction. Flow rate of 100 $\mu l / \min$ was obtained when connected with an 80V voltage source. Fig 1-5 gives an illustration of the peristaltic micropumps.

Despite some success in prototyping diaphragm-involved mechanical micropumps, they have many undesired features for practical use in today's lab-on-a-chip technology.

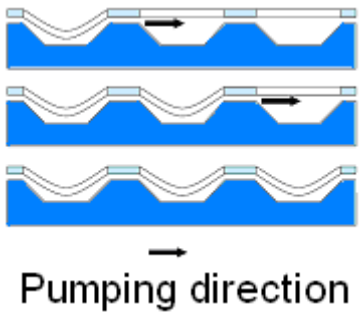

Figure 1-5 Schematic of peristaltic micropump [7]

Diaphragm micropumps usually are associated with large size, valve leakage, high power consumption, low reliability and difficult 3D fabrications. With emerging nanotechnology and biochemical research, precise handling of small volume of fluid (~nanoliter) becomes more and more important. Non-mechanical micropumps are investigated to further scale down the microfluidic devices. One type of non-mechanical micropumps utilizes phase change of working medium. A representative example is bubble pump, in which bubbles are generated inside the pumping chamber to displace the fluid by heating or electrochemical method. Ref. [19] presented a valveless micropump using traversing vapor bubbles. A number of heating modules were placed across the pumping channel and asymmetric heating process was controlled by switching on and off these heating modules. The problem of fluid slipping past the bubbles seems to be insignificant according to the author. The flow rate of $0.5\,nl/\min$ was measure at 23V of AC signal. The power assumption is however as high as 62mW per heater.

The electrowetting phenomenon was also utilized as an actuation mechanism for micropumps. It is classified into the electric micropump category since surface tension difference arisen from charge redistribution upon applied potential is responsible for the droplet movement. The fluid pumping is realized by advance of droplet instead of continuous fluid flow in electrowetting pumps. The presence of electric field in solution results in electrical stress on the droplet and a change in the wetting properties of a droplet of fluid on substrate. The surface tension is reduced and hence decreases the contact angle of electrolyte droplet. A number of studies [20][21] show liquid fronts can be driven at speeds up to ~25 cm/s, and multiple liquid droplets of volumes down to ~1 nanoliter can be dispensed from microliter volumes. This technique was adopted for

lab-on-a-chip applications [22] [23] [24], typically with a series of individual addressable electrodes. However, the factors of large droplet size, high activation voltage and water evaporation need to be taken into consideration in practice. Also one thing needs to mention is that electrowetting mechanism is a droplet manipulation technique. It does not produce continuous flow. Once the fluid passes, the surface is wet and pumping stops. The illustration of bubble pump and electrowetting pump is shown in Fig 1-6b.

1.2.2 Electrokinetic Approaches

The previous sections reviewed the current non-electrokinetic approaches of micropumping. There are many issues with mechanical pumps that need to be solved prior to the application in LOC devices. For instance, the power consumption is problematic for piezoelectric (high required voltages) and thermapneumatic (low

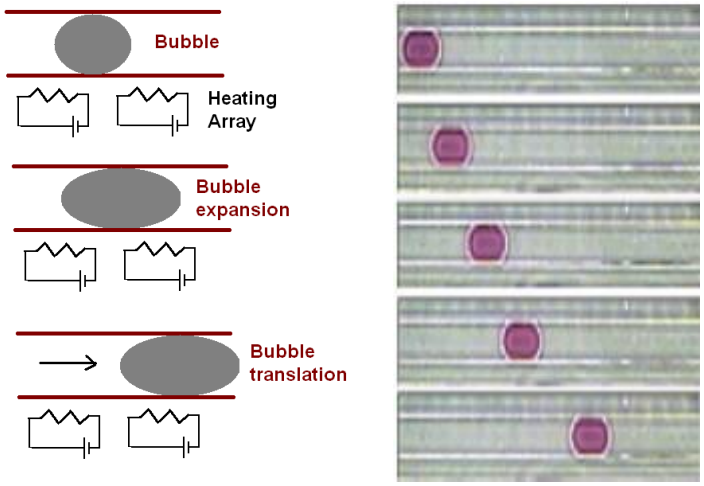

(a) (b)

Figure 1-6 Illustration of bubble pump (a) and sequence of droplet movement with electro-wetting (b) ([25]).

frequencies only) micropumps. Disadvantages for electrostatic micropump include small actuation strokes and long term degradation of performance and precision control of bubble pumps are difficult to realize.

For automated total analysis system (μTAS), the reduction in length scale leads to dominance of viscous force. The inertia of fluid mass becomes insignificant. Reynolds number, defined as the ratio between inertia force to viscous force, is usually small for on chip fluid samples (the range of 10^{-2} to 10^{2}), rendering hydrodynamic pressure insignificant. Most of the biological objects of interest, such as DNA, cells and proteins have a characteristic length from a few hundred nanometers to micrometers, where electrokinetic approaches are especially effective in the domain. With the development of MEMS technology and fabrication methods, the integration of micro scale electrodes into microchannels is a relative simple process. Therefore, electrokinetic forces are ideal choices for manipulation of tiny biological objects and performing fluid operations. This section reviews the current applications of electrokinetic-relative fluid pumping techniques including electroosmosis (EO), electrohydrodynamic (EHD) electrothermal (ET) and pumps.

Electroosmotic Micropump

Electroosmotic micropumps with DC excitation have been demonstrated in many forms [26] [27]. A typical DCEO devices use the design in which anode and cathode is located at the ends of channels (see Fig 1-7 for an example). The surface group at channel wall (in many cases silica or glass capillary) gets deprotonated when wetted, leaving a negatively charged surface. The induced surface charge attracts positively charged ions

and repel negatively charged ion to form the electric double layer. In fluid, the neutral charge density is still maintained. With an applied DC field, the charges experience the Coulomb force and are dragged to the electrodes with opposite polarity. The force experienced by the fluid near channel wall is much higher than in the center due to the higher charge density, resulting in a surface flow. When the channel hydraulic diameter is much larger than double layer thickness, the velocity profile is nearly uniform across the cross-section. Because of the configuration of opposing electrodes in a relative long distance (centimeters), high voltage is required to establish an electric field enough to pump the fluid. [26] described a DCEO pumping device by which high pressure capacities can be achieved in excess of 20 atm at 2kV of applied voltage. Ref. [27] reported a maximum fluid flow rate of 15 $\mu L/\min$ with 1kV DC voltage to a structure where two electrodes were placed at each end of the microchannel (Fig 1-7). The current problems of DCEO pumps are mainly derived from the requirement of high voltage, and consequently bubble generation, pH gradient and chemical reactions at the electrodes. These drawbacks have kept DCEO pumps from enjoying a higher degree of success with μTAS applications.

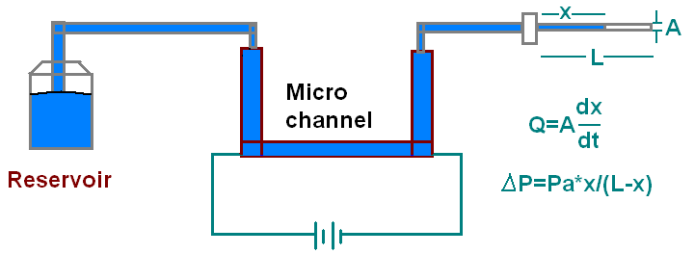

Figure 1-7 Characterization setup of DCEO micropump [26]

ACEO produces fluid flow by surface mobile charge experiencing Coulomb force as well. However, the application of ac signal eliminates the need of faradaic reaction. Electrodes are embedded into the channel without the worries of gas generation and therefore the voltage needed to establish strong field strength is reduced as a result of shortened electrode spacing. Unlike the deprotonation on the channel surface for DCEO flow, mobile charges on electrodes surface in ACEO devices experience stronger Coulomb force and drive the surrounding fluid. In alternating electric field, the sign of charges in double layer switches as a results of electrostatic attraction when electrode polarities change. Since electric field changes the direction at the same time, the direction of Coulomb force maintained to ensure a constant flow direction.

ACEO pumping has been seen in many literatures. For microfluidic systems containing multiple repetitions of paired electrodes, the most common way to induce pumping is to use asymmetric electrodes. Ref. [27] presented an ACEO pump using interdigitated electrode arrays. The electrodes in a pair have unequal widths. One pair of asymmetric electrodes produces a non-symmetric local flow, leading to a global fluid motion in the direction of broken symmetry. The maximum flow rate of 0.001 $\mu L/s$ was achieved with a $10^{-4} M$ KCL solution for 4Vrms of AC signal at 1 kHz. Similar designs in [28] [29] showed recorded peak velocities of 75 $\mu m/s$ at 1.2 Vrms and 450 $\mu m/s$ peak velocity at 2.2 Vrms. A different configuration using traveling wave ACEO micropump was presented in [30] (Fig 1-8 top right). AC signals at 90 degrees phase delay were applied to the electrodes. The regular pumping of dilute KCL solution ($\sigma = 0.0015 S/m$)in the direction of the travelling electric field was maintained for voltage less than 3Vpp at frequency less than 1 kHz. For voltage beyond a certain

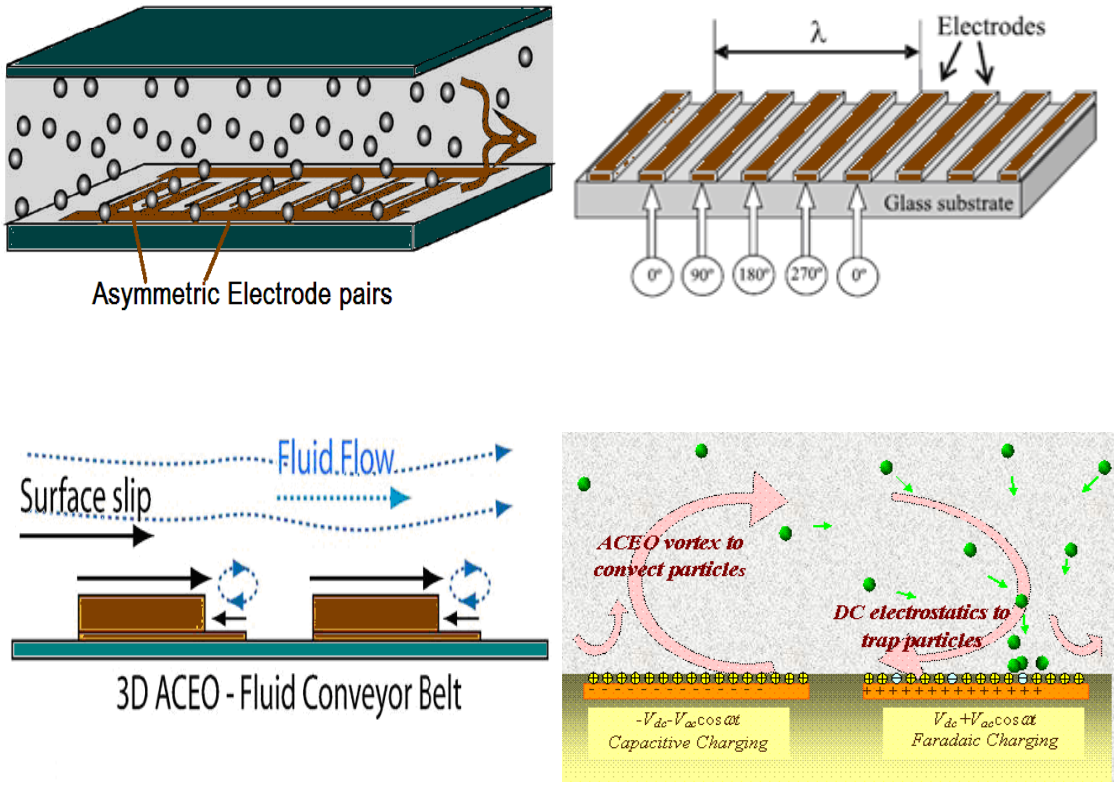

Figure 1-8 Micropump designs using ACEO (Left Upper: Asymmetric [27]; Right Upper: Traveling Wave [30]; Left Lower: 3D [33]; Right Lower: Biased [41])

threshold, the pumping was seen in the reversed direction. Titanium electrodes had a higher threshold voltage (4Vpp) than platinum electrodes (3.5Vpp). Also larger voltage seemed to be required for electrodes with larger gap distances. Another planar design of traveling wave ACEO was later reported in [31]. Given 1.5Vpp, the highest velocity was measured to be 70 $\mu m/s$ at 1 kHz.

Non-planar ACEO pumps have been studied recently both by simulations [32] and experiments [33]. The use of stepped 3D electrode array in these designs attenuated the counter flow vortices and produced a much higher velocity for fluid pumping. The step height in [33] was in the range of 1-5 μm with 5 μm separation between the electrodes.

At 3V peak voltage and 1 kHz signal, the 3D device demonstrated a peak velocity of $420\,\mu m/s$, close to three times of highest velocity $150\,\mu m/s$ in base line device with planar electrodes. [33] also showed non-planar designs with a wider operation range of frequency. Significant velocities span over a frequency range up to 10 kHz.

ACEO flow has been demonstrated to generate surface velocity of 50-100 micron/s by applying AC signals on the order of 1 Vrms with an electrode spacing of 5-25 micron above [88]. However, complexity in fluid dynamics takes place at higher voltages. Fluid reversal was seen in many publications [2] [31] [33]. It was tentatively attributed to faradaic charging of the double layer (i.e. generation of co-ions by electrochemical reaction as opposed to the counter-ion attraction in regular ACEO). Faradaic charging takes place at higher voltage level as compared to the capacitive charging mechanism, which is the mechanism responsible for ACEO devices referenced above. A recent study of faradaic charging in ac electrokinetic shows that significant increase of the amount of surface ions at about 4Vrms for electrodes with 5 microns gaps [34]. Therefore, by intentionally adding dc bias to one of the electrode, one can have capacitive and faradaic charging mechanism happening on different electrodes. A universal ACEO flow is formed because same polarities of ions are induced at anode and cathode surfaces. This "biased" ACEO technique was introduced to generate micropumping in systems with pairs of symmetric electrodes [35] [36]. This new technique has two major advantages. First, the double layer charge density caused by capacitive charging is limited by the equilibrium charge density on electrode surface. At positive biased electrode, the charge density caused by faradaic charging does not have this limitation and it can reach several orders larger in magnitude. Therefore, higher fluid velocity and pumping efficiency can

be achieved with biased ACEO mechanism. Second, ACEO has the capability of depositing particles on specific locations of electrodes, resulting from the formation of counter rotating vortices [36]. This ability is enhanced in biased ACEO by introducing the DC excitation. Most of the colloidal particle and micro-organisms acquire negative charges in solution. They will experience electrophoretic force in addition to viscous force from ACEO induced fluid motion. This makes them more easily being trapped on positive biased electrode.

Both DCEO and ACEO function on fluids with relatively low-ionic strength, i.e., fluid of low conductivity ($10^{-6} \sim 10^{-3} S/m$). For conductive fluids, the increase of ion concentration leads to the suppression of double layer formation. The double layer thickness is smaller which results in lower surface charge densities and pumping capabilities. This property sets limitation of ACEO mechanism in many biological and chemical analyses where highly conductive fluids are often used.

Electrohydrodynamic Micropump

Coulomb force is the main propelling source for fluid motion in EHD pumps. There are many types of EHD pumps which are distinct mainly based on the method by which charged particles are introduced into the fluid. The injection pump, also known as ion-drag pump, uses the interaction of an electric field with electric charges injected into a dielectric field. The electrodes are referred as emitter and collector. Electrochemical reactions cause the injection of free ions into the bulk fluid, which implies the application of high voltage dc signal. [37] fabricated an ion-drag EHD micropump consisting of pairs of planar grids for fluid motion. A flow rate of $250 \mu L/s$ was reported at 800V. [38]

experimented with pairs of coplanar electrodes and [39] compared different coplanar designs and concluded the best pumping efficiency from saw-tooth shaped emitter electrodes. Liquid nitrogen was successfully pumped in a cryogenic cooling micro-system [40]. The numerical analysis on the 3D micropillar electrodes was presented in [41] which showed an increase of pumping performance per higher voltage and shorter electrode gaps. [42] describes an effort of applying a polymer layer of parylene and crosslinked gelatin to protect the gold electrodes from electrolytic aging with a trade-off of pumping efficiency and long term stability. However, the applications of ion-drag pumps are limited by the need of high dc voltage in very dielectric solutions.

The polarization EHD pump utilizes the charges from dissociated species. A dipole is formed on the charge surface. In high electric field region, dipoles possess less energy. Therefore, dipoles in the section of channel bounded by the electrode have lower energy than those outside of the region. A pumping action is then induced. This mechanism has appeared recently in thin film evaporator application [43] and 3d micropump modeling [44]. The illustrations of injection and polarization type of EHD pumps are given in Figure 1-9.

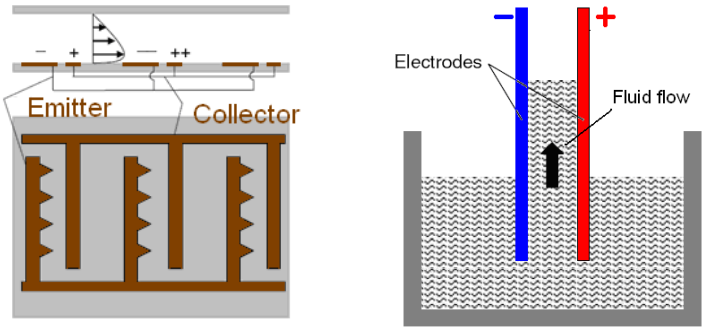

(a) (b)

Figure 1-9 Illustrations of injection (a) and polarization (b) EHD micropumps

Electrothermal Micropump

ACET effect has a short history since it was put forward in early 1990's and not applied to micro-structures until recently. The miniaturization of devices leads to higher energy density being dissipated in the fluid which is suitable to induce temperature gradient (Nevertheless, it was later found that too small a chamber hydraulic diameter would inhibit the formation of ACET flow [45] [46]). Heating the solution results in the change of fluid conductivity and permittivity. Such variations cause the generation of free charges which intends to move under Coulomb force and drag the fluid. The heating process can be either from the fluid Joule heating, or externally applied (e.g. light illumination) [47]. Unlike ACEO which is determined by surface stress, ACET exerts volume force to the fluid bulk and obeys no-slip boundary condition. A sample picture is given in Fig 1-10.

Early on, ACET pumps used travelling wave signal to induce the charge and provide time and space varying electric field. One of the attempts was reported by Fuhr in early 1990s, which applied a traveling wave of four-phase signals to drive fluids [48]. A travelling wave frequency as high as 3.1MHz was used in [49]. Ref. [50] studies the

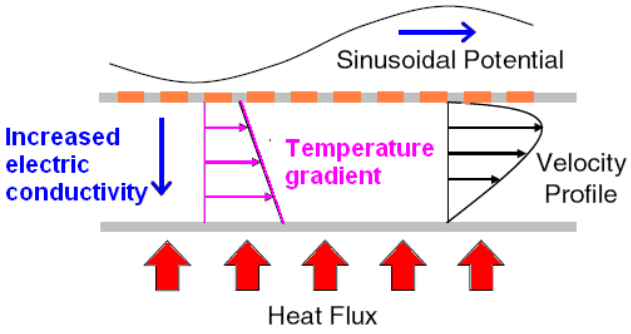

Figure 1-10 Schematics for a travelling wave based pump [7]

ACET effect in the presence of a constant external temperature gradient (strong illumination) in which case electrothermal velocity is linearly proportional to the external thermal gradient. With a solution of $\sigma = 2.5 * 10^{-3}$ S/m, a peak velocity of 80-110 μm/s at 10 Vrms was observed using light illumination. Another application of ACET effect shows the improvement of heterogeneous binding rate up to a factor of 9 with a 10Vrms applied ac signal [51]. Symmetric electrode systems were used for a high conductive buffer of 1S/m. The electrothermal microstirring induces the flow motion and transport streptavidin particles to vicinity of surface and captured by biotin. Similar research efforts applied ACEO/ACET to perform fluid mixing [52]. Over 90% of mixing efficiency was achieved using 7-9 Vrms ac signal with a frequency range of 100-500 kHz in a 0.001S/m diluted potassium chloride solution [52]. The mixing efficiencies were closer to 100% at higher frequencies which indicates the better effectiveness of ACET induced fluid flow.

1.3 Dissertation Outline

Studies in this dissertation first identify the capability of ACET effect on performing fundamental fluid manipulation functions in different electrode designs. The contribution to current knowledge base of ACET study is further illustrated by discovering an ACET flow reversal phenomenon which is due to the reverse of temperature gradient. Different from common practice of applying external heating source to invert temperature distribution, the reversal shown in this dissertation is induced by the natural fluid response to varying operating conditions. At last, a great enhancement of ACET pumping velocity is achieved by superimposing a dc offset on ac signals and inducing faradaic current. The novel technique improves the ACET pumping velocity by up to one order of

magnitude.

The outline of this dissertation is as follows: the introduction to microfluidics and electrokinetics has been given in Chapter 1 as well as the literature review. The next chapter explains the theoretical background about ACEO and ACET including the derivation of forces and calculations of flow magnitude. The particle force DEP is also mentioned. Since formation of electric double layer is the key fundamental property behind electrokinetics and has served as an important basis for ACEK mechanisms, an equivalence electric circuit model based on the surface/fluid property is derived to represent the interaction between electric field and surface/fluid. Chapter 3 presents the experiment results on how the ACET effect is utilized in micropumping and particle trapping. Numerical simulations using finite element methods software are conducted to verify the flow pattern. Chapter 4 offers discussions to the experiment results. We use the equivalence circuit model presented in chapter 2 to support that ACET effect causes the fluid motion. Analytical calculations are performed to rule out the possibilities of other candidates such as ACEO, DEP, buoyancy force, Brownian motion and gravity in generating noticeable flow in experiments. In the follow-up experiments using symmetric electrode system, we observed an interesting flow reversal associated with only one solution among many tested at a particular frequency. The results and discussion are given in chapter 5. Chapter 6 describes a new method which greatly enhances the current ACET-based pumping velocity with the application of a dc bias which induces faradaic charging. Flow response to faradaic current are experimentally recorded and explained with electrolytic theories. With limited dc voltage within the range of $\pm$1.4--2V, the pumping velocity is enhanced with up to one order of magnitude. This enhancement to

regular electrothermal technique fascinates ACET even more in the future applications of lab-on-a-chip design.

Chapter 2. Electrokinetic Mechanisms

As mentioned in Chapter 1, electrokinetics uses interactions between fluid and electric fields to induce fluid flows and manipulate particles. At the interface of electrode and electrolyte, a transition occurs from electronic conduction in the lead wires to ionic conduction in the fluid. Ionic conduction typically involves mass transport. This chapter explains in details two fluid manipulation mechanisms of electrokinetics — electroosmosis (EO) and electrothermal (ET) effect. The particle force dielectrophoresis (DEP) is also mentioned. An equivalence circuit model is derived to provide insights into their differences and how the force magnitudes vary with operating conditions.

2.1 Electrode/electrolyte Interface and Electroosmosis Effect

Dominance of surface effect is one of the key features that distinguish microfluidics from our macro world approaches, which becomes very important as the scale of structures drops down to micrometers. Electroosmosis is a type of surface force. In this section, we start with a brief discussion of electrostatics in electrolytes to lay the basis for ACEO.

When solid is in contact of fluid solution, the surface charge builds up at the interface. In theory, the electric state of a charged surface in fluid solution is determined by the spatial distribution of ions around it. The charge density at the interface of the solid surface and solution is significantly different from that of the fluid bulk. In order for the interface to remain neutral, the surface charge is balanced by the redistribution of ions close to the solid surface, which leads to aggregation of counter-ions at the electrode surface. This can be viewed as the migration of ions with opposite charges from the bulk

to surface area by electrostatic force. The ion aggregation process screens the surface and keeps the fluid bulk electro-neutral, while at the same time, form a capacitive like "relaxed" double layer due to the affinity of charge-determining ions to a surface. Equations below describe the potential distribution within the electric double layer.

For simplification, electrolyte is assumed to be symmetric, meaning that the solution containing two species of ions only different in charge polarities. The solution is also said to be quasi-neutral, i.e., $n_+ - n_- << n_+ + n_-$, where n_+ and n_- are the concentration of positive and negative ions. The ions establish an electrostatic field in solution given by the Poisson equation:

$$\nabla \bullet (\varepsilon_0 \varepsilon_r \nabla \phi) = -e(n_+ - n_-) \tag{2-1}$$

where $\varepsilon_0 = 8.85419 * 10^{-12} C/N \cdot m^2$ is electric constant, ε_r is the relative dielectric constant of the substance and e is the electron charge. The Poisson equation describes the electrostatic potential distribution ϕ with a fixed charge distribution. In equilibrium, the ions respond to the external field via the Boltzmann equation:

$$n_\pm = n_0 \exp(\mp \frac{e\psi}{k_B T}) \tag{2-2}$$

where n_0 is the bulk concentration of salt, ψ is the external field, $k_B = 1.3807 * 10^{-23} JK^{-1}$ is the Boltzmann constant and T is temperature. The Poisson equation is related to Boltzmann distribution when a mean-field assumption is valid. The field ψ to which the ions respond in equilibrium is identical to the field ϕ that ions establish. The ions have no interaction with one another, but rather with the mean field established by the statistical distribution of ions. Therefore, the final Poisson-Boltzmann equation takes the form of:

$$\lambda_d^2 \nabla^2 (\frac{e\phi}{k_B T}) = \sinh(\frac{e\phi}{k_B T}), where, \lambda_d = \sqrt{\frac{\varepsilon k_B T}{2 n_0 e^2}} \quad (2\text{-}2)$$

λ_d is a characteristic length scale over which electrostatic fields are screens by ions and it is named the Debye length. If only a small potential is considered, the equation above can be further simplified as:

$$\lambda_d^2 \nabla^2 \phi = \phi \quad (2\text{-}3)$$

The linearized Poisson-Boltzman equation (Eq (2-4)) represents the Debye-Huckel (DH) approximation in which the double layer capacitance per unit area, $C_{dbl} = \frac{\varepsilon}{\lambda_d}$, is constant. Solutions to the nonlinear PB equation (Eq (2-3)) give rise to a more elaborated double layer model (Gouy-Chapman model), which consists of two layers: a diffuse layer at the outer boundary of double layer and a stern layer at the inside of double layer. Ions in diffuse layer are considered as loosely bounded to surface and subjected to move when experiencing electric forces. The potential is as assumed to decay exponentially in diffuse layer. The stern layer located between surface and diffuse layer contains ions that are tightly attracted and immobilized. Between the stern layer and the diffuse layer is the slip plane beyond which ions have a tendency to "slip" away under the influence of electric field. Further partition divides the stern layer into inner and outer Helmholtz plane. The overall double layer structure is illustrated in Fig 2-1.

As charge density is the product of capacitance and voltage drop, it is important to find the potential drop across double layer, also known as zeta potential ζ. We can derive the magnitude of zeta potential from the general solution of linearized Poisson-Boltzmann equation. If the assumption of λ_D being much smaller than channel

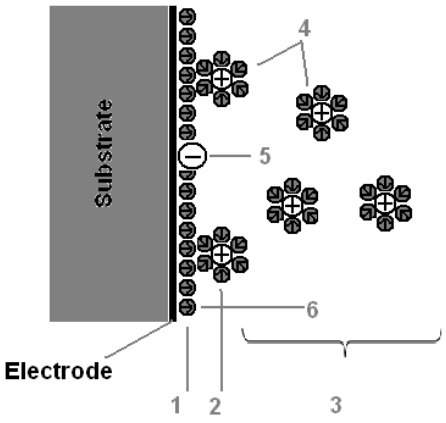

Figure 2-1 The Gouy-chapman-Stern model of electric double layer. 1: inner Helmholtz layer. 2: Outer Helmholtz layer. 3: Diffuse layer. 4: Solvated ions. 5: Absorptive ions. 6: Solvent molecule. [53]

height holds true, the solution to Eq (2-3) is

$$\phi(x) = \phi_0 e^{-x/\lambda_d} \tag{2-4}$$

where ϕ_0 is the surface potential, x is the distance to surface. A typical surface potential distribution is shown in Fig 2-2.

From the formula of Debye length we can see that the Debye length is a property of fluid alone. It does not depend upon application of external voltage. Also, in a medium with strong ionic strength, i.e. high conductivity, the formation of double layer is compressed, reducing the amount of mobile charges in double layer. In general, the Debye length (λ_D) is scaled from 1 to 100 nanometers in aqueous solutions depending on the ionic strength. It typically is much smaller than any geometrical distance relevant for most LOC systems, so bulk solution remains neutral as diffuse charges are confined to thin double layers.

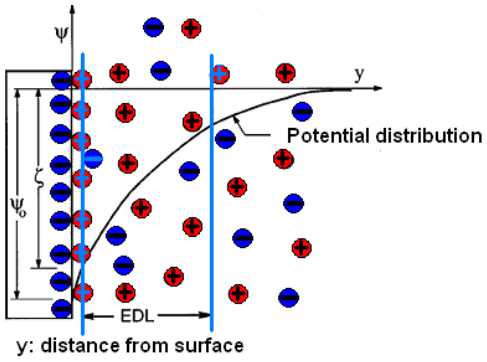

Figure 2-2 The potential distribution in double layer [54]

Electroosmotic flow arises from the interaction between the mobile charges in the diffuse layer and external electric field. Ions in diffuse layer are mobile and will migrate when subject to Coulomb force from tangential component of electric fields. Through viscosity, the ions drag the surrounding liquid ions to move along, inducing electroosmotic flows. The electroosmotic surface velocity is referred as the slip velocity, given by the Helmholtz-Smoluchowski equation:

$$v(y,t) = -\frac{\varepsilon_0 \varepsilon_r}{\eta} \zeta E_t \tag{2-5}$$

where η is the electrolyte viscosity and E_t is the field strength tangential to surface. The Helmholtz equation shows that electroosmosis velocity has no dependency upon the size of channel, unlike pressure driven flow in mechanical micropumps whose velocities scales with square of capillary radius.

As mentioned in Chapter 1, the essential difference between DCEO and ACEO concerns the origin of the diffuse layer charge. In order to let gas bubbles escape from the reaction site in DCEO, the electrodes are placed at ends of microchannels with open reservoir. Since no tangential field is present on electrode surface, DCEO relies on the charge formation from dissolution or absorption on “passive” boundaries. In ACEO, the

fabrication of electrodes on channel walls allows planar electrode designs (meaning that electrodes on channel walls) and the resulting tangential field on electrode surface. The charge density is much higher on electrodes than on passive channel boundaries. Therefore ACEO is far more effective than DCEO since charges are induced by electric field on "active" boundaries, i.e., electrodes. Immediately after a signal is applied, electric field lines intersect with the electrodes. With an ac signal, the polarity of electrodes switches at the second half of a period, deposited ions are expelled from the original location and migrate to the counter electrode. The sign of ions in double layer change in phase with the electric field direction. A steady flow is then maintained for both halves of an ac period as Figure 2-3 shows. More generally speaking, any component of double layer that varies in phase with electric field will give rise to a time-averaged ACEO flow, whereas double layer on passive boundaries in ac case time-averages to zero.

The capacitive charging mechanism of double layer has a charging time of order of $\tau_c = \frac{\varepsilon}{\sigma}\frac{l}{\lambda_D}$ [31], where l is the characteristic length of the system, typically the electrode separation. It indicates that electroosmosis is frequency dependent. When

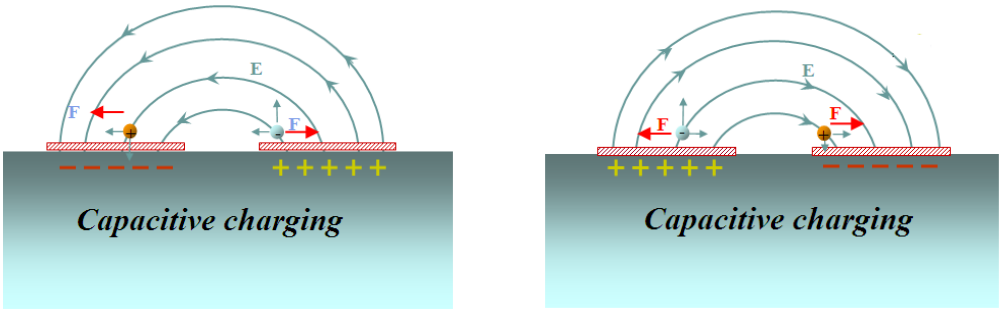

Figure 2-3 Steady ACEO flow is maintained for two halves of a period

$\omega\tau_c << 1$ ($\omega = 2\pi f$ is the radian frequency), the charging process is thorough and surface charges completely screen the electrodes, leaving no tangential field component. On the other hand, when $\omega\tau_c >> 1$, the deficit in time for charges to migrate and deposit on surface hinders the formation of double layer which leads to small zeta potential [55]. Plot of electroosmotic velocity versus frequency is therefore in a bell-shape as seen in many literatures. At frequency lower than the charge relaxation frequency $1/\tau_c$, the zeta potential is equal to that for a capacitance per unit area of value $\frac{\varepsilon_0\varepsilon_r}{\lambda_D}$ in thin double-layer approximation [56].

The ACEO mechanism has a variety of advantages to be applied in LOC devices. Stronger flow than traditional EHD flow is possible because of the higher zeta potential in ACEO. Many ACEO pumps produce 10^2-$10^3\ \mu m/s$ flows for voltage level <5V. Moreover, one can modulate zeta potential through a proper geometry or a gate voltage. A latest publication explores the gate control technique to achieve dynamic flow control [57]. By using soft lithography materials to channel design and applying low gate voltage (-2V) to a particular segment, the flow velocity is locally manipulated with an enhancement of flow rate from $0.61\ \mu L/\min$ to $1.29\ \mu L/\min$. Similar enhancement to fluid velocity has been achieved by using 3d stepped electrodes to a directed ACEO flow [33] [58].

Besides the advantages, obstacles also lie on the road of applying ACEO in LOC devices to a further degree. Qualitative discrepancies, sometimes at the orders of magnitudes, are seen between theoretical predictions and experimental measurements. A comprehensive summary is given in [59]. The suppression of flow velocity by electrolyte

concentration due to insufficient double layer charging is another major issue which limits the utility of ACEO in many LOC systems. The ACEO phenomenon has been experimented with immeasurably small velocities for electrolyte concentrations in excess of 10 mM [59]. This confines the attraction of ACEO to applications in which dilute and relatively aqueous solutions are used, for examples, deionized water as a displacement of bio-fluids in microcooling.

2.2 AC Electrothermal Effect in Microfluidics

ACET effect arises from uneven Joule heating due to an electric current flowing through the fluid. The theoretical foundation of ACET mechanism is a coupling problem which involves electric, thermal and fluidic mechanical formulations. At the time an ac signal is applied, the electric field is established within the solution. Charged particles are attracted by the electrode with opposite polarity and migrate, which forms the ionic current. The current density in the fluid is expressed as:

$$J = \sigma E = (\mu_+ + \mu_-)cE \qquad (2\text{-}7)$$

where σ is the fluid conductivity, c is the concentration, μ_+ and μ_- is the limiting ion conductivity for anions and cations which are constants at 298K. Eq (2-7) indicates the resistive manner of fluid bulk. In addition, the electrical Reynolds number is much less than one in microfluidic systems, implying that ohmic current dominates.

The current flows through the ohmic fluid bulk and henceforward generates heat (this process is named the Joule heating). In order to estimate the temperature rise in micro-electrode devices, the energy balance equation given below is used to link the electric and thermal field together [45]:

$$\rho_m c_p \bar{v} \bullet \nabla T + \rho_m c_p \frac{\partial T}{\partial t} = k\nabla^2 T + \sigma E^2 \qquad (2\text{-}8)$$

where ρ_m is the mass density, c_p is the heat capacity, v is the fluid velocity and k is the thermal conductivity. The first term in Eq (2-8) illustrates the effect of heat convection by fluid motion. The effect of fluid motion on the temperature profile is assumed to be minimal [45]. In order for this to be true, we need:

$$\frac{\rho_m c_p v l}{k} << 1 \qquad (2\text{-}9)$$

Typically for water, $k = 0.598 J/m/s/K, c_p = 4.184 * 10^3 J/kg/K$. For a system with characteristic dimension of 60 microns, the effect of fluid flow on the temperature profile can be neglected even for a fluid velocity approaching 1mm/s. The second term in Eq (2-8) stands for the temperature diffusion process. The diffusion time estimates can be deducted from Fourier equation as [45]:

$$t_{diff} = \frac{\rho_m c_p l^2}{k} \qquad (2\text{-}10)$$

The diffusion time is typically at the order of $10^{-3} s$ in micro-systems. In another words, the thermal equilibrium is established within $10^{-3} s$ after applying the signal. Thus, for the fields of frequency greater than 1 kHz, the differential temperature change is neglected. Therefore Eq (2-8) is reduced to:

$$k\nabla^2 T + \sigma E^2 = 0 \qquad (2\text{-}11)$$

The temperature rise is estimated by substituting for the electric field as:

$$\Delta T \approx \frac{\sigma V_{rms}^2}{k} \qquad (2\text{-}12)$$

Since the electric field is highly non-uniform, the power density is also highly

non-uniform. The temperature variation in fluid gives rise to local changes in permittivity and conductivity. These inhomogeneities lead to the net force in fluid. The general expression for the electrical force per unit volume is given as [45]:

$$f_E = \rho_q E - \frac{1}{2} E^2 \nabla \varepsilon + \frac{1}{2} \nabla (\rho_m \frac{\partial \varepsilon}{\partial \rho_m} E^2) \tag{2-13}$$

where ρ_q is the volume charge density. The last term is the electrostriction force that can be ignored in an incompressible fluid (it is the gradient of a scalar) [60]. The first term is the Coulomb force, and the second is the dielectric force. The estimation of these forces can be made from the charge density equation as described in Gauss's law $\rho_q = \nabla \cdot (\varepsilon E)$. By performing a lowest order perturbative expansion and separating electric field into the sum of the applied field E_0 and the perturbation field E_1 ($E_1 << E_0$) [45], equations above can be combined to get:

$$f_E = (\nabla \varepsilon \cdot E_0 + \varepsilon \nabla \cdot E_1) E_0 - \frac{1}{2} E_0^2 \nabla \varepsilon \tag{2-14}$$

The charge conservation equation is $\frac{\partial \rho_q}{\partial t} + \nabla \cdot (\rho_q u) + \nabla \cdot (\sigma E) = 0, and, \nabla \times E = 0$

Implied by a very small Reynolds number, the ratio of magnitude of the convection current $\rho_q u$ to the conduction current σE is negligible. Hence the second term in charge conservation equation is omitted. If we consider the field is time varying ($E_0 = \mathrm{Re}[E_0 e^{j\omega t}]$), we can rearrange the charge conservation equation and get

$$\nabla \cdot E_1 = \frac{-(\nabla \sigma + j\omega \nabla \varepsilon) \cdot E_0}{\sigma + jw\varepsilon} \tag{2-15}$$

The perturbation expansion can be understood as follows. Since field is oscillating with frequency, the steady component of the force produces a continuous motion. For the

isothermal case, the total force is zero since there is no free charge. When non-uniform electric fields is present, the heating process produces gradients in local conductivity and permittivity by $\nabla\varepsilon = (\frac{\partial\varepsilon}{\partial T})\nabla T$ and $\nabla\sigma = (\frac{\partial\sigma}{\partial T})\nabla T$, leading to the migration of free space charges under electric field and exerting force on fluid through viscosity. Thus, by substituting Eq (2-15) into Eq (2-14), we have the final form of the time average electric thermal force:

$$< F_{et} > = -0.5\left[(\frac{\nabla\sigma}{\sigma} - \frac{\nabla\varepsilon}{\varepsilon}) E \frac{\varepsilon E}{1+(\omega\tau)^2} + 0.5\left|E\right|^2 \nabla\varepsilon \right] \qquad (2\text{-}16)$$

where $\tau = \varepsilon/\sigma$ is charge relaxation time. The formula shows that the thermal force F_{et} follows the directions of electric field and is proportional to the temperature gradient. In aqueous solutions at 293K, we have [61]

$$\frac{1}{\varepsilon}\frac{\partial\varepsilon}{\partial T} = -0.004 \Rightarrow \frac{\nabla\varepsilon}{\varepsilon} = \frac{1}{\varepsilon}\frac{\partial\varepsilon}{\partial T}\nabla T = -0.004\nabla T/^{o}C \qquad (2\text{-}17)$$

and $$\frac{1}{\sigma}\frac{\partial\sigma}{\partial T} = 0.02 \Rightarrow \frac{\nabla\sigma}{\sigma} = \frac{1}{\sigma}\frac{\partial\sigma}{\partial T}\nabla T = 0.02\nabla T/^{o}C \qquad (2\text{-}18)$$

Eq (2-17) and Eq (2-18) show that two terms in ACET force have different signs. Letting two terms equal, we can have the crossover frequency $f_c = \frac{\sqrt{11}\sigma}{2\pi\varepsilon}$, which is only dependent on the fluid properties and typically at the range of kHz to Mhz. [62] showed that the ET force has its maximum effects in a frequency range below the crossover frequency where the Coulomb force dominates.

2.3 Fluid characteristics of ACEO and ACET

ACEO and ACET mechanisms are both applied to various electrode designs to induce electrokinetic flows for micro-sample processing and fluid manipulation in LOC devices. ACEO originates from electric stress at the electrode surface while ACET exerts volume force on fluid bulk. This brings discrepancies in many aspects.

1. Characteristics of driving force

ACEO is a surface force, and fluid flows driven by ACEO have the maximum speed at the charged surface. On the contrary, ACET force directly applied to the bulk. Hence, slip boundary conditions applies to ACEO models with a surface velocity and ACET models pick up non-slip condition for the electrode surface. Additionally, the magnitude of ACET velocity does not merely depend on the field strength, but also the temperature gradient, which could reach its maximum at some distance from the electrodes. Therefore ACEO peak velocity is seen on the surface, while ACET flow maximum is within the bulk.

The above property of velocity profile has an impact on the performance of electrokinetic devices at very small scale. When the hydraulic diameter or system dimension is reduced to the scale of a micrometer, ACEO velocity is expected to increase. On the other hand, due to no-slip boundary condition of ACET flow, the flow velocity will become suppressed when the hydraulic diameter becomes less than 20 microns.

2. **Frequency Dependency**

The bell-shaped frequency dependency of ACEO has been discussed in section 2.1. Two elements, tangential electric field and the zeta potential, determine the magnitude of

ACEO induced fluid flow. At high frequencies (typically higher than tens of kHz depending on ionic strength), there is not sufficient time for ion migration and hence electric double layer cannot be fully formed. At low frequencies, ions will completely screen the surface charges of the electrodes, resulting in low tangential field strength. This fact leaves a window from few hundred Hz to few kHz which is ideal for the ACEO mechanism. Data in [63] shows that ACEO is most noticeable for frequencies lower than 100 kHz, beyond which its effect is minimal and can be neglected. The optimal frequency for ACEO operation can be estimated as $\Omega \approx {}^{1}\!/\!_{2\pi} \cdot {}^{\sigma}\!/\!_{\varepsilon} \cdot {}^{\lambda_D}\!/\!_{l}$, where λ_D is the Debye length, and *l* is the characteristic length of the system, e.g. the electrode spacing.

Recall that the expression of electrothermal force $\vec{F}_{et} = -0.5\left[\underbrace{(\frac{\nabla\sigma}{\sigma} - \frac{\nabla\varepsilon}{\varepsilon})\vec{E}\frac{\varepsilon\vec{E}}{1+(\omega\tau)^2}}_{CoulombForce} + \underbrace{0.5\left|\vec{E}\right|^2\nabla\varepsilon}_{DielectricForce}\right]$. ACET velocity has little dependency on frequency when it is well below the cross-over frequency. Coulomb force will dominate at low frequency. For aqueous solutions at 293K, conductivity and permittivity change with temperature gradient as $\frac{1}{\sigma}\frac{\partial\sigma}{\partial T} = 0.02$ and $\frac{1}{\varepsilon}\frac{\partial\varepsilon}{\partial T} = -0.004$. The two forces in the Eq (2-16) compete in magnitude and tend to cancel each other. The cross-over frequency of ACET force is derived by letting two forces equal. Fig 2-4 shows the transition frequency of 170 MHz for a solution with conductivity of 0.224 S/m. Such result indicates that ACET fluid flow is the result of Coulomb force under usual experimental conditions.

3. Conductivity Dependency

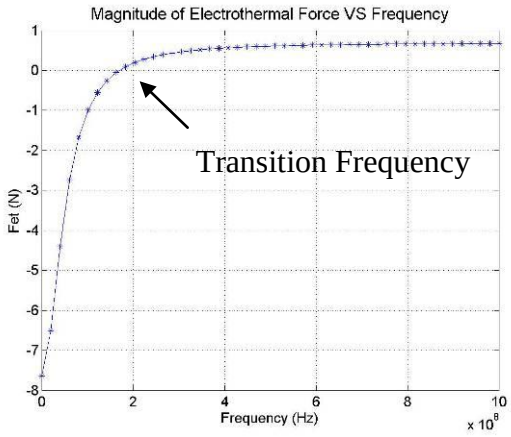

Figure 2-4 Plot of electrothermal force versus frequency.

From the definition of Debye length, we can see that ACEO is limited to fluids with low conductivities. When the fluid ionic strength increases, the Debye length of the double layer is reduced, leading to the lower zeta potential. Peak ACEO velocity (at its optimal frequency) decreases. Also the double layer relaxation time becomes shorter. The frequency at which ACEO velocity maximizes goes higher. ACEO flows become weak for fluid with conductivity above 0.1 S/m [33]. As a contrast, the temperature gradients increase linearly with conductivity and so enhance the ACET flow. Fluids with conductivity up to 1.58 S/m (Phosphate buffered saline) were tested in our experiments in chapter 3. ACET effect also functions on fluid with low conductivities. We have observed flow motion of tap water ($\sigma = 2*10^{-2} S/m$) and deionized water ($\sigma = 2*10^{-4} S/m$) at medium frequencies ranges (tens of kHz to hundreds of kHz) with noticeable velocity in the reversed direction. Chapter 5 describes one case of such a flow reversal in symmetric electrode system.

2.4 Dielectrophoresis (DEP) force

Dielectrophoresis (DEP) force is different from two mechanisms above as it direct applies to particle itself. It originates from the difference of dielectric properties between neutral particles and the fluid. When the polarization of particle is greater than that of the medium, the net negative charge faces the positive electrode and the net positive charge faces the negative electrode; the polarization vector is anti-parallel to the field vector. The reverse occurs when the medium contributes more charge. If we look particle as a whole, a dipole is formed by polarization. Therefore, when a particle is placed in a non-uniform electric field, the Coulomb force that both ends of dipole receive is unbalanced. A net force then drives the particle away or toward the high field locations, depending on the particle's relative polarizability to that of the fluid. Fig 2-5 lists the two situations of particle polarization in a non-uniformed electric field. When the particle dielectric properties (i.e. complex permittivity which is defined as $\varepsilon_p^* = \varepsilon_p - j\frac{\sigma_p}{\omega}$, the subscript p means particle) is greater than surrounding fluid, the particle polarization causes the electric field line to bend towards the particle (Fig 2-5a).

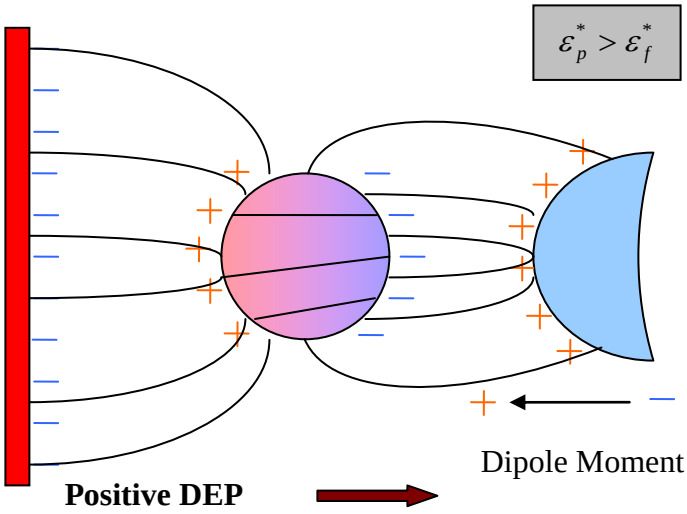

(a)

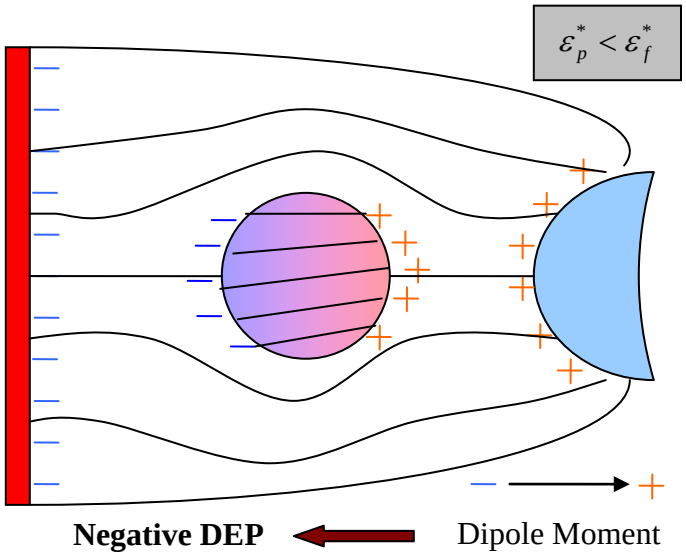

(b)

Figure 2-5 Particle polarization within non-uniform electric field. (a) pDEP, (b) nDEP

The particle acts like a “conductor”. The net force causes the particle movement towards field maxima. The phenomenon is named as positive DEP (pDEP). The opposite is shown on Fig 2-5b, where the particle polarizability is less than that of the electrolyte. The particle acts like an “insulator”. Negative DEP happens and drives particle away from field maxima.

In ac field, the induced dipole changes direction with applied field. However, a relaxation time is required for the charges to reach equilibrium. At low frequencies, the movement of charges keeps pace with switching direction of electric field. For higher frequencies, induced charges do not have sufficient time to response. The particle polarization is then transited into the alternative situation in Fig 2-5b. Therefore, at different frequency spectrums, the particle experiences forces on different directions. This fact leads to frequency dependency of DEP forces. For particles with radius r

suspending in solution with permittivity of ε_f, the representation of DEP force magnitude is given by [64]:

$$\vec{F} = 2\pi\varepsilon_f r^3[\mathrm{Re}(f_{CM})\nabla E_{RMS}^2 + \mathrm{Im}(f_{CM})(E_{x0}^2\nabla\varphi_x + E_{y0}^2\nabla\varphi_y + E_{z0}^2\nabla\varphi_z)] \quad (2\text{-}19)$$

f_{CM} is the Clausius-Mossotti factor which reflects the magnitude and direction of field-induced dipole and given by $f_{CM} = (\frac{\varepsilon_p^* - \varepsilon_f^*}{\varepsilon_p^* + 2\varepsilon_f^*})$. The subscript *p* and *f* stands for particle and fluid, respectively. The superscript indicates the complex permittivity. $E_{x0}^2\nabla\varphi_x$, $E_{y0}^2\nabla\varphi_y$, $E_{z0}^2\nabla\varphi_z$ are the directional component of magnitude and phase of electric field in Cartesian coordinate which only applied to traveling wave signal. Fig 2-6 shows a sample plot of f_{CM} with respect to the frequency.

2.5 Equivalence Circuit Model in Microfluidic Chamber

Impedance analysis using equivalence circuit model can be used to assess the relative importance of double layer charging (ACEO) at the electrode surfaces and Joule heating (ACET) in the fluid bulk. At the interface of electrolyte and electrodes, there are double

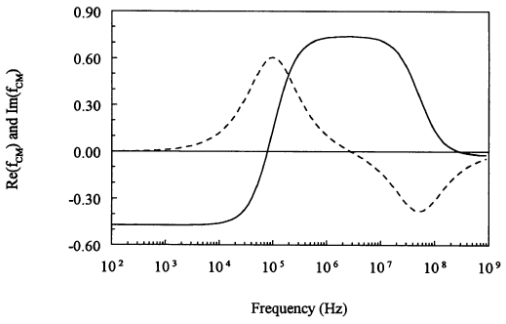

Figure 2-6 Plot of f_{CM} with frequency in [64]

layer capacitances, C_{dl}, due to charging at the interface, (it is not an ideal capacitor, but act like a constant phase element (CPE) as defined in [65] [66].) The fluid bulk is treated as a resistor R_{solu} and electricity passing it generates heat according to Ohm's law. It is in series with the interfacial impedances on both ends. C_{cell} represents direct dielectric coupling between electrodes and its value is determined by dielectric properties of the fluid. R_{lead} accounts for the parasitic resistance of the microelectrodes. The electrode may serve as a voltage divider for use in a conductive fluid. The circuit is shown in Figure 2-7.

At small DC voltages with no chemical reactions, the electric field in fluid is blocked by the capacitor-like behavior of double layer, resulting in no electrokinetic flow. Hence for DCEK, electrode reactions are necessary to establish an electric field in fluid. With low frequency ac signal, the impedance from C_{dl} is much larger than that from R_{solu}. The system exhibits mostly capacitive characteristics and more voltage drops across the interfacial double layer, which is desired for ACEO techniques. When frequency increases, the double layer impedance loses its dominance as there has no enough time for free ions to travel between electrodes and deposit under the attraction of electrostatic force. Instead, fluid volume force from ACET effect dominates. When the frequency

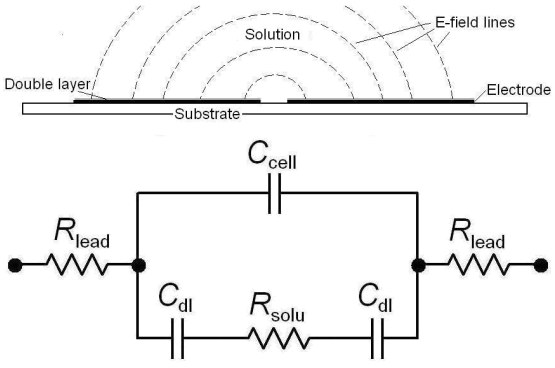

Figure 2-7 RC equivalent circuits of an electrode/fluid system

increases further (usually at MHz range), the dielectric coupling between the two electrodes comes into play. The whole system exhibits capacitive characteristics again. The frequency dependency of electrode/electrolyte system will be carefully examined in our ACET experiments and used to determine the cause of flow reversal observed in symmetric experiments.

Chapter 3. AC Electrothermal Effect for Microfluidic Applications

The motivation of research in ACET study has been previously mentioned. Reduction of fluid manipulation ability with respect to increased fluid conductivity of ACEO demands an alternative approach to handle fluids with higher ionic strength. This chapter describes two sets of experiments as proof of principle that the ACET effect is practical for biofluidic functions: face-to-face particle trapping and planar micropumping. Two types of electrode designs are used to test the ACET's versatility. In face-to-face electrode system, ACET effect induces vortices in fluid and brings embedded particles (in sub-micron size) which are originally evenly distributed in fluid to electrode surface. Particles are then trapped at the surface by forces such as electrostatic attraction, Van del Waals force or DEP force. The particle count in a sample area was tripled within 2 minutes as measured in our experiments. The net pumping motion by ACET effect was observed using asymmetric interdigitated planar electrodes. The working fluid was seeded with latex micro-particles to track fluid motion. At the beginning of experiments, the micro-particles were located at one end of the chamber. After applying electric field, they quickly moved forward and occupied the whole channel, showing a successful pumping attempt by ACET effect. Both applications prove the abilities of ACET effect in fluid handling and offer its use for further study in LOC designs. This chapter starts with the research methods used in our electrothermal experiments, including particle image velocimetry (PIV), micro-device fabrication and simulation. Results from numerical simulation using Femlab/Comsol Multi-Physics is presented and compared with experiment measurements.

3.1 Research Methods

3.1.1 Particle Image Velocimetry (PIV)

Particle image velocimetry is an optical method used for fluid visualization. Tracer particles seeded in the fluid are assumed to follow the flow motion and are used to extract the velocity information of the flow. The common practice is to record consecutive picture frames by a CCD camera, divide the images into small interrogation spots and cross correlate the images from two time exposures. The spatial displacement that produces the maximum cross-correlation index approximates the average displacements and is used to calculate the velocities. This method is used in our research to extract the fluid velocity. In our lab, a CCD camera (Nikon Coolsnap ES) is attached to the Nikon eclipse LV100 microscope and outputs real-time images to a PC. The images are processed using Image Pro 3DS (www.mediacy.com. Cybernetics Inc) software. The Image pro software has a built-in image processing capability to calculate the displacement of each individual selected particle. A number of particles were chosen in our research to ensure the sample size. Fluid velocity is the average values of these sample measurements. Time interval between two consecutive frames taken by camera is fixed at 0.1s.

3.1.2 Numerical Simulation

Finite element analysis using *Femlab/Comsol Multiphysics* (www.comsol.com; Stockholm, Sweden) is used throughout our research to predict the fluid behavior under various conditions. The models are reduced into two-dimension by simulating the cross sectional view of the microfluidic device. The models restore the experimental conditions

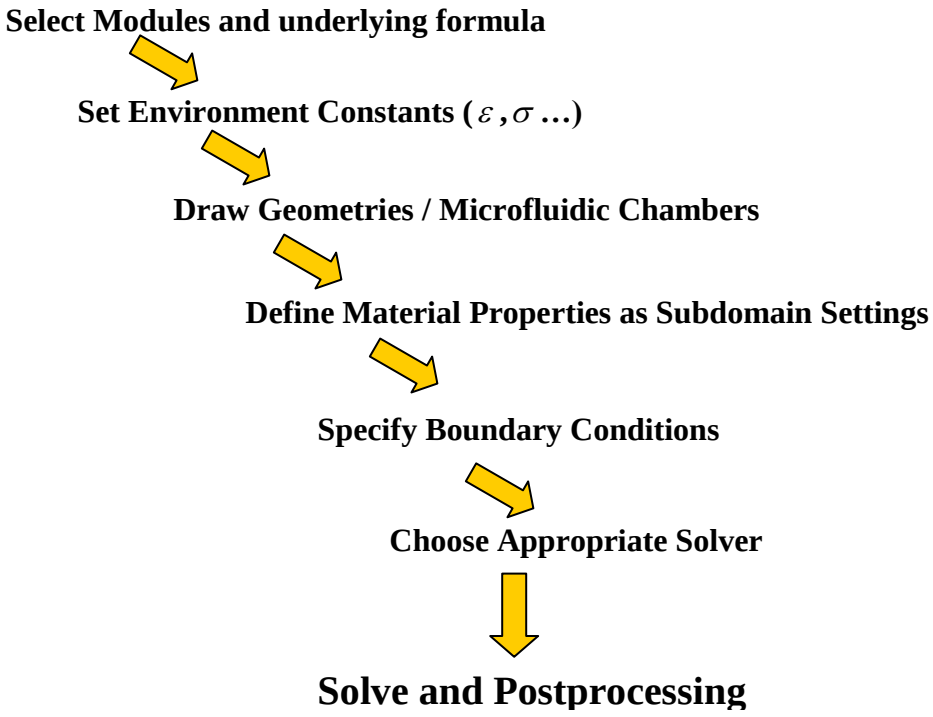

Figure 3-1Flow chart of numerical simulation

and the simulated results show good agreement with the experiment measurements. The following flowchart (Fig 3-1) describes the steps of microfluidic simulation.

The module selection in Comsol Multiphysics simulation is critical, as the module provides a set of differential equations that govern the solution space and also include a few types of appropriate boundary conditions to select. AC electrokinetics simulation involve solving for electric field in the media, i.e. conductive media (shorted as "DC") module and fluid mechanics, i.e. incompressible Navier-Stokes ("NS") module. AC electrothermal simulation requires additional heat convection and conduction (CC) module to be coupled between the above two modules so that the solutions of electric

field are used to calculate Joule heating and temperature distribution in the fluid. The ACET force is then calculated from electric and thermal field distribution. Since the heat convection due to fluid flow is shown to be negligible in chapter 2, three modules are solved in a sequential order with coupled variables. Environmental constants such as fluid conductivity and relation permittivity are predefined.

The geometries of simulated models share the same dimensions with experiment setup. For simplicity, we simulate only one period of electrode pair. The effects of repeated electrode patterns are accounted for by applying periodic boundary conditions to the side boundaries (often seen as the fluid inlet and outlet). The sub-domain equations are defined in the model selection step. The boundary conditions are specified with regard to the physical meaning of each boundary. The color scale in result presentation shows the magnitude of physical terms and arrows indicates the direction.

3.1.3 Fabrication

The electrode arrays used for ACET experiments were fabricated on bare silicon wafers using standard photolithographic methods. A glass mask was first designed using CAD software (done by Prichya Mruetusatorn) with transparent and opaque patterns as negative images of the electrodes. The wafer fabrication was then performed in a cleanroom in Oak Ridge National Lab. The figure below (Fig 3-2) illustrates the fabrication process.

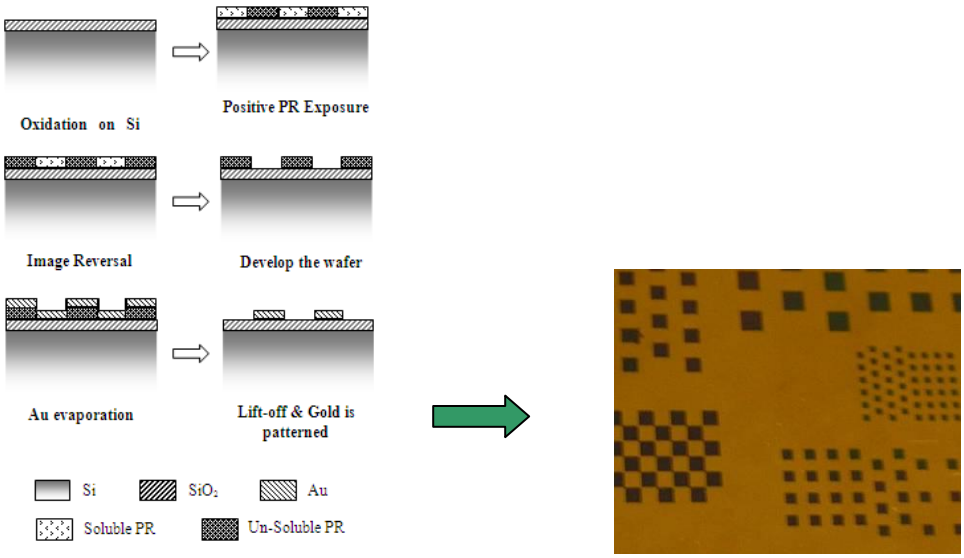

Figure 3-2 Fabrication steps of silicon wafer

The procedures for wafer fabrication are:

- RCA wafer cleaning using corrosive chemicals. The first step is to remove organic contaminants at high temperature (70-100^{o}C). After that wafers are dip etched in hydrofluoric acid (HF) to remove a thin layer of oxide that might have grown on silicon. Ionic and metal contaminates are then removed in acid solutions at an elevated temperature.
- Oxidation using thermal furnace. This step deposits a layer of silicon oxide which is used as insulation in our experiments on bare silicon. The oxide thickness is 270nm on average with 10% of variation after thermal oxidation.
- Lithography process
    1. Spin a layer of Hexamethyldisilazane (HDMS, a hydrophobic substance) to increase adhesion between wafer and photoresist. The primer is dropped at the center of wafer which sits on top of a spinning device.

We wait ten seconds for it to react with wafer and then spin at 3000 RPM for one minute so that HDMS is evenly distributed on wafer surface.

2. Apply a thin layer of S1818 positive photoresist (1.86 micron) using the same spinning parameters (3000 RPM for one minute).
3. Soft bake the wafer at 115^{o}C for one minute to increase the adhesion.
4. Use contact aligner to transfer electrode patterns onto the wafer surface from mask. The ultraviolet light hardens the photoresist that is not protected under the shade of patterned mask.
5. Image reversal using Ammonia (NH3) for one to one and a half hour. This step reverses the effect of ultraviolet light illumination by weakening the areas that are exposed to UV light and makes them solvable for later developing.
6. Wafer with patterned photoresist layer is developed in a CD-26 TMAH solution for one minute. Only weakened areas are dissolved in developer. A flood exposure step of one minute using plain mask is performed before development to ensure the pattern quality.
7. Descum the wafer surface to remove residues and ensure the uniformity of photoresist layer. The descum chamber is pre-vacuum to 5 mTor. Gas valve then increase the pressure to 150 mTor. The descum process takes 30 seconds at a 10V, 400W voltage.

- E-beam evaporation of electrodes

1 A thin layer of Ti (5 nm) are deposited using electron beam evaporation.

This step increases the bond between gold electrode layer and the photoresist. The current is controlled at 0.1~0.15 A to maintain a deposition speed of 1A^{o}/s. The evaporation chamber is pre-vacuumed to a pressure of $5*10^{-6}$ Tor

2 Deposit 95nm of Au at 0.3 A current and $2*10^{-7}$ Tor pressure

- Lift off. This step removes the remaining photoresist layer together with metals on top. The metal that is directly deposited on silicon oxide is kept as electrode.

1 Soak the wafer in acetone solution for 1~2 hours. After that, use a ultrasonic device for 30 seconds twice to further break down the adhesion between photoresist and wafer

2 Clean wafer surface with deionized water and spin dry for final processing

3.1.4 Experiment Setup

Fig 3-3 shows a typical system setup for microfluidic experiments. Electric signals were generated by an Agilent 33220A function generator (Agilent Technology, CO) and then amplified (Model #: 354-1-50, Heico Company) to reach a desired voltage level for electrothermal experiments. Voltages of 1.4-11.3Vrms at 200 kHz were used. The experiment process was monitored through the Nikon eclipse LV100 microscope and recorded using the attached CCD camera. The z-direction manipulation was provided by the microscope so that the distance between focal plane and electrode surface is monitored.

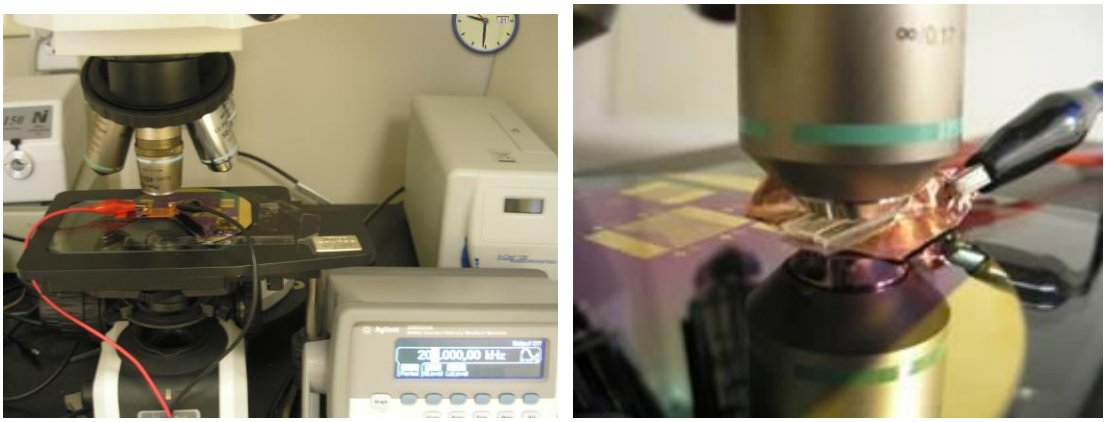

Figure 3-3 Experiment apparatus and fluidic chamber

Diluted sodium chloride solution is used for the trapping and pumping experiments described in this chapter. High conductivity of 0.224 S/m provides a similar fluid medium as used in many bio-applications. Fluorescent particles with 500nm diameter (Molecular Probes) were suspended in the working fluid as tracers so that fluid motion can be visualized from microscope.

3.2 Microfluidic Applications

3.2.1 ACET Particle Trapping on Parallel Plate Configuration

In our particle trap device, two electrodes are placed facing each other. The fabricated wafer serves as the bottom electrode and a piece of conductive indium-tin oxide (ITO) glass is placed on top as top electrode which also seals the chamber. Two electrodes are separated by a spacer of 500 μm ((PC8R-0.5, Grace Bio-Labs, Inc.). The total volume of fluid chamber is $1.27\,ml$. Fig 3-4 shows schematics in which two regions of gold electrode are illustrated.

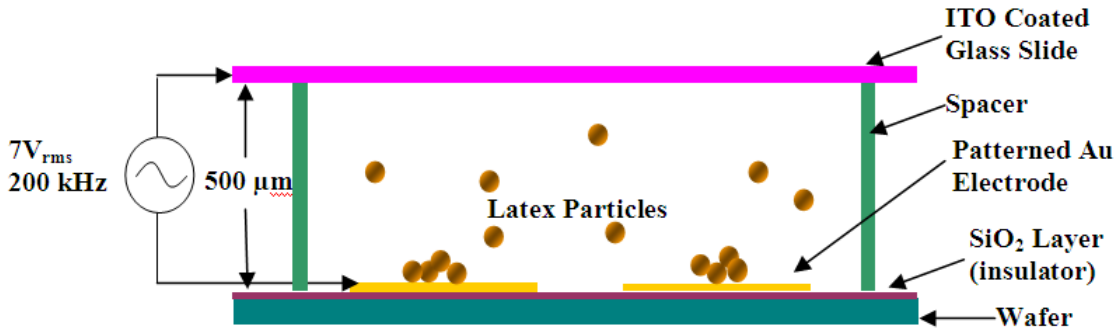

Figure 3-4 Schematic drawing of parallel ACET trap

Simulation

The geometry in Figure 3-4 is used in face-to-face trap simulation in Comsol Multiphysics with one part of bottom electrode included, as shown in Figure 3-5. The bottom electrode is 600 microns wide as measured in the experiment. The top boundary is covered by the entire piece of ITO glass and therefore treated as an electrode of 1,800 microns wide. An intermediate voltage level (7.17Vrms, 200 kHz) is applied between two electrodes.

Since there is no externally applied charge density in fluid, the Poisson equation as described in Eq (2-1) is simplified into the Laplacian equation $\nabla^2(\sigma V) = 0$ for calculation of electric field distribution. Non-electrode boundaries are treated as electric insulation. For the thermal module, the subdomain equation is given in Eq (2-11). Joule heating is the only heat source in our simulations. Treating the electrodes as isothermal (300K at room temperature) is appropriate for conductive solutions [33]. The rest of boundaries are considered as thermal insulation, meaning that no heat exchange through the outer environment. The heat capacity and thermal conductivity of the solution is 4184 J^oC^{-1} and 0.598 $Jm^{-1}s^{-1}K^{-1}$, respectively. In fluid dynamics module, the top and bottom boundaries are solid, and therefore given non-slip conditions. Fluid can enter and leave the chamber

freely from side boundaries. They are treated as neutral boundaries as if there is "no boundaries at all". The water viscosity is 0.001 $kgm^{-1}s^{-1}$ at 20°C. The ACET force is calculated by equation (2-16) and inputted in subdomain settings.

The calculated electric field shows an uneven distribution (Fig 3-6). The field maxima are located at the edge of bottom electrode with peak values of 0.522V/micron and decreases rapidly with increasing distance as expected.

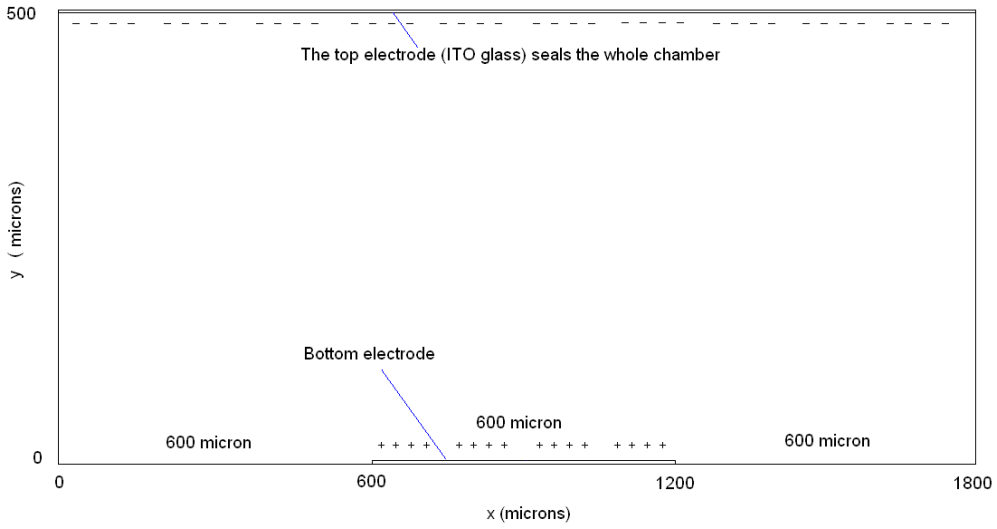

Figure 3-5 Simulation geometry of parallel particle trapping

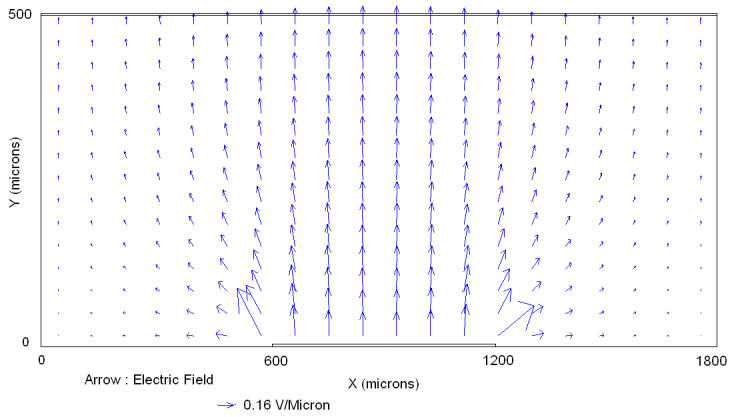

Figure 3-6 Electric field distribution of parallel trap device

The solution to the thermal equation gives the temperature distribution as shown in Fig 3-7. For an applied voltage of 7.17Vrms, the temperature gradient reaches a peak value of 0.609 K/μm at the same locations where electric field is maximized. The temperature gradient is represented by arrows in Fig 3-7. The arrow length scales with the gradient magnitude. Peak temperature rise is simulated to be 2.44 K. The high temperature region forms a ring shaped distribution due to the asymmetric electrode lengths.

The fluid motion is plotted in Fig 3-8 with streamlines and arrows both indicating the velocity scale. Two counter-rotating vortices are produced above the bottom electrodes. The flow direction is upwards in the middle and downwards at the sides. Global velocity maxima are seen at the location about 20 microns away from the bottom electrode, where the temperature gradient is at the highest. Flow velocity decreases along the electrode inwards until it becomes zero at the middle. Transversal motions are cancelled out by flows in opposite directions and particles are stagnated at the center.

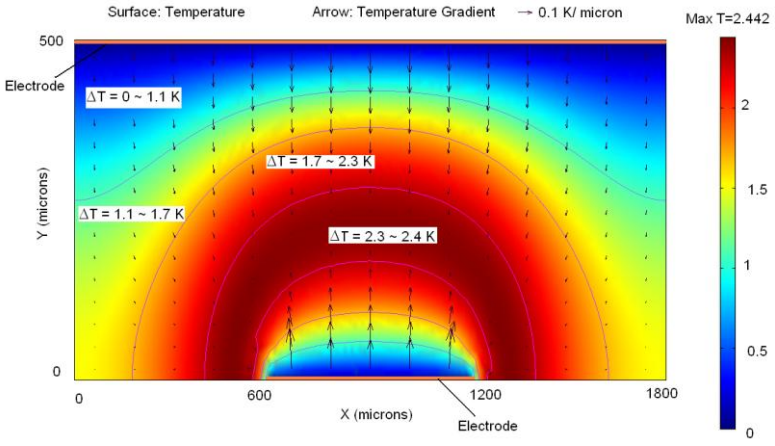

Figure 3-7 Temperature distribution simulation. The maximum temperature rise is about 2.4 K at 7.17Vrms. The temperature gradient (in arrows) has its maxima close to the electrodes.

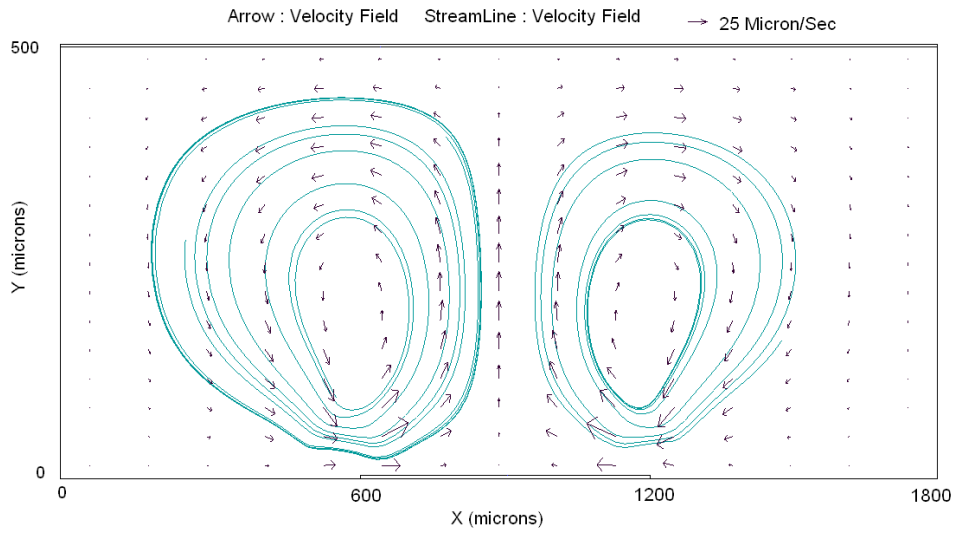

Figure 3-8 Simulated flow field profile. Above the bottom electrode, two counter-rotating vortices are formed that move from the electrode edges inwards.

Experiment

The experimental setup of ACET parallel particle trap was given at the beginning of this section. Embedded particles are fluorescent and the intensity change signifies the change in particle counts. When an AC signal was applied, particles started to move in circulating swirls. At the wafer surface, the particles flow from both electrodes edges to the center. When the focal plane of the microscope was elevated to be 80 microns above the wafer, the flow directions were reversed and particles were seen entering the plane from center and leaving from sides. Thus by following the 3d particle trajectories, we confirmed that fluid flow was in vortex pattern vertical to the surface, same as seen in simulation models. Temperature rise of 2.1K within fluid was recorded using an infrared thermometer (model # 52224, Mastercool, Inc.) when 7.17 Vrms was applied. Particle movements at this high frequency region are hardly observed. That is probably because of the attenuation of Coulomb force and enhance of dielectric force. The magnitude of

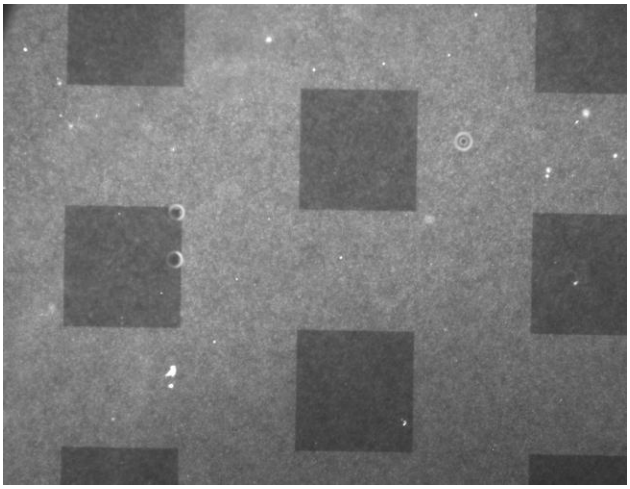

(a) Before applying AC voltage

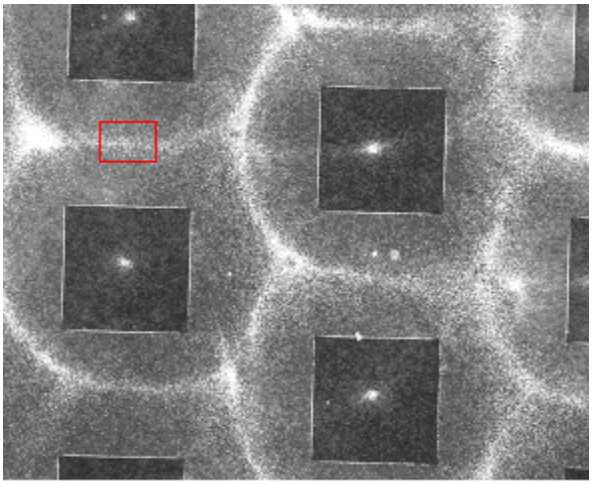

(b) 5 minutes after applying AC voltage

Figure 3-9 Wafer surface before and after AC signals being applied. Particles were directed towards null points of electric fields (center) and became trapped. (Bright areas indicate high density of particles.)

ACET force is reduced by the counteracting of forces.

Fig 3-9 (a) and (b) compare the appearance of wafer surface before and 5 minutes after a voltage was applied. Particles were evenly distributed over the whole bottom surface. The dark squares were the non-conductive regions. The process of particle

aggregation is illustrated by the increased illumination at center of bottom electrodes in Fig 3-9 (b). The collection process was mostly completed after a few minutes when large proportion of particles becomes immobilized. Same as shown in simulation, particles were trapped to the center of electrodes and therefore forming the cell-like shapes. Particles also formed smaller clusters at the centers of non-conductive regions. This was attributed to the symmetry of electrode design where influences of electric fields at those locations were cancelled out. Flow from the vicinity propelled particles and had them deposited at center.

The trapping effects are quantified in our experiments. Fig 3-10 shows the number of particles that were trapped into a designated rectangle area of 360 x 225 μm^2, of which the location is indicated by the red rectangle in Fig 3-9 (b). The particle concentration was measured as 6×10^5 counts per mm^3. At the beginning of experiment, an initial count of 30 particles in area was measured. After two minutes, the number of particles was tripled, showing the effectiveness of active ACET particle trapping. The number of trapped particles versus time shows a linear relationship with a positive slope of trapping rate at about 0.5 particles per second.

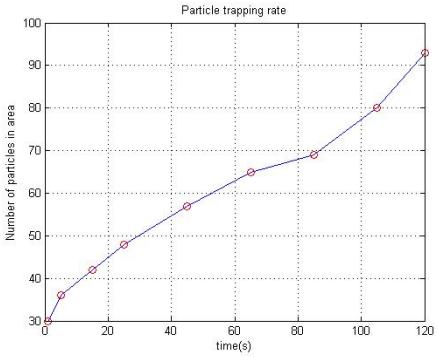

Figure 3-10 Number of particles collected in designated area as a function of time

3.2.2 Asymmetric Micropump

The above trapping experiments demonstrate the capability of ACET effect in producing fluid flow so that embedded particles are trapped with proper electrode design. Since the maximum velocity of ACET flow is on the order of 100 microns/s, using a different electrode design we can utilize ACET effect for micropumping.

Electrode array with multiple groups of asymmetric electrode pairs in our micropumping experiment are deposited on the silicon wafer (planar placed). The electrodes have dimensions of 100 μm narrow electrode/20 μm between electrode gap/180 μm wide electrode/100 μm between-pair gap. The height of the chamber is 500 μm. The same processes were used to simulate the pumping model, only one electrode pair was included in geometry. The effects of electrode repetition were incorporated by applying periodic boundary conditions to the side boundaries which served as fluid inlet and outlet. The pumping action is self-induced upon applying voltage. Fig 3-11 shows the fluid field profile. The fluid motions are generated by applied electric signals, and the net flow is directed from the narrower electrode towards the wider one.

The micropumping experiments were conducted in the same way of particle trapping experiment. To better visualize the microflow, 1 μm latex particles were injected into one end of a pre-filled channel. The particles were carried along by the fluid and transported from one end of the channel to the other. Image sequence in Fig 3-12 illustrates the pumping action on a particle cluster advancing through electrode pairs when an AC signal of 6.6Vrms at 200 kHz was applied. The focal plane of microscope was ~50 μm above the wafer surface. The height of the focal plane was controlled through a

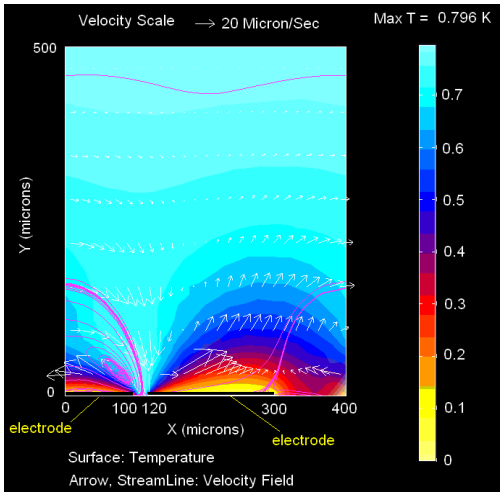

Figure 3-11 Simulated micropumping over a pair of asymmetric electrodes by AC electrothermal effect. Net fluid transport is generated by asymmetric electrodes. Maximum velocity is 162 μm/s at 5.5Vrms.

computerized stepper motor (Optic scan II, CS152Z, Prior Scientific Instrument LTD). Dark slices in Fig 3-12 were the gold electrodes. Colors were inverted in postprocessing for better visualization. Initially, a cluster of particles was seen at the left end of gap between two electrode pairs. It advanced to the next electrode pair upon viscous drag of ACET flow. In Fig 3-12 (c) and (d), the cluster was attracted to the electrode surface as shown in simulation. It left the focal plane and therefore stayed out of focus. In next image (e), it resurfaced to the starting height and prepared to be pumped to next electrode. The average fluid velocity was approximately 117 m/S.

The experimental results shown in this chapter illustrate the capabilities of ACET effect as a candidate for conductive fluid manipulation. The numerical simulation using ACET equations presents assimilar fluid patterns as observed in experiments. The quantitative analysis will be shown in next chapter with more discussion of ACEK mechanisms in depth.

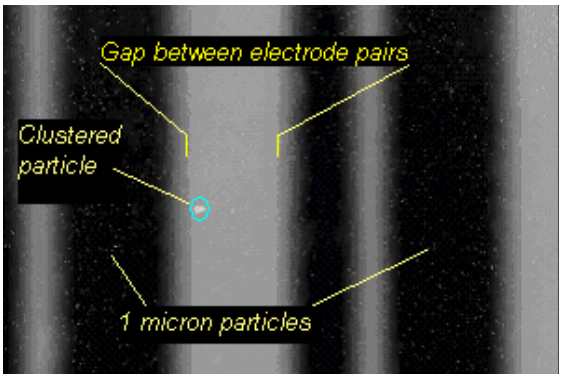

(a)

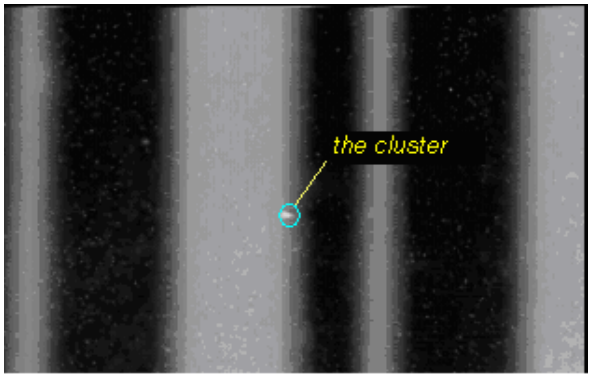

(b)

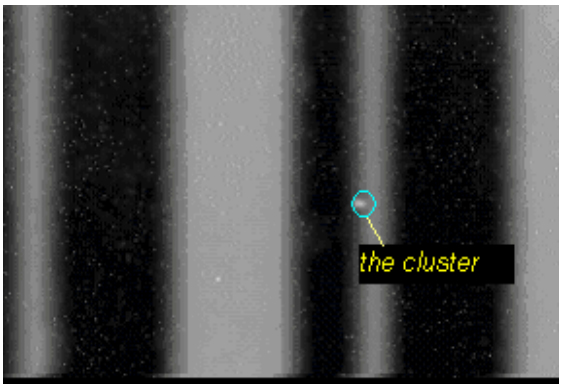

(c)

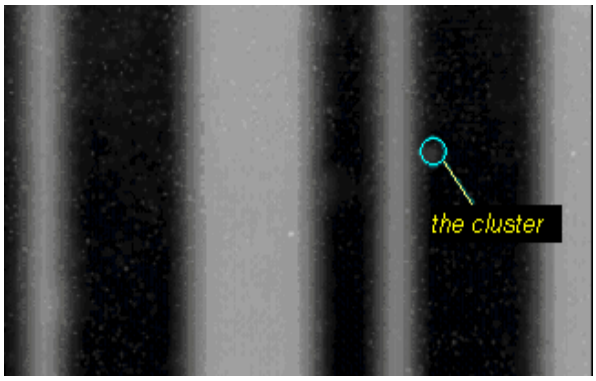

(d)

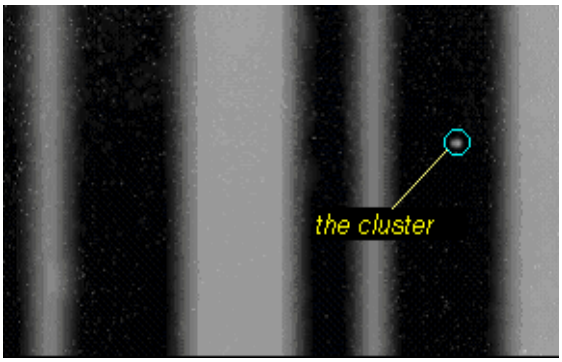

(e)

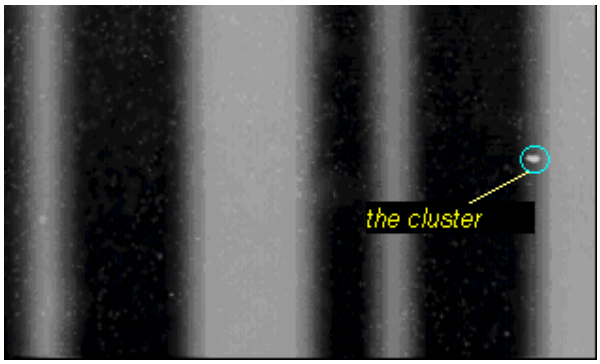

(f)

Figure 3-12 Image sequences showing a particle cluster advancing through the electrodes. The image color was reversed to illustrate the particle more clearly. (a) t=0s, (b) t=1s, (c) t=1.8s, (d) t=2.3s, (e) t=2.9s, (f) t=3.4s. V=6.6Vrms @ 200 kHz.

Chapter 4. Comparisons of AC Electrothermal Effect with AC Electroosmosis

In the previous chapter, the experimental results have demonstrated the capabilities of AC electrothermal effect for fluid manipulation. From chapter 2, we know that ACEO can induce similar flows. Therefore, it is necessary to identify the individual contribution of such forces to observed flow. In this chapter, the experimental data will be analyzed from several angles to ensure that it was ACET effect at play.

4.1 Impedance Analysis

The impedance data was acquired in order to determine the circuit behavior of fluid systems at the frequency range of interest. The equivalence circuit model has been given in chapter 2. Since electrokinetic mechanisms all exhibit frequency dependencies, analyzing the impedance spectrum can help us understand the reason of fluid motion so that the magnitude of each mechanism can be accessed. Data were acquired from 100 Hz to 20 MHz in a logarithm scale. Fig 4-1 shows the magnitude and phase plots of the parallel plate particle trap and the asymmetric micropump impedance. For the trapping device, the magnitude of impedance decreases from $1{,}472\Omega$ at 100Hz to 79Ω at 50 kHz and remains constant until several MHz (Fig 4-1a), while the phase angle changes from -74.831 to -2.149 at corresponding frequencies (Fig 4-1b). The component values were calculated using a Matlab algorithm as: $C_{dbl} \approx 3.788\mu F, C_d \approx 133.45 pF, R_f \approx 41.6\Omega$. The double layer capacitance is

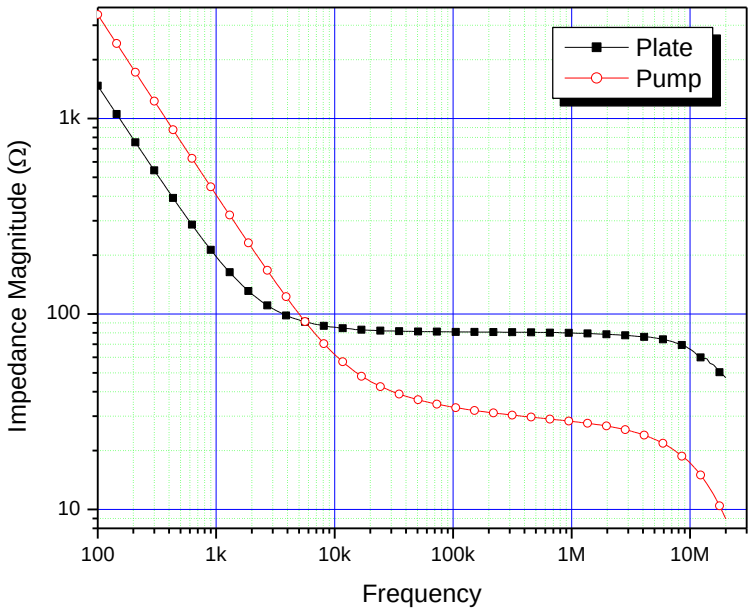

(a)

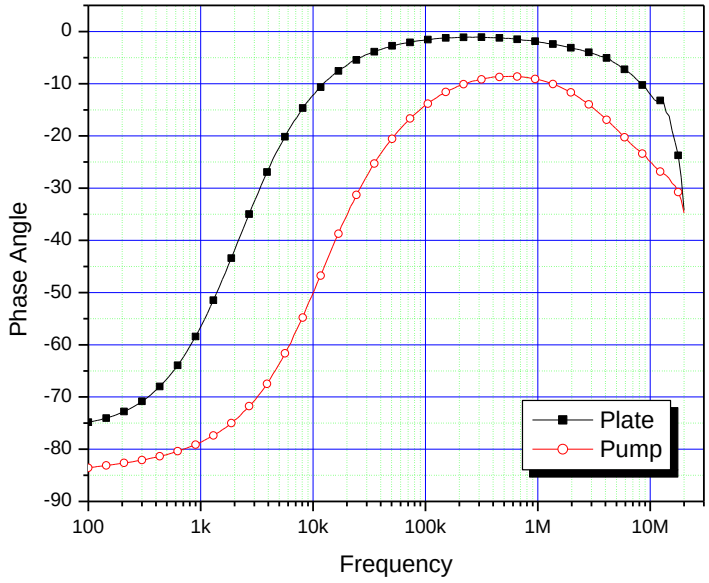

(b)

Figure 4-1 Impedance spectra of the ACET devices from 100Hz to 20 MHz.Magnitude (b) Phase

comparable to the estimated capacitance in previous section where $C_{dbl} \approx 0.3 * AreaOfElectrode = 2.604 \mu F$. The difference could be accounted by impurities at the electrode surface and the non-linearity in double layer models. The impedance measurement shows that the frequency range from 50 kHz to a few MHz is suitable for ACET operation since system demonstrates mostly resistive impedance. The magnitude stays constant over a wide range of frequencies. The phase angle at low frequency does not go to -90^o degrees. It is due to the non-ideality of the double layer capacitance (CPE). When frequencies are high enough (at MHz range), the impedance from paralleled dielectric coupling capacitance starts to dominate, and the system impedance starts to exhibit capacitive characteristics.

The same impedance analysis was performed on the micropump. A very similar pattern is seen with slightly smaller fluid resistance values. The impedance plot gives $26\Omega \angle -12^\circ$ at 200 kHz. Therefore, at the operating frequency of 200 kHz, the system is electrically functioning as a resistor which is suitable for ACET effect.

4.2 Discussions

Many mechanisms mentioned previously have the tendency to become possible sources for observed electrokinetic flow. Impedance analysis above provides insights of system behavior at the operating conditions. A more detailed discussion is given below in order to validate the supposition that ACET is responsible for the observed fluid motion. We use results from face-to-face trapping experiments as examples.

4.2.1 ACET effect

The simulation results of a face-to-face trapping model are shown in chapter 3. A

temperature increase of 2.44 K is achieved by applying 7.17Vrms on the electrodes. The magnitude of the ACET force and temperature increment can be analytically estimated. Suppose that the chamber height is h microns, given the potential difference of V on electrodes, we have $|E|=|-\nabla V|=V/h$ and the power dissipated per unit volume is

$$W(h)=\sigma E^2=\sigma V^2/h^2 \tag{4-1}$$

Substituting this power representation into temperature balance equation Eq (2-11) gives:

$$k\nabla^2 T=-W(h)=-\sigma V^2/h^2 \tag{4-2}$$

Let y represent the distance from high potential surface in vertical direction. The boundary conditions at $y=0$ and $y=h$ is $T=0$. That gives a general solution of T as:

$$T(y)=\frac{\sigma V^2}{2kh}(y-\frac{y^2}{h}),\ and,\ \nabla T=\frac{\sigma V^2}{2kh}(1-\frac{2y}{h}) \tag{4-3}$$

We can see that the temperature gradient is maximized at electrodes and zero at $y=\frac{h}{2}$, which is in agreement with simulation results. The maximum temperature rise can be calculated from Eq (4-3). At $y=\frac{h}{2}$, $\Delta T_{\max}=\frac{\sigma V^2}{2kh}\cdot\frac{h}{4}=\frac{\sigma V^2}{8k}$. The time averaged ACET force per unit volume is:

$$<F_{et}>=[\frac{0.024}{1+(\omega\tau)^2}-0.002]\cdot\frac{\varepsilon\sigma V_{rms}^4}{2kh^3}(1-\frac{2y}{h}) \tag{4-4}$$

For 7.17Vrms used in experiment, the maximum of electrothermal force is approximately $60.6\ N/m^3$ and the temperature rise is 2.41K. The simulation gives result of 2.44K as shown in Fig 3-7. Both are close to experiment measurement of 2.1K

temperature rise.

Our experiment has shown that the fastest particle motion, i.e. fluid velocity, occurs at ~20 microns above the wafer surface, which is in agreement with the simulation results. This is consistent with the characteristics of ACET flows, since electrothermal effect induces volume force on the fluid, and fluid velocity at the boundaries is zero according to no-slip condition.

From Eq (4-4), we know that ACET velocity is expected to follow a quartic relationship with respect to the applied voltage. The voltage dependency of fluid velocity was experimentally studied in the particle trapping experiments by varying the applied voltage from 11.9 V_{pp} to 22.7 V_{pp} at 200 kHz.

Fig 4-2 gives a comparison between velocities from theoretical prediction (quartic dependency to applied voltage $0.000303V_{p\text{-}p}{}^4$ or $0.0194V_{rms}{}^4$), curve fitting and

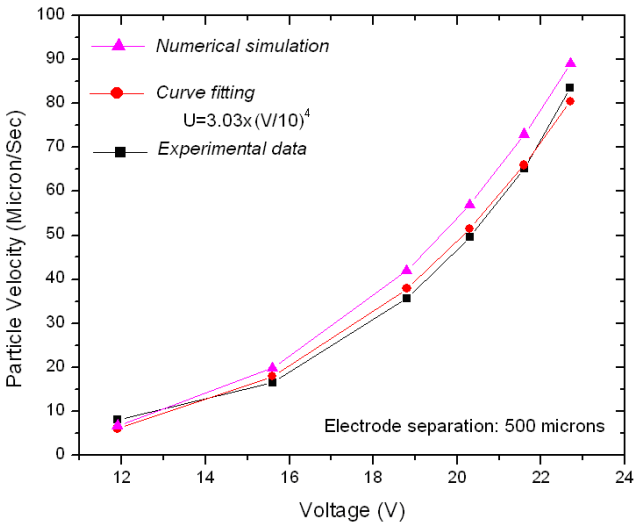

Figure 4-2 Particle velocity as a function of applied voltage. Three data sets are from simulation (triangle), curve-fitting (dot), and experiments (square).

experimental measurements. The data sets exhibit a close agreement. Simulated velocities are slightly higher than experimental data. As the applied voltage increases, ACEO fluid velocity goes up as V^2, while $u_{ACET} \propto V^4$, the contribution from ACEO becomes less noticeable.

4.2.2 ACEO

From frequency dependency of ACEO mentioned in chapter 2, its influence to fluid motion at 200 kHz is minimal. To further identify that ACEO is not responsible for the observed fluid motion, we perform a hand calculation of the ACEO velocity according to Helmholtz-Smoluchowski equation. For sodium chloride, the molar conductivity Λ of Na^+ and Cl^- is 50 $S \cdot cm^2 / mol$ and 76 $S \cdot cm^2 / mol$, respectively. The ion concentration n_0 in fluid is calculated from equation $n_0 = \sigma / (\Lambda_{Na^+} + \Lambda_{Cl^-}) = 0.0178 mol / L$ and the Debye length is 2.3 nm. The double layer capacitance is given by $C_{dbl} = \frac{\varepsilon}{\lambda_d}$, in this case, equals to $0.3 F / m^2$. Zeta potential takes the form of $\zeta = \frac{1}{2}(V - IR_f)$, where V is the applied voltage and I is the current through fluid. So,

$$\zeta = \frac{1}{2} V (1 - \frac{R_f}{R_f + j \frac{2}{\omega C_{dl}}}) = \frac{V}{2 + j \omega R_f C_{dl}} \qquad (4\text{-}5)$$

The value of zeta potential from Eq (4-5) is about one thousandth of applied voltage at 200 kHz. From the Helmholtz-Smoluchowski equation, we estimate the ACEO velocity in parallel trapping device to be less than 1 micron/s. This calculation leaves out the non-linearity of double layer potential drop. The actual ACEO velocity could be even

smaller.

4.2.3 DEP force

One thing worthy to note is that in Fig 3-9b, the boundaries between electrodes and non-electrodes were also highlighted after experiments which showed a sign of particle aggregation under positive DEP (pDEP) force. The explicit form of DEP force is shown in Eq (2-14). The estimation of DEP velocity can be done by using the friction factor. Stoke's law states that the frictional force exerted on spherical objects in viscous-dominating fluid (i.e. small Reynolds number) is $F = 6\pi\eta a U$, where η is the viscosity. If we ignore the term associated with travelling wave signal, the DEP velocity is written as:

$$U_{DEP} = \frac{F_{DEP}}{6\pi\eta a} = \frac{2\pi\varepsilon a^3 \,\mathrm{Re}(f_{CM})\nabla E_{RMS}^2}{6\pi\eta a} = \frac{\varepsilon a^2}{3\eta}\mathrm{Re}(f_{CM})\nabla E_{RMS}^2 \qquad (4\text{-}6)$$

At the kHz frequency range, the real part of Clausius-Mossotti factor is close to 1. Under such conditions, the ratio between ACET and DEP velocity is [45]:

$$\frac{U_{ET}}{U_{DEP}} \propto \frac{\sigma V^2 r^2}{a^2} \qquad (4\text{-}7)$$

r is the distance between particle and electrode edge in polar coordinates. From Eq (4-7) we can see that the DEP velocity scales with ACET velocity when r is comparable to the particle radius. However, this ratio attenuates rapidly as the distance increases. Therefore, the DEP force only has influence to those which are very close to the surface. The simulation picture (Fig 4-3) shows that DEP velocity can be largely neglected except for particles located very close to the surface. The DEP velocity simulation was incorporated to the ACET model to provide a comprehensive view of flow pattern in chamber (Fig

4-4). Notice the arrows located close to electrode edge point downwards (shown in box). The vertical component of DEP velocity attracts particles onto the surface. When it wins the competition against the viscous drag, particles are immobilized. Particle velocities close to the edges are enhanced by including the pDEP effect in simulations ($57\ \mu m/s$ versus $109\ \mu m/s$). This result adds to the ACET flow which produces counter flow and the combination of two mechanisms causes the trapping to be more effective.

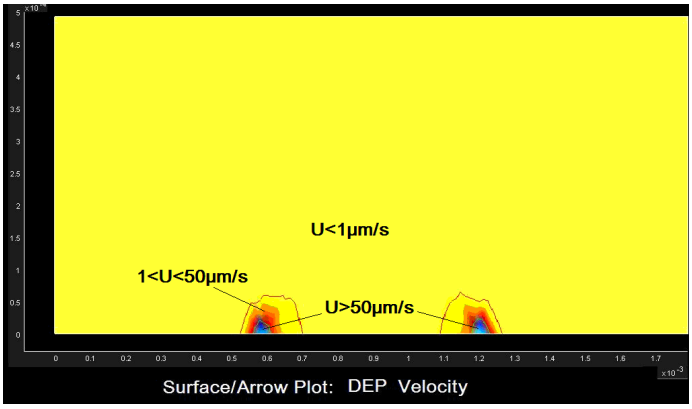

Figure 4-3 Simulated magnitude of DEP velocity

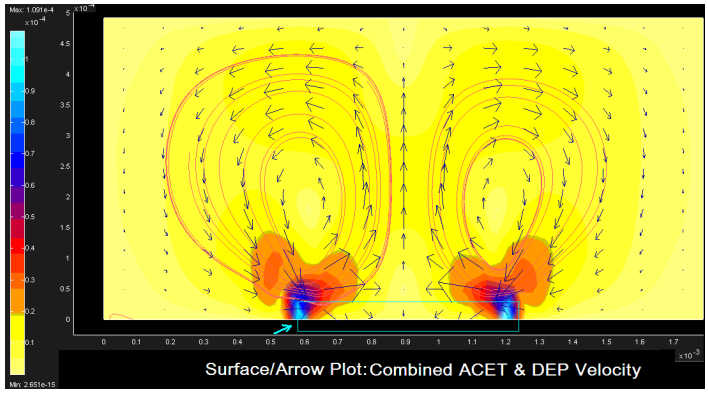

(a)

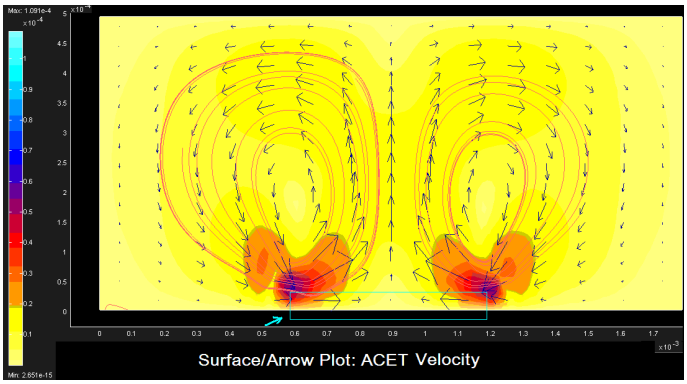

(b)

Figure 4-4 Comparison of simulation pictures (a) combined DEP effect with ACET (b) ACET only

4.2.4 Buoyancy force

Natural convection, or buoyancy, has the ability to introduce vortex-like flow pattern at the presence of temperature rise in fluid. A simulation picture is shown below (Fig 4-5). Different from AC electrothermal, buoyancy force is related to the magnitude of temperature rise instead of local temperature gradient, which causes the fluid to move from high temperature region to low temperature area. The magnitude of buoyancy force equals to the weight of fluid displaced by the body and can be represented as

$$f_g = \Delta\rho_m g = \frac{\partial\rho_m}{\partial T}\Delta T g \qquad (4\text{-}5)$$

Notice that this formula does not have frequency term. However, at very low frequencies, chemical reaction happens prior to the heat convection. Electric energy is mostly transferred to chemical energy instead of heat. The magnitude of buoyancy velocity in the simulation below is about four orders of magnitude smaller than electrothermal velocity. In experiment, the bulk temperature rise in our parallel trapping

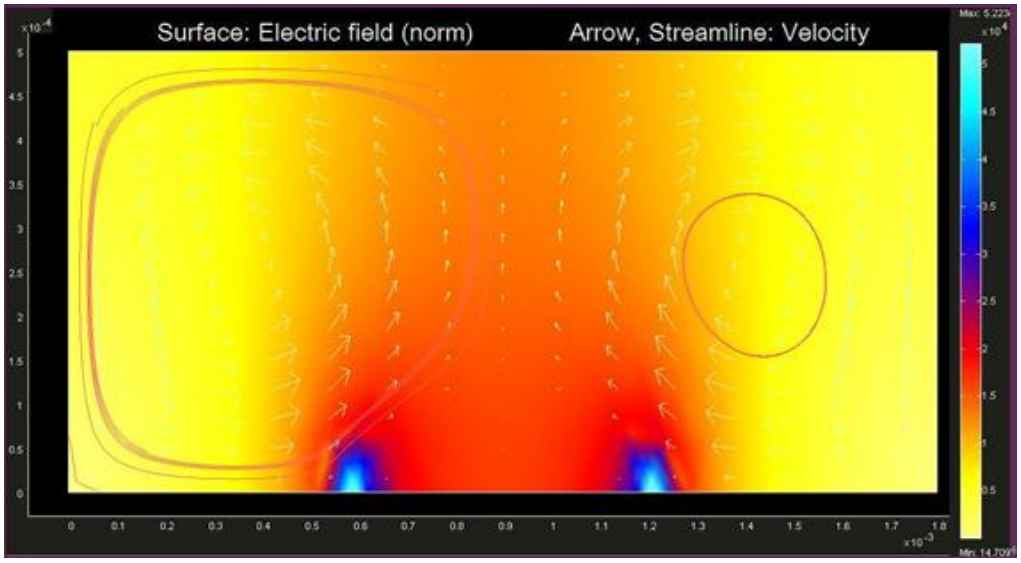

Figure 4-5 Simulated buoyancy induced fluid flow in parallel trapping device

device is 2.41k at the voltage of 7.17Vrms (section 3.2.1). In this case, $\frac{1}{\rho_m}\frac{\partial \rho_m}{\partial T} \approx 10^{-4}/\deg ree$. Hence we can calculate the magnitude of buoyancy to be $f_g \approx 0.00237 N/m^3$, much less than the electrothermal force ($60.6255\ N/m^3$). Therefore the buoyancy force is negligible compared to the electrical forces.

4.2.4 Brownian motion

Brownian motion refers to the erratic and constant movements of particles in a liquid (or gas) environment. It is a stochastic process and over time the distribution of the random displacement of particles follows a Gaussian profile. For the two dimensional case, the particle displacement due to Brownian motion has a zero mean and approximated standard deviation of $\Delta = \sqrt{\frac{k_B T}{3\pi a \eta} t}$, where a is the particle radius, T is

the temperature, t is the period of operation. For the 500nm particles that are used in our trapping experiments, the standard deviation of particle displacement due to Brownian motion is about 0.025 nm/sec. In experiment we records particle velocities at the order of tens of micron per second. Therefore, since the particles move at a speed a thousand times faster in a deterministic way, we can ignore the effect of Brownian motion.

4.2.5 Gravity

In fluid dynamics, the velocity due to gravity is given as $u_g = \frac{2}{9}\frac{a^2 \Delta\rho}{\eta} g$ [28], where g is the gravitational acceleration, $\Delta\rho$ is the density difference between particles and fluid. To a first order approximation, this density difference is of the order of fluid density. For particles of micrometer scale, the velocities due to gravity usually have the magnitude of few nanometers per second. We calculated that in our experiments, particle velocity due to gravity is approximately 0.1nm/s. At such a speed, it would take a few days for the gravity to deposit the suspending particles onto the solid surface. Similar to the Brownian motion, the gravity is not taken into consideration in measuring particle velocities.

4.3 Summary

The impedance analysis discussed in this chapter provides insights to the electric behavior of fluidic system at operating conditions. It illustrates the dominance of ACET flow from a quantitative point of view. The effect of ACEO is estimated using circuit model and it is shown ACEO is not strong enough to induce noticeable fluid flow in our experiments. Effects of other factors including buoyancy and DEP force are also analyzed.

The conclusion is that ACET effect induces major bulk flow in both trapping and pumping devices, whereas DEP assists in attracting particles to the electrode surfaces. However, due to the short effective distance of DEP force, the main fluid flow still follows ACET induced pattern.

Chapter 5. Microfluidic flow reversal at low frequency by AC electrothermal effect

Flow reversal is an intriguing phenomenon in AC electrokinetics. To expand the application scope of ACEK, it is imperative that ACEK microflows can be very well predicted and controlled, which motivates the research on ACEK microflow reversal. Several research groups have observed that under certain operating conditions, microflows reverse their directions due to a small change in the applied AC electric signals. This chapter describes a flow reversal phenomenon caused by AC electrothermal effect. Fluids with conductivities of $2 \cdot 10^{-4} S/m$, $0.02 S/m$ and up to $0.1 S/m$ were experimented at frequencies ranging from 1 kHz to 110 kHz. Flow reversal was observed only at low frequencies (~1 kHz) for $\sigma = 0.02 S/m$. Analysis of system impedances and simulation of power consumption lead us to conclude that the distribution of electric power consumption is dependent on conductivity and AC frequency. As a result, when more electric power is consumed at the surface/electrolyte interface rather than within the fluid, both the location of temperature maximum and the directions of temperature gradients will be changed. Therefore the direction of AC electrothermal force is reoriented, causing the flow reversal. The model which accounts for this surface heating is simulated using calculated power dissipation from impedance analysis and results are in agreements with experiments. Having gained the knowledge of how temperature gradients influence the flow directions, we proceed to investigate the possibility of waste heat harvesting by ACEK micropumps. Numerical simulation has been performed that supports our concept.

5.1 Introduction to ACEK flow reversal

It has been observed by several groups that ACEK mechanisms may reverse the flow direction upon a small change in pumping parameters, such as AC frequency or voltage. Most of the reversal applications are seen in micropumping. To expand the application scope of ACEK, it is imperative that ACEK microflows can be very well predicted and controlled, which motivates the research on ACEK microflow reversal. Flow reversal happens mostly in ACEO devices [46] [47] [50] [67] [68]. Using an array of asymmetric planar electrodes and KCL solutions at about $1.5e^{-3}$S/m, Studer et al. [2] reported the reversal of their ACEO pumping direction at relatively high frequencies (50-100 kHz) and high voltages (up to 6 V_{rms} with 4.2 μm in-pair electrode gap). Wu et al. [69] and Lastochkin et al. [70] reported ACEO flow reversal by Faradaic charging in deionized water. Urbanski et al. [33] observed flow reversal in their 3D step ACEO micropump at frequencies over 10 kHz and voltages beyond 2 Vrms using deionized water, and they reported that flow reversal threshold voltage increases as the increase of the operating frequency. Yang et al. produced back and forth microflows in their T-shape electrodes by changing AC frequency between 1 kHz and 1 MHz [71]. Gregensen et al. described an observed flow reversal at low frequency (~1 kHz) and low AC voltage (~1Vrms) [72]. They attributed this phenomenon to possible Faradaic electrode reactions.

Several different mechanisms have been used to explain the flow reversal. Induction of co-ions from reactions at 2 Vrms, 100 Hz is responsible for flow reversal in [47]. At high voltage and high frequency as in [71], ACET dominates over ACEO and the pin-structured electrode design causes the opposite flow direction of ACET effect. In

middle frequency range (1 kHz to 100 kHz) where ACEK devices most likely to operate, refs. [73] and [74] suggest Steric effect as responsible for flow reversal. When voltage induced at double layer exceeds the small perturbation requirement, charges in the diffuse layer of the double layer are considered "crowded" and cannot be regarded as closely packed at the electrode surface. Therefore, the double layer capacitance decreases, which affects the charging time (response time) of the electrodes. In a planar electrode system, a pair of electrodes with unequal width has different charging times for its two members, and the narrower electrode can respond to a higher frequency than the wider electrode. At relatively high frequency (10−100 kHz), the wider electrode loses its ability to generate ACEO surface flow, and the net flow will follow the surface flow on the narrow electrode. As a result, the pumping direction reverses. In steric effect, the surface flows on each electrode maintain their directions from the inner edge to the outer edge, and the flow reversal is caused by the change of dominance from the wide electrode to the narrow one.

Flow directions in an ACET device can also be reversed by modifying its thermal boundary conditions. Ref. [75] has shown by simulation how thermal conductivities of the substrates affect ACET flow directions. Their work studies traveling wave ACET systems with silicon and glass substrates. ACET flows on a glass substrate move in opposite directions to those on a silicon substrate. Silicon is a better thermal conductor than glass, and conducts more heat away from the Joule heating. Thus, when no external heating is applied, for glass substrate the temperature maxima is located within the fluid, while the silicon substrate pulls the temperature maxima down onto the solid

surface. This subtle difference changes the direction of thermal gradients and therefore, causes electrothermal forces to be opposite in directions.

In our experiments, we have observed strong flow reversal around 1 kHz over a pair of symmetric electrodes. The electrolytes used in our experiments have conductivities of $2 \cdot 10^{-4} S/m$, $0.02 S/m$ (close to tap water), and up to $0.1 S/m$ (saline). We have observed the flow reversal only for the case of $\sigma = 0.02 S/m$ at low frequencies (~ 1 kHz). The steric effect cannot explain the reversal since the flow direction over each individual electrode is reversed. Flow reversal due to Faradaic charging ACEO is unlikely as flow reversal did not occur at higher ionic strengths (where Faradaic charging is more prone to occur). Since Joule heating cannot be neglected for ionic strength of 0.02S/m, we used the impedance data to extract the heat dissipation in the fluid, which showed a change of temperature gradient directions, and hence flow directions. A qualitative agreement is reached between numerical and experimental results.

5.2 Flow reversal experiment

In order to verify that the flow reversal happens on each electrode (not by the dominance of one electrode as steric effect theory implies), a pair of symmetric coplanar electrodes was used in our experiments. The structure of the microfluidic cell is schematically shown in Fig 5-1. The electrodes are 160 microns in width and the gap is 10 microns. We use a polymer microwell (SA8R-0.5, Grace Bio-Labs, USA) to form the fluidic chamber. The chamber height is 500 microns. To observe the movement of fluids, 1 μm latex particles are seeded in the liquid and their trajectories were tracked by a CCD camera (Photometrics CoolSnap ES, USA). The AC voltage magnitude in

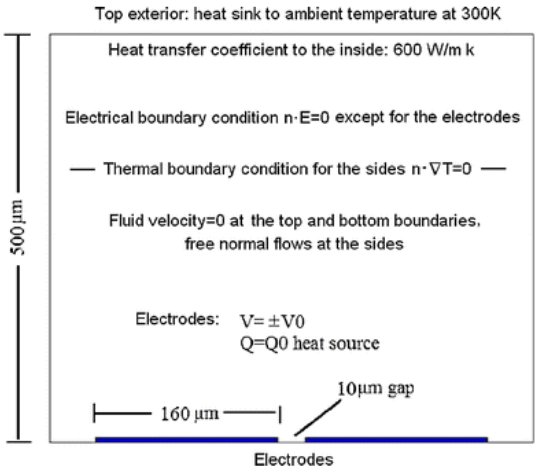

Figure 5-1 Schematic of microfluidic chamber and simulation boundary conditions

experiments was fixed at 5.3Vrms. The conductivities of fluid were chosen as $2 \cdot 10^{-4} S/m$ (referred to as solution A), $0.02 S/m$ (referred to as solution B). More conductive saline solutions (up to 0.1S/m) were also used in experiments, however, no flow reversal was observed.

The experiments were performed at six different frequencies ranging from 1 kHz to 110 kHz. Interestingly, flow reversal phenomenon was observed only for solution B around 1 kHz. At the instant when the AC voltage was turned on, the particles take an initial movement from inner electrode gap to the middle of electrodes, as seen in regular ACEO experiments. Within a few seconds before the flows were fully developed and steady, counter flows started to form, indicated by tracer particles moving in from outer edges of both electrodes and going towards the center gap. As time goes on, the counter flows become strong enough to reverse the original flow directions and form consistent fluid vortices. When the focal plane of the microscope was elevated from the electrode

surface to about 40-60 microns above surface, the particles was observed to move in opposite directions, indicating two counter rotating vortices. Figures 2 (a) and (b) show the velocity curve for solutions A and B.

The velocity data in Fig 5-2 were acquired at the inner edges of the electrodes at the surface level. Five samples were taken at each frequency. Except for the case of 1 kHz, both solutions exhibit similar velocity variation patterns. For solution A, fluid velocity decreases noticeably from 1 kHz to 30 kHz, which is likely due to the transition from ACEO to ACET flows. In this frequency range, double layer impedance still dominates, so ACET forces are weak. However, the electrode polarization cannot respond fast enough to the switching AC field and ACEO velocity goes down rapidly as the frequency increases. At 50 kHz and above, the interfacial impedance becomes negligible compared with the fluid bulk; ACET forces dominate and fluid velocity only vary slightly. For

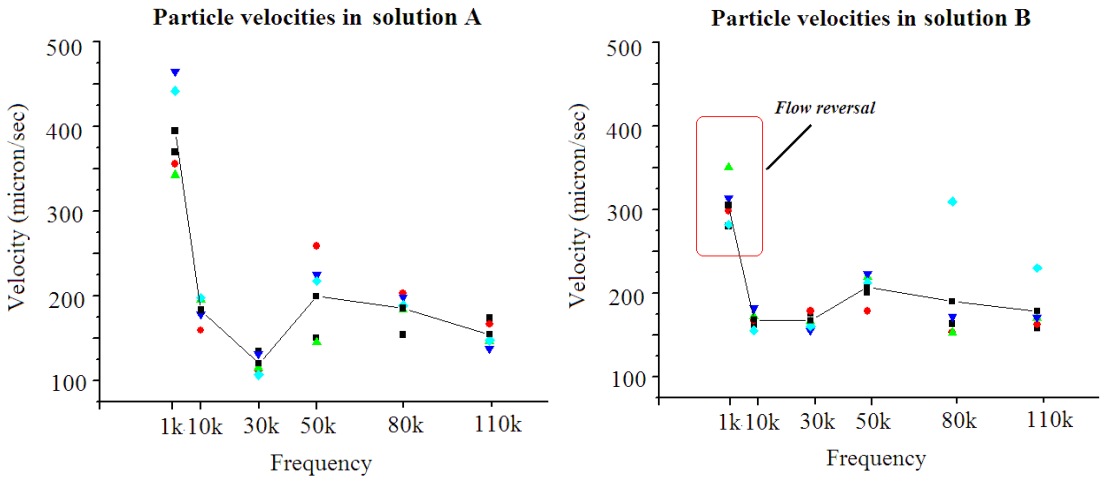

(a) (b)

Figure 5-2 Experiments results of particle velocities for different solution (a) Velocity curve for solution A (b) Velocity curve for solution B

solution B, there is only small variation in fluid velocity, which is because ACET dominates at this ionic strength and there is not much difference in Joule heating of the fluid except for at 1 kHz.

5.3 Impedance analysis

In order to explain the fluidic behavior, the equivalence circuit model shown in chapter 2 is used to access the power dissipation on different parts of the fluidic cell. The fluid bulk is regarded as a resistor. The double layer capacitance is approximated by a constant phase element (CPE), whose impedance has the form of $Z = \frac{1}{j\omega C_{dbl}} \approx \frac{A}{(j\omega)^{\beta}}$.When β is 1, the CPE model describes the behavior of an ideal capacitor. In our case, the values of β are between 0.65 and 0.85. Therefore it is indicated that interface does not behave as an ideal capacitor and a resistive term needs to be included. At very high frequencies, AC electric field pass through the fluid by dielectric coupling between the electrodes, i.e., the fluid is equivalent to a dielectric medium and it is represented by $C_{dielectric}$. The dielectric capacitance is usually several magnitudes smaller than the double layer capacitance. Therefore, its influence will not manifest until at high frequencies. The modified equivalent circuit model is presented in Fig 5-3.

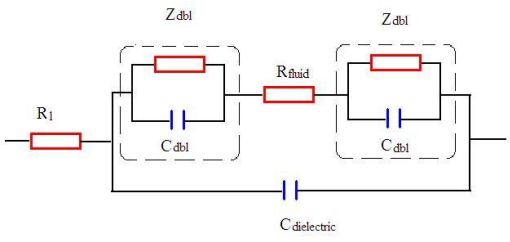

Figure 5-3 Modified equivalence circuit model

Figure 5-4 shows the impedance spectra for solution A and B (bottom). Both spectra show a decrease at low frequencies that is attributed to the double layer capacitance. At middle frequencies range, the fluid resistance causes most of the voltage drop and the plots exhibit a more flat slope. At higher frequencies, the dielectric capacitance dominates and the impedance magnitude decreases at -20 dB/decade, as in any RC filters. The values of the components in the equivalent circuit of Fig 5-3 were extracted by curve-fitting of Fig 5-4 and impedance simulation with Matlab. Good agreement can be seen between the measurements and the extracted equivalent circuit. Table 5-1 lists the extracted component values.

	Solution A	Solution B
40	120K	37K
100	83K	18K
1K	46K	4.6K
10K	12.2K	2.7K
50K	2.7K	1.7K
200K	670	620
Extracted Parameters		
A	3.30E+06	3.60E+06
β	0.6788	0.8424
R_fluid(Ω)	43K	2.4K
C_d(F)	1.20E-09	1.20E-09
Surface Impedance	$Z = A/(j\omega)^{\beta}$	

Table 5-1 Impedance values and extracted parameters

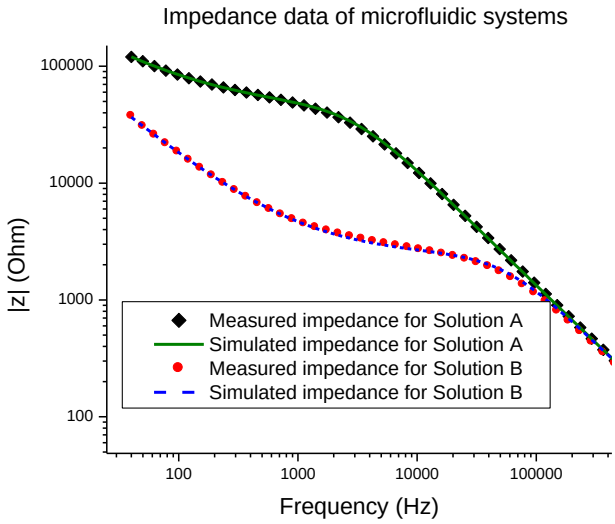

(a)

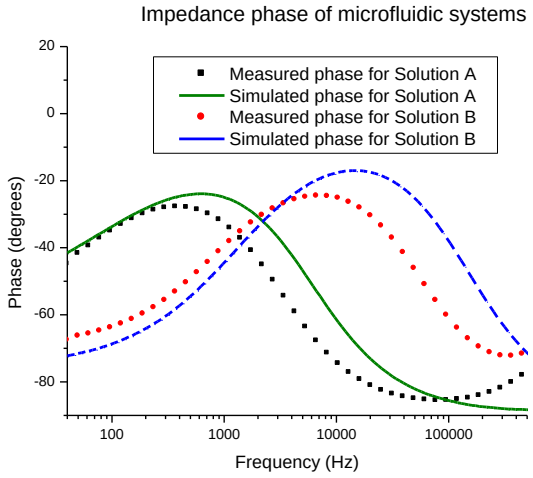

(b)

Figure 5-4 Impedance spectra of the microfluidic system. Black: solution A. Red: solution B. Lines are the fitted values. (a) Magnitude. (b) Phase

With the impedance values, the heat generation at each impedance component is calculated as a function of AC frequency. Fig 5-5 compares the heat dissipation at the surface and in the fluid. For solution A, the large fluid resistance value indicates that at all frequencies more voltage is dropped over the fluid, leading to consistent higher power consumption in solution. Nevertheless, at low frequencies, ACEO flow has a higher velocity magnitude than ACET flow. For solution B, the heat dissipation has a very different pattern from that of solution A as shown in Fig. 5-5(b). At low frequencies (~ 1 kHz), more voltage drops at the electrode interfaces than over the fluid, hence more heat dissipates at the electrode surfaces. With increasing frequency, the impedance of the double layer goes down, and the differences of heat dissipation between two parts are reduced. According to Fig. 5(b), the heat dissipations on electrode and in fluid bulk equal each other at approximately 3 kHz, beyond which the fluid heating again dominates. As a result, the temperature maximum in solution B will move as a function of frequency.

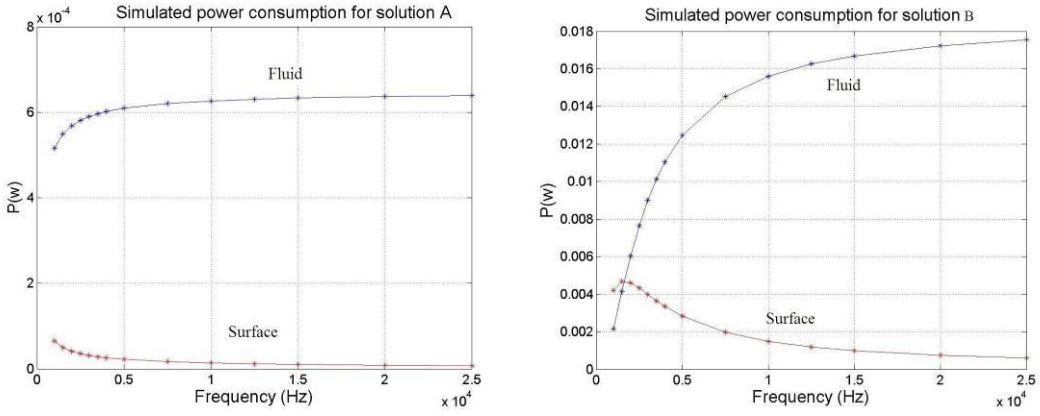

(a) (b)

Figure 5-5 Power consumption plot for different solutions, (a) solution A (b) solution B

5.4 ACEK Numerical Modeling

In simulation, electrodes are commonly considered as ambient temperature and it applies to most of the situations for conductive solutions. For this particular case as the power calculation suggests, we need to take into account the heat generation at the electrode surface. Therefore in the flow reversal model, we define electrodes as a heating source in the thermal module. The heating power per unit area derived from energy dissipation and the actual electrode size is given as 3125 W/m^2 for 1 kHz and 1172 W/m^2 for 10 kHz. The cover of our fluidic chamber is made of plastic. Therefore, it is treated as a contact layer to room temperature with an estimation of heat transfer coefficient ($h = 600 W \cdot m^{-1} \cdot K^{-1}$). The fluid inlet and outlet are assumed to be thermal insulation since no heat exchange happens on these boundaries.

Fig 6 gives the simulated ACET flow profile at $\sigma = 0.02 S/m$ (solution B), and three situations are considered. Fig 5-6a and b are both for frequency of 1 kHz. Joule heating in fluid is limited to a low level due to large impedance at low frequencies. Electrodes in Fig 5-6a are treated as a thermal conductor with no surface heating. The area with considerable temperature rise is confined within the electrode gap where electric fields concentrate. The thermal force is directed from the inner gap towards the outer electrode edges, pushing fluids outwards and pulling down the fluid in the middle because of mass conservation. When surface heating is accounted and its magnitude is larger than bulk heating (Fig 5-6b), the temperature gradient points from the surface where the highest temperature is and fans out into the fluid bulk. The resulting thermal force becomes pointing upwards in the middle, and therefore forms vortices in opposite directions to those in Fig 5-6a. The simulation dictates the flow reversal as revealed in experiment.

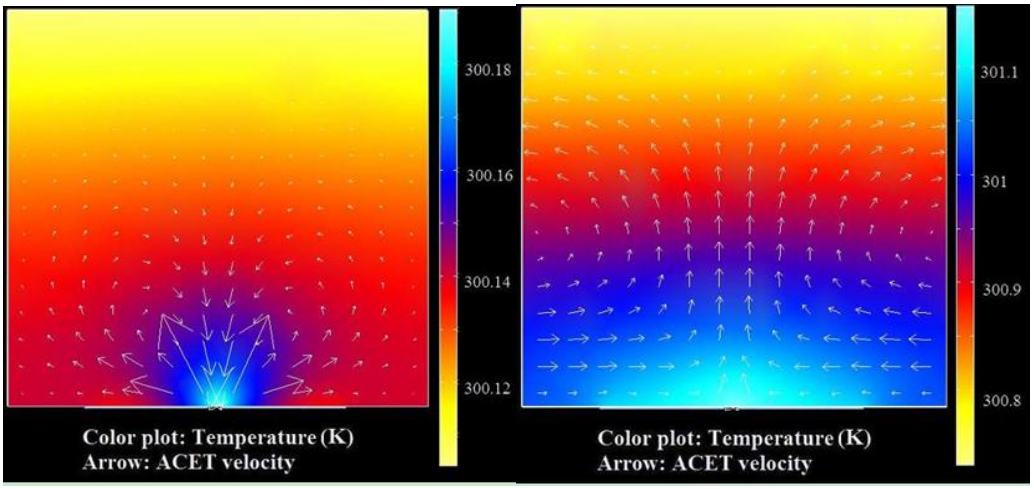

(a) (b)

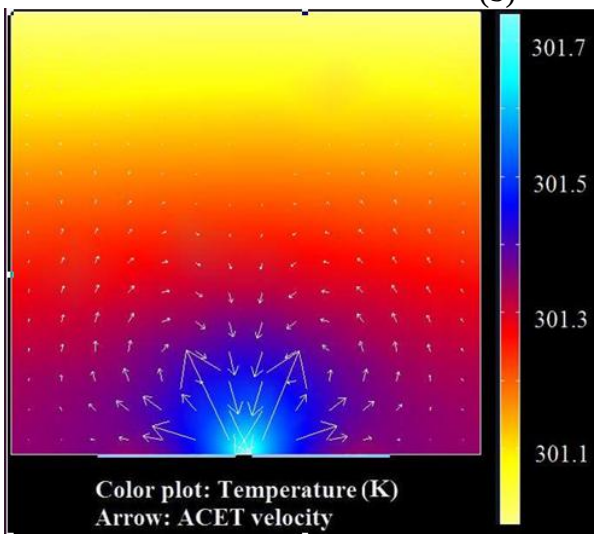

(c)

Figure 5-6 Numerical simulation results for solution B, (a) when no surface heating is included at f=1 kHz, the fluid keeps temperature maxima inside it by generating uneven Joule heating. (Vrms=1.8V. Q=0) (b) surface heating is included at f=1 kHz (arrow length not to scale). Higher power consumption at surface in tap water solution drags down the temperature peak and causes the flow reversal.(Vrms=1.8V, Q=3125W/m2) (c) at high frequencies (~10 kHz) Joule heating takes dominance again even when surface heating is considered. Flow exhibits regular pattern. (Vrms=4.84V, Q=1172 W/m2)

Simulated magnitude of reversal flow is however one order smaller than the experiment (tens of $\mu m/s$ compared to hundreds of $\mu m/s$). Fig 5-6c shows the velocity and temperature profile at 10 kHz. The surface heating becomes less important in magnitude when compared with Joule heating. Similar to Fig. 5-6a, the high temperature area is limited to a small region around the electrode gap, so the regular ACET flow direction is resumed. The simulated velocity in Fig. 5-6c is at the order of hundreds of $\mu m/s$, which is directly comparable to the experiment data.

The study into flow reversal that we carried out in this chapter is more than academic exercise. It provides us with insight into various factors that could modulate ACEK flow. It also leads us to speculate that ACET effect can be used for waste heat scavenging. If heat flux from below the electrodes can reverse the flow direction, a high heat flux from the above should be able to increase pumping velocity. Thus, the flow velocity can be enhanced with a magnitude proportional to the given temperature gradient as Eq (2-16) shows. Some numerical simulations have been performed and the results are shown below.

In Fig 5-7a, the micropump model with electrode dimension of 10/10/50/50 is simulated with an external heating of 10 mw from top boundary. Fig 5-7b is the controlled case with only self heating by electrodes. The fluid conductivity is set at 0.002 S/m. Both plots use the same color scale. With the aid of external heating, the peak velocity ($318.4\,\mu m/s$ vs $48.4\,\mu m/s$) and flow rate ($4.42\ \ \mu L/s$ vs $0.54\,\mu L/s$) are both one order of magnitude higher. This property is very desirable as micropump for microcooling applications. The flow rate will increase to take more heat away as the chip gets hotter, so to realize a self regulating feedback loop.

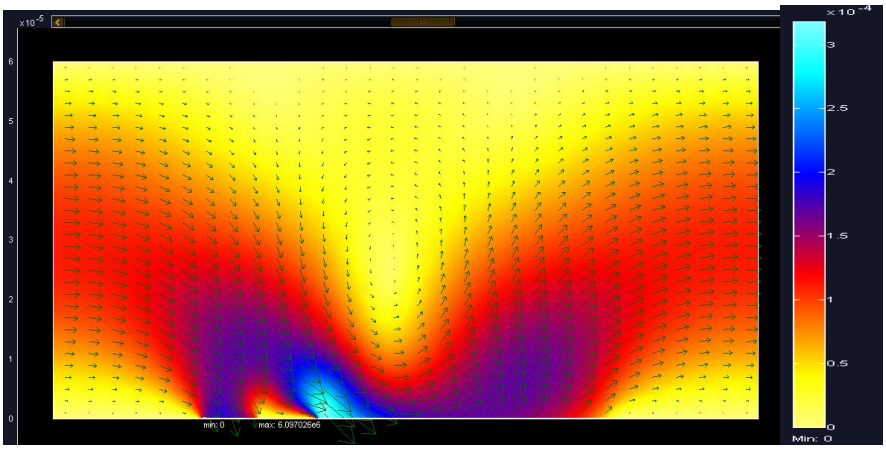

(a) Velocity plot when external heat (10mw) is applied to the top boundary

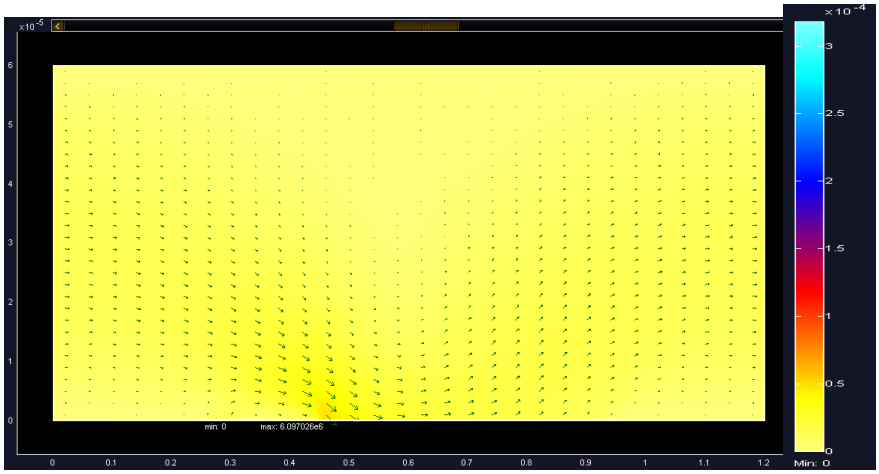

(b)Velocity plot with no external heating

Figure 5-7 Simulation results show the effect of external temperature gradient

5.5. Low frequency electrode processes and conclusions

To be exhaustive about possible causes of flow reversal, here is more discussion on how our observation is unlikely due to ACEO flows. At low frequencies (well below charge relaxation frequency $\omega = \sigma / \varepsilon$), ACEO typically will generate a higher fluid velocity than ACET. ACEO certainly contributes appreciably to the velocity data in Fig 5-2a for frequencies below 10 kHz. The influence of ACEO decreases with frequency and ionic strength of the solution, while the relevance between ACET velocity and

frequency is not obvious in our experiment conditions. The frequency dependency of ACEO fluid flow was documented in [67]. Using their results as a reference, solution A should show a peak in velocity well below 1 kHz and the solution B should have a velocity peak between 2 kHz and 10 kHz. Our velocity data in Fig. 5-2a agree with the ACEO characteristics, while those in Fig 5-2b do not, indicating that mechanism other than ACEO should be responsible. Previous research of ACEO flow in symmetric electrode system shows the existence of two minor counter rotating vortices near the outer edges of electrodes [36][77]. Such vortices result in the stagnant lines on the electrodes where tracer particles are found to deposit. ACET effect does not produce counter vortices, and hence, no particle assembly lines on the electrodes. In our experiment, we have observed particle line aggregation at 1 kHz for solution A, however, not for other solutions with higher ionic strengths or higher frequencies.

To sum up, an interesting flow reversal at low frequency was observed in our experiments. Since ACEO and conventional Joule heating based ACET theories cannot account for this phenomenon, an ACET flow reversal mechanism is explained using surface heating. Using an equivalence circuit for the microfluidic system, we are able to illustrate the frequency dependence of ACET microflows. Increased dissipation of electric energy at the electrode surface leads to the change in temperature gradients and ACET flow pattern. Such study of flow reversal helps understand ACET effect and realize reliable control of microfluidic devices.

Chapter 6. Reaction-Enhanced Fast ACET pumping

In previous experiments, ACET pumping velocity was recorded on the order of 100 $\mu m/s$ at 6.65 Vrms (18.8 Vpp), 200 kHz and with a fluid conductivity of $\sigma = 0.224 S/m$. Such velocity levels are comparable to the results from other research groups, and usable for bio-sample applications. However, a dramatic increase of velocity from the range of $\mu m/s$ to mm/s has been achieved in our follow-up experiment by intentionally inducing a layer with high density charges, which is done by superimposing a DC offset voltage over the AC signal. The maximum velocity reaches 2.5mm/s at 4.42 Vrms, 100 kHz with a -2V dc bias. By controlling the level of dc voltage, we can achieve much higher pumping efficiency without dealing with the side effects of electrolysis. Such a finding adds a viable method to the current micropumping families. The experiment process and results are presented in the following sections. Section 6.1 gives an introduction to electrolytic basics that helps to understand Faradaic (electrochemical) reactions. Section 6.2 describes reaction enhanced ACET effect and shows numerical simulation results. Section 6.3 presents experimental results and discussions to.

6.1 Electrolytics

Electrolyte is a substance that will dissociate into free ions which make the substance electrically conductive. The charge carriers in an electrolyte are mobile ions bounded to respective material atoms. This is different from metals. In metals, electrons at the outermost layer in metal molecule are loosely attached to atom. They are more like an electron gas not linked to a certain atom, but with a probability of being at a certain

location at a certain time. The reason that current flows fast in metal is that it is not the same electron entering and leaving. Electronic current implies no transport of substance. Therefore, an externally applied dc current can flow forever without changing the substance. On the contrary, ionic conduction in electrolytes depends on the migration of ions, and typically, is much slower in speed (of the order of tens of mm/s [78]). The ionic current implies the transport of ions, which can be depleted with an external applied dc current (electrolysis). New solid material like organic polymers and glasses may contain an appreciable amount of ions that are free to move, so the notation of electrolytes is not limited to liquid media. Some solids show both ionic and electronic conduction.

The ionization of electrolyte is of particular importance to conductivity and heat generation. Atoms with outermost shell structure closer to configurations of noble gas are more likely to gain or lose electrons and reach the stable form, and thus, easier to be ionized when hydrated. Electronegativity is the relate ability of an atom to gain electrons and become a negative ion. Pauling scale is often used as a measure of electronegativity. Atoms with particular large or small Pauling scales are more inclined to reach the stable form and ionized than atoms with a medium Pauling scale. An example will be the sodium chloride solution. Na has a Pauling scale of 0.9 and Cl of 3.0. When solvated, sodium and chloride atoms are easily ionized and therefore the solution possesses a considerable conductivity. For ionized atoms, the electrolyte provides such a mean so that ions with different polarities migrate from one electrode to another with opposite directions. This direction is reversed when the signs of voltage switch. Additionally, electron transfer may also happen between solid and neutral species at the interphase. The transport of these species in the bulk of the electrolyte is not by Coulomb force but by a

diffusion process caused by a concentration gradient. Diffusion is essentially derived from the concept of Brownian motion and molecular collision.

As stated in the previous chapters, the processes in the bulk of the solution are very different from the processes at the electrode. The charge redistribution at the interface when electrodes are hydrated leads to the formation of double layer, which is of great importance in the study of microfluidic manipulation. Due to the nature of capacitive behavior of the double layer, its interaction with applied ac electric field has been utilized to developing ACEO flow. The process is much more complicated when a dc signal is added. The electric charges transfer from electrons in electrodes to ions in solution, i.e. the transformation from electronic to ionic conduction. An over potential needs to be reached to induce massive transformation for inert polarizable electrodes such as gold [78]. Hence, the study of interphase phenomena needs to be addressed in order to understand the electrode processes when both AC and DC electric fields are present.

When an electrochemical reaction happens, the charges in the electrode enter the solution and lead to a dc current through the interphase, in contrast to the capacitive, non-faradaic current components in ac case. The amount of electrochemical reaction is proportional to the quantity of electricity passed by the electrolyte, and their relationship is described in Faraday's law of electrolysis, $M = Q/Fz$, where M is the amount of substance produced by electrolysis, z is the valency of the element produced and F is the charge of 1 mole of electron (96472 coulomb/mol). The dc current entering solution is also referred as faradaic current as it obeys Faraday's law. Although it is practically difficult to determine the actual amount of substance involved in electrochemical reaction, we can use particles as flow tracers and gauge the effect of electrolysis by measuring

particle movements along with increased dc voltage.

6.2 Reaction-enhanced pump design

Chapter 4 shows that ACET velocity has a quartic relationship with applied ac voltage. Therefore by tuning ac voltage level, we can achieve good control of pumping performance. Net pumping by ACET has been achieved by asymmetric electrode designs. In chapter 4, net fluid pumping has been shown with electrode pairs of 100/20/180/100 microns, as schematically shown in Fig 6-1. Other designs include orthogonal or 3D electrodes [33] [71].

In this work, we have found that the magnitude of ACET force can be greatly enhanced when we superimpose a dc bias to one of the paired electrodes in addition to ac voltages. A DC offset at the electrodes is intended to induce faradaic charging. Experiments have confirmed that enough voltages will lead to the free ion generation in solution due to faradaic reaction [34]. Therefore, near the surface area, a region of high charge density with much higher local conductivity than its surroundings is formed. The coupling between high conductivity jump and high electric field intensity near electrode surface boosts the fluid flow by a few orders of magnitude.

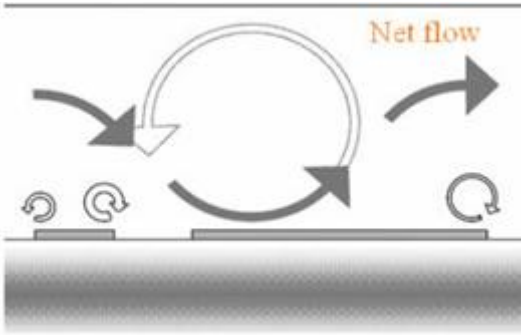

Figure 6-1 Schematic of micropumping using asymmetric designs

In the past, the dc bias approach has been applied in ACEO experiment for directed particle assembly. [79][80] reported a biased ACEO pump fluid using a mixture of ac and dc signals. The velocities exhibit an exponential dependency on voltage with a velocity of ~300 $\mu m/s$ obtained at 4.5 Vpp. The faradaic charging can produce charge densities orders of magnitude beyond the equilibrium density, which is not possible for the regular capacitive double layer charging.

In this research, frequencies at the order of 100 kHz are applied to electrodes; therefore it is unlikely to be the ACEO mechanism as reported in the past. On the other hand, this frequency is way below the transition frequency of ACET, so the fast flow is due to coulomb force. So conductivity gradient is the dominant term as shown in Eq (2-16). The faradaic current causes a sudden conductivity jump (i.e. large $\nabla\sigma/\sigma$) at the interface. Ions in such a layer should not contribute to ACET flow directly. Instead, ACET force magnitude is strongly enhanced at corresponding locations according to the equation $f_E \approx -\frac{1}{2}\frac{\nabla\sigma}{\sigma}[\frac{\varepsilon E_{rms}^2}{1+(\omega\tau)^2}]$. In experiments, high fluid velocities (~mm/s) are recorded. Such results have never been seen in previous publications in ACET researches given similar applied voltages. Comparable velocity levels have been reported by using dc signal alone, nevertheless, the electric field is as high as 10^4V/mm. Our approach of using AC signals lower than 7Vrms and DC offset of 2V provides the benefit of generating high pumping velocities, while at the same time, maintaining a relatively low voltage level [81].

6.3 Experiment results and discussions

We conducted the experiments on reaction enhanced ACET by following the similar steps described in Chapter 3. The gold electrodes in a pair have the width of 10 and 50 μm, with inner and outer gap of 10 and 50 μm, respectively. The electrode arrays are sealed with polymer microchannels of 500 μm in height. The solutions are chosen as low-conductive deionized water ($\sigma = 2e^{-4} S/m$). Sodium chloride solutions at $\sigma = 0.06 S/m$ and $\sigma = 0.1 S/m$ were also used to make comparison with the deionized water solution, in order to test the influence of ionic strength. All solutions are seeded with fluorescent particles of 500nm in diameter (Invitrogen, USA). Fluid velocities are acquired by tracing particle trajectory at 50 μm above the surface. A Tabor signal generator (model# 8551) is used to supply mixed voltages. The dc bias can be added from the "bias" panel with a maximum of 2V. A sample picture taken at 7.07Vrms, 100 kHz and -1.8Vdc using DI water is shown below in Fig 6-2. Multiple particles are in high speed motion. Their trajectories are elongated due to superior velocities.

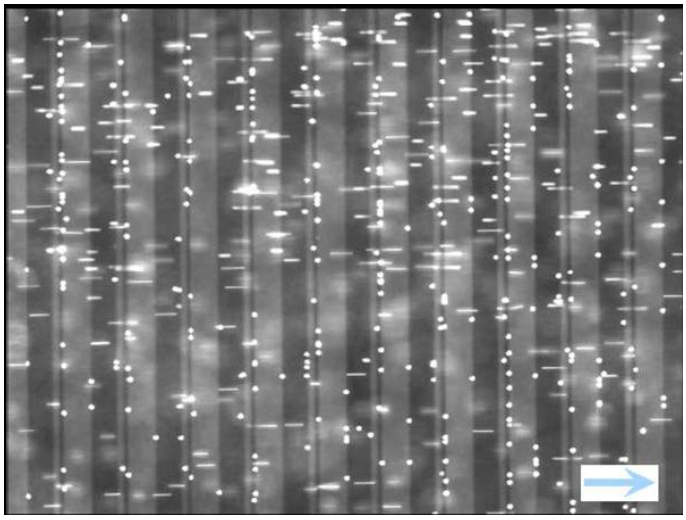

Figure 6-2 Experiment image of fast particle pumping

The pumping velocities were recorded in order to investigate the effects of bias level (Vdc) to pumping velocities. The results are shown in Fig 6-3. Two groups are supplied with 4.42Vrms (12Vpp) and 1.77 Vrms (5Vpp), respectively, as indicated with pink and blue. The frequency is fixed at 100 kHz. For both groups, a general trend of positive correlation between bias level (on either polarities) and pumping velocity is obvious. At small dc bias (<0.4V), the amount of extra ions enter the solution by faradaic current is negligible and the fluid flows does not vary much from the ac experiments. The deionized fluid medium contains too few ions to sustain an ac current large enough and produce noticeable temperature variation and ACET flow. The process of charge transfer between metal electrode and solution becomes more substantial at higher dc biases. The increasing number of ions in vicinity of metal surface creates higher conductivity gradients. Fluid exhibits a much more violent pumping behavior after bias level exceeds the over potential of gold electrode, which appears to be ~$\pm$1. 5V in Fig 6-3. The nonlinear increase of pumping speed with regard to dc bias indicates the existence of an energy barrier in faradaic reactions.

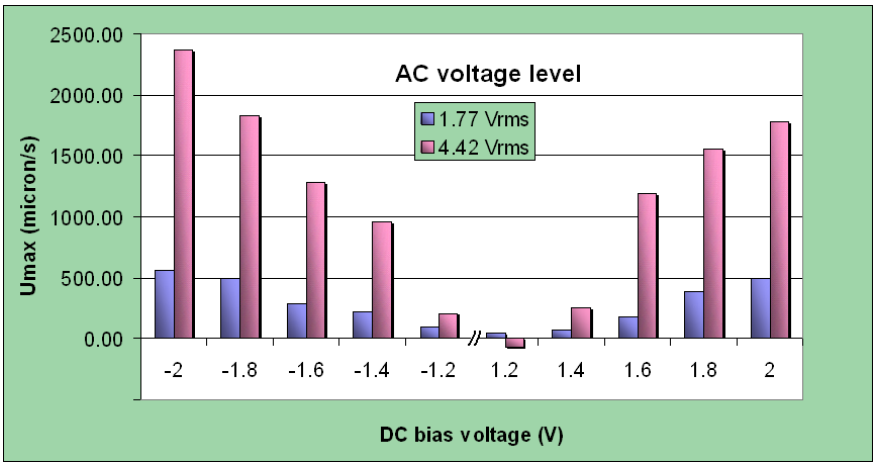

Figure 6-3 Improvement of pumping velocity by dc biasing

The reasoning of energy barrier can be understood in two ways. The reduction potential is defined as the potential difference between metal and the solution when the reduction reaction takes place, i.e. the reaction which ions gain electrons and are reduced to metal. From the perspective of electrochemistry, if the potential is negative, the tendency of metal substance to be oxidized is high and it is more likely to lose outer layer electrons. An example is that sodium ions have a -2.71V reduction potential, indicating nearly no possibility of regaining metal sodium from the ionized form. For Au electrodes, the reduction potential is +1.5V. This signifies not only the energy release at the time of reduction, but also a great tendency of Au ions to gain electrons and return to the original metal form. Therefore it is implied that Au is a highly polarizable metal and only a tiny potion of Au ions enters the solution when wetted. It takes a sufficiently high dc voltage to trigger the reaction and charge transfer, as what is shown in our experiments. Another understanding of energy barrier comes from the view of fluid dynamics. Water hydration has a tendency of creating energy barrier. In the case of a cation in solution, the negative end of water molecules is oriented towards the ion and a sheath is formed around the cation. Outside of the primary hydration sphere, another water molecule may be oriented as well, forming a more loosely bounded hydration sheath. Additionally, absorption is also a potential reason of changing surface property. It is the process of chemical binding of ions to the surface and adds a resistive component to the equivalent circuit as shown in Chapter 5.

Fig 6-2 illustrates very fast positive pumping (here we define the direction from short electrode to wide as positive) velocities for dc bias on both polarities. For bias levels between -1.2V and 1.2V, the fluid pumping is directed to the “negative” direction. The

energy dissipation and surface heating as described in chapter 5 could be applicable to explain the reversal. Similar experiment results are reported by [2] at lower frequency (50 kHz) with no detailed explanations of the causes. As stated above, a sufficiently large voltage is necessary to penetrate the energy barrier in order to conduct massive charge transfer. The ionization of the neutral species such as dissolved oxygen takes place at lower dc voltages before the breakdown [78]. Since species are neutral and do not undergo the electric force, the migration of such merely depends on the concentration gradient. Therefore, at small dc bias voltages, the electron transfer becomes no longer a rate-limiting factor, but rather the diffusion of oxygen to the cathode. The process is that oxygen molecules are reduced and accepting electrons at the negative biased electrode and turn into hydroxyl ions. At the cathode surface, the concentration of oxygen is nearly zero; all available oxygen is reduced immediately. The oxygen molecules in solution are not migrating in the electric field, they move because of the concentration gradient.

In order to further explain the reversal at small dc bias with the lack of empirical data of oxygen dissociation due to difficulties of quantifying during experiment, we update our equivalence circuit model by adding an electrode reaction dc/ac path in parallel with double layer capacitance. A sorption path is also suggested [78] as shown in Fig 6-4. The processes that are considered are:

- Faradaic component: the rate of electron transfer to the electro-active species (typically ions in this case) of the solution. A more specific model may contain an extra Faradaic component describing the amount of species that can be transported to/away from the reaction site from the bulk electrolyte.
- The double layer charging and the sorption of the species at the electrode surface

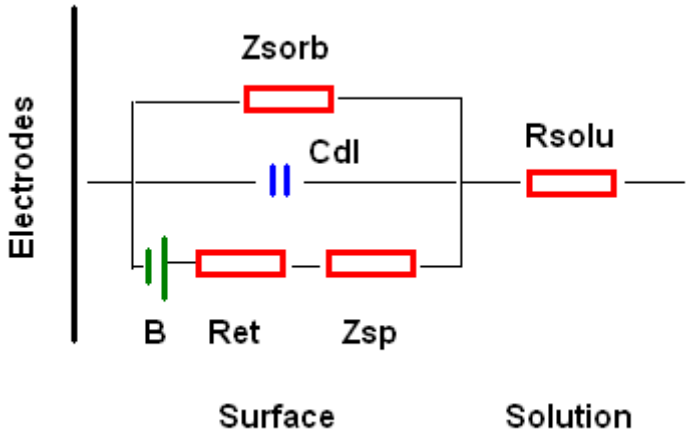

Figure 6-4 Equivalence circuit when chemical reaction takes place

The electrode reaction dc/ac path (faradaic) starts with a dc reduction potential which is determined by the Au electrode and electrolyte, modeled by a battery B to represent the reduction potential. It is in series with a resistor Ret representing the rate of electron transfer at the time of chemical reaction. Ret is obviously related to the activation energy and to the extent to which ions have reached the vicinity of electrode surface so that the electron transfer can occur. A resistor is used to model the process since the reaction is immediate and little transfer time is involved. Ret is current dependent. For polarizable electrodes, it is very large at small dc bias and therefore it is not sufficient to create electrode reaction. Ret only dominates to the extent that electron transfer is the current-limiting process. The impedance Zsp stands for the faradaic impedance which incorporates the slow process admittance Ysp. It is related to the reactions that are rate limited by the necessary time of transport to/from the reaction sites. An example of its dominance is the oxygen dissociation at small dc bias when the value of Ret is negligible. The faradaic current is limited by diffusion alone which is only dependent on concentration gradients.

The capacitive double layer serves as the passage of ac current. It is usually considered as pure capacitive, frequency-dependent in most of the literatures with ideal electrode surface. In chapter 5, we have shown that it is not an ideal capacitor. The double layer impedance is approximated by using the constant phase element model. The capacitance increases with higher ionic strength solutions. It is also suggested [78] to have a distribution of capacitive and resistive properties which values are dependent on the type of metal, the surface condition, the type of electrolyte and the applied voltage.

The additional impedance Zsorp is due to absorption of species at the electrode surface. No electron transfer happens between such species and electrode surface but they do change the surface properties and interfere with the local charge density. Sorption currents are ac currents; however, as the absorption/desorption may occur abruptly at dc voltages, these currents maybe dependent on applied dc bias.

The updated equivalent circuit model accounts for the process of electron transfer at the time when dc bias is present. While dc voltage is remained small (-1.2V to 1.2V in our case), neutral species are ionized at the electrode surface; the faradaic current is generated but mostly diffusion limited. Although the connection between diffusion limited faradaic current and surface heating is not quantitatively presented in this dissertation due to difficulties in measuring the amount of substances involved in surface reaction, one can speculate that the large resistance of Ret would cause the heat from surface being dominating over Joule heating. Therefore, we attribute the flow reversal as a result of reversed temperature gradient which is similar to the case in chapter 5. When enough energy is provided by dc bias ($\sim\pm 1.5$V), the massive electron transfer happens between the electrode and electro-active species in solution. Ret becomes much smaller

and the faradaic current change from diffusion-limited to rate-limited. Abrupt conductivity jump generated by sudden increase of faradaic currents becomes responsible to the high velocity bars in Fig 6-3. The dc biases over 2.0V were also tried in our experiments, electrodes showed a great deal of degradation and gas bubbles were present at the surface. A different chemical process involving water decomposition generates undesired gases as usually seen in DCEK experiments and sabotages the fluid transport.

The importance of ac voltage is illustrated in Fig 6-3. AC field strength is proven to be still influential in generating enhanced pumping velocities. No flow was observed when we apply the dc voltage. This separates our approach from the ion drag pump which depends only on dc voltage and EP phenomenon it utilizes.

Fig 6-5 shows the variation of dc component of a current reading on the 120Ω resistor which is in series with fluidic system per dc bias. Obviously, the current does not linearly increase with dc bias; instead, a plateau is reached after 0.8V and up to 1.4V with a slight increase from initial values. This is the stage where minor scale of electron transfer happens between neutral species and electrode. A steep jump seen between 1.4V-1.8V Vdc matches with the pattern of Fig 6-3, shown a positive correlated

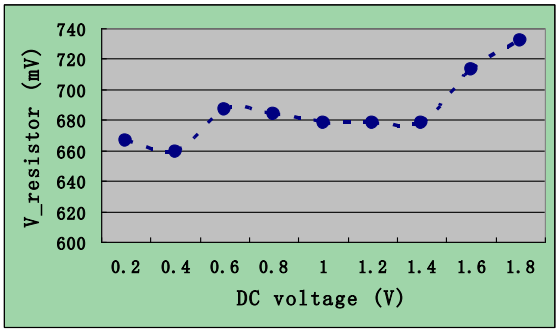

Figure 6-5 The voltage reading from a 120Ω resistor in series with fluidic system

relationship between generated faradaic current and increased pumping velocities. The current data is used in our simulation model to show the increase of pumping speed by considering the effect of faradaic current.

Fig 6-6 compares pumping velocities to various dc bias levels of two different electrodes systems. One has 20 micron, 100 micron for shorter and wider electrode length, and 20 micron, 100 micron for inner and outer electrode gap, respectively. Another system has the whole dimension reduced into half. The velocity pattern shown in Fig 6-5 is similar to what Fig 6-3 shows. Since voltages applied to two electrodes systems are the same, we deduce that the higher electric field strength in the smaller system leads to higher pumping velocities.

The effect of ionic strength on biased pumping is tested in our experiment. Other than deionized water, we have used diluted sodium chloride solutions with conductivities of 0.06 S/m and 0.11 S/m. Under the condition of 7.07Vrms 100kHz AC voltage and using 1 micron particles, both solutions generate similar velocity responses to dc bias as in the DI water case, except the magnitude of fluid pumping is a lot slower. For dc bias

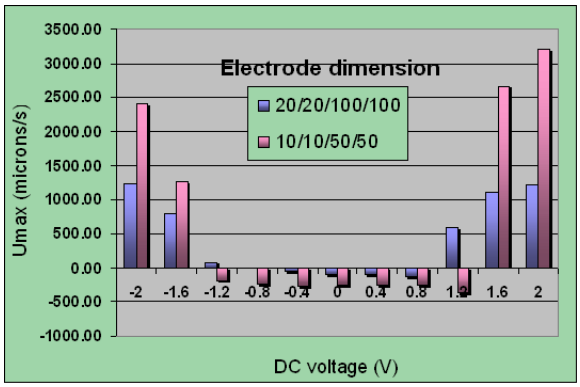

Figure 6-6 Comparison of velocity data between two electrode systems

with absolute value smaller than 1.5V, no sign of fluid pumping is observed. Particles advance slowly to the positive direction when the magnitude of bias level increases, and bubbles are started to be seen at 2V dc. The recorded average velocity for 0.06 S/m solution maximizes at 129.3 μm/s at -1.8V, and for 0.11 S/m solution, maximizes at 41.1μm/s. Great discrepancies in speed (to an order of magnitude) lie between conductive solutions and deionized water.

As stated earlier, when dc bias reaches the level to break down the energy barrier, gold molecules in solid are oxidized by losing outer electrons and transferred into ions. For dilute solutions as used in our experiments, this process is governed by Nernst equations, which states as $E = E^0 - \frac{0.059}{n}\log[Q]$, where E is the actual cell potential, E^0 is the standard cell potential, n is the number of electrons transferred in the reaction and Q is the reaction quotient which is directly related to the ion concentrations in solution. In an electrochemical cell, the actual cell potential E is the chemical potential available from redox reactions. Higher the value, the greater tendency reaction has to take place. As mentioned earlier, the standard reduction potential for sodium ions is -2.71V when hydrogen ions are taken as the equilibrium point (0V). This implies that the extent of the reaction is much greater in deionized solution than in sodium chloride which helps understand the velocity discrepancies measured in our experiments. Additionally, when compared with hydrogen ions as in the DI water case, sodium ions possess a smaller electronegativity (2.1 VS 0.9 as in Pauling scale), indicating a higher probability of being ionized and extended hydration sheath. Therefore, an additional energy is required to stretch the sheath to a new location, which means the voltage needed to sustain a faradaic current is higher for sodium chloride solutions. This is also observed in our experiments

that sodium chloride solution requires a 1.8V activation voltage for reaction as compared with ~1.5V for deionized water.

Another thing to mention is that the reaction happens on anode and cathode is different. At anode, gold is oxidized into ions and enters the solution with faradaic current. When dc bias is over 1.5V, the oxidation process dominates over the reduction reaction happens at cathode in terms of generating aggregated ion layers near the surface. In another words, the reaction enhanced ACET flow is mainly boosted by the reaction and formation of conductivity gradient at anodes. Since we use asymmetric geometry, the charge density is higher on short electrode and so is the current density and electric field strength. Thus, by combining the factor of larger extent of ion generation at anode and large electric field strength on short electrode, we can choose the best combination in order to achieve higher pumping performances. We have observed that negative bias produces higher velocities in Fig 6-3 but the opposite in Fig 6-6. By carefully examining the experiment apparatus, we have figured that, in Fig 6-3 dc bias is applied to the wide electrode which leads to the fact that negative bias favors more in terms of pumping speed when the short electrode is treated as the anode. In Fig 6-6 a different experimentation causes bias being applied to the short electrode and thus positive bias produced higher pumping speed. This is also found true in the experiments using conductive solutions.

Fig 6-7 shows the velocity data taken at different channel height. The reaction enhanced ACET flow is more similar to be a surface flow. This is well clear from its origin of surface reaction and ion aggregation. To some extent, it exhibits flow patterns similar to ACEO flow. However, the high frequency (100 kHz) applied and the

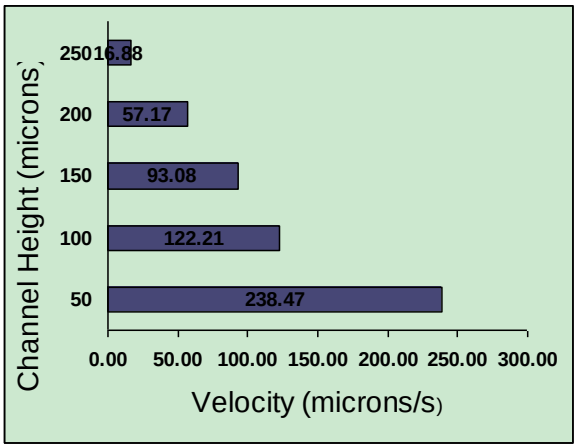

Figure 6-7 Velocity data taken at different channel height. Experiment conditions: 7.07Vrms, 100kHz AC voltage with -2V dc bias in conductive solution $\sigma = 0.08 S/m$.

conductive solution (0.08 S/m) rules out the possible involvement of ACEO in play.

We have used Comsol Multiphysics to simulate the dc bias scenario. The results qualitatively show the ability of bias voltage to create a fluid flow in much stronger magnitude. Two small regions (with height of ~1 micron) on top of electrodes are assigned with a higher conductivity value compared with its adjacent fluid surroundings. Variation of current readings on a resistor in series with fluid system indicates the change in local fluid conductivity near surface. The actual values of $\nabla\sigma$ are approximated from the equation $\nabla J = \nabla\sigma \cdot E$ if we assume the field strength remains constant due to fast fluid flows. The fluid conductivity is set as $\sigma = 2e^{-4} S/m$ (DI water) and the AC signal is 7Vrms, 80 kHz. The ratio $\frac{\nabla\sigma}{\sigma}$ is approximated to be at the order of 1 in simulation models. The control group is shown in Fig 6-8 (a) without the dc bias, i.e., no conductivity jump near electrodes. Summaries of simulation results are given in Table 6-1.

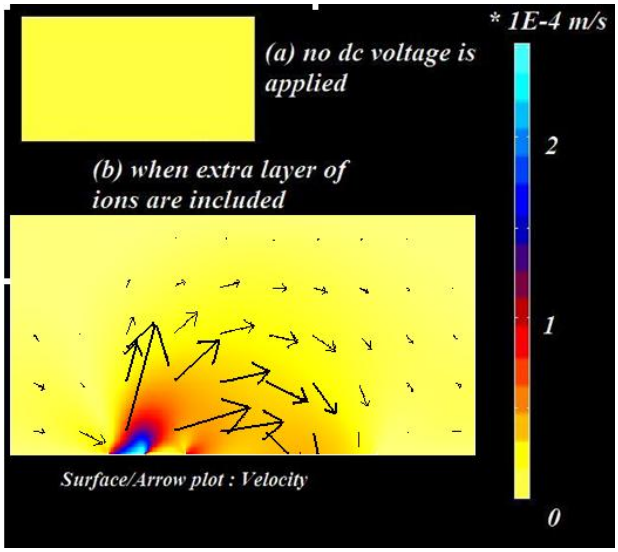

Figure 6-8 Simulation results show the comparison of pumping effect under the same velocity color scale.

Table 6-1 shows that the maximum velocity in biased simulation is about 300 times higher than the case when no DC voltage is applied (250 $\mu m/s$ VS 0.8 $\mu m/s$). The flow rate is 100 times higher ($2.2e^{-5}$ m^2/s VS $1.6e^{-7}m^2/s$). Given the temperature field are almost identical in two cases (maximum temperature rise is 0.04K and temperature gradient is 5954 K/m), the simulation qualitatively supports with our theory that the conductivity disturbance caused by faradaic current enhances the ACET force and leads to fast micropumping.

6.4 Summary

This chapter describes a novel reaction enhanced ACET micropumping approach. The method can be applied to both non-conductive and conductive solution with enhanced pumping velocity up to one order of magnitude. The extent of chemical reaction is controllable via monitoring dc bias so that the defects of electrolysis can be

	ACET	DC biased ACET
Electric field strength (V/m)	5.11E+06	5.15E+06
Temperature (K)	300.04	300.04
Temperature gradient (K/m)	5951.47	5954.62
Maximum velocity (m/s)	8.86E-07	2.52E-04
Flow rate (m2/s)	1.60E-07	2.20E-05

Table 6-1 Summaries of simulation results

avoided. The gold electrodes we used in experiments are highly polarizable. Such a property sets up an opening threshold potential for the onset of faradaic reaction. Diluted solution is more favorable to produce extra amount of ions due to faradaic currents than concentrated medium, and therefore, achieves better pumping performances. The fast pumping speed to the order of mm/s is not commonly seen in ACET manipulations for voltages less than 10V. Such a method provides a prospective future to be applied in real time pumping applications.

Chapter 7. Conclusion and Future Work

7.1 Conclusion

This dissertation focuses on one of the electrokinetic mechanisms-- the AC electrothermal effect for fluid manipulation in microfluidic devices. Microfluidic handling approaches by electrokinetic means are taking over the research attention from regular mechanical designs for its simplicity, high efficiency with low power consumption and easy-to-implement. Effective fluid manipulation by current ACEO technique is limited to fluids with low ionic strength (typically lower than tap water) [82][83]. The goal of this ACET research is to extend the application scope of microfluidic electrokinetics to fluids with no restriction in conductivities.

The interactions between fluids and electric fields were first studied in this dissertation. The surface effects distinct electrokinetics from regular mechanical approaches. The fluidic system exhibits resistive or capacitive behavior from the capacitive charging in double layer and its competition with resistive fluid bulk. The actual response depends on many factors including fluid conductivity, operating frequency, surface integrity and electrode designs. With embedded particles or cells, force exerts on such solid substances, adding another layer of complexity to fluid motion analysis. An equivalent circuit is then derived in chapter 2 so that impedance spectra of fluid system are used to access the relative importance of each component. This approach helps us understand the reason behind experiment observation.

Research of ACET effect is inspired by the increasing requirement of bio-sample manipulation in recent years. Applications of ACET in micropumping and particle trapping with the combining of experimental and numerical analysis were rarely seen

prior to this work. The results to these topics are presented in Chapter 3. The solutions used in these experiments have conductivities close to those in bio-samples. ACET mechanism is proved to be effective in fluidic handling at proper frequencies and particle trapping due to viscosity[84][85][86]. Considerable flow velocities at the order of hundred microns per second were recorded in our experiments at low voltages (<10Vrms). The numerical analysis using finite element methods add to the experiment results and show match in flow patterns and fluid velocities. In chapter 4, the impedance analysis with respect to face-to-face particle trapping device is conducted with extracted component values. We quantitatively compare the magnitude of other forces which might be possible to induce fluid flow. These forces include ACEO, DEP, buoyancy, Brownian motion and gravity. They are all ruled out because of negligible influence to the observed flow, leaving ACET to be the only responsible mechanism for micropumping and particle trapping. Moreover, the quartic relationship between ACET velocity and applied potential is first time reported in our research, further confirming ACET induced flow.

The research of ACET effect in conductive solutions is augmented by application on less conductive media such as deionized water and tap water in chapter 5. The flow reversal in symmetric electrode system is however observed in our experiments. It only happens to the second least conductive solution we have tested. The conventional ACEO theory and explanations of flow reversal shows no resemblance of fluidic pattern to our case. By carefully examining the experiment conditions and impedance spectra, we found that the resistive component implied by lossy double layer charging is accountable for surface heating, which is usually ignored by community [87]. Heat is generated on surface/interface at the time of current flow. When fluid conductivity and frequency is

appropriate, the regular ACEO flow is weak, and surface heating takes dominance over the bulk heating. Direction of temperature gradient changes, then the flow is reversed. Calculated power consumption is higher at the surface than in the bulk for the reversal frequency only, proving the ACET reversal theory.

An enhancement of ACET pumping was discovered in chapter 6. The dc offset added to one part of paired electrode induces reaction, which causes the faradaic current flow and aggregation of charges near electrode surface. The conductivity gradient now primarily comes from this charge gathering process instead of temperature rise. The recorded velocity has an increase up to one order of magnitude. Qualitative discussions are given to several influential factors revealed in experiments. At different AC potentials, there are large differences in recorded velocity, which separates this approach from the dc injection pump. The influence of fluid conductivity is shown by less conductive solution favoring more from the faradaic current flow than saline solutions with higher concentration. Also there appears to be a threshold dc voltage beyond which the flow shows a much more violent pumping action. This is due to the over potential of polarizable gold electrode.

7.2 Plan of Future Work

There are two directions that are interesting for further ACET research.

- Microcooling using ACET

Development of IC industry has been following Moore's law towards further scaling down. Thermal issues in high performance ICs are a bottleneck for further developments.

Thus liquid cooling solutions are becoming necessary and electrokinetic micropumps are attractive candidate for integration into a microcooling system due to its easy fabrication and low cost.

ACET can be induced by external temperature gradient [47], which is abundant in cooling applications. Simulations in chapter 5 have demonstrated an enhancement of pumping velocity by applying external heat source. The heated IC chip would be an ideal source for such purposes. Moreover, the technique described in chapter 6 also causes much higher fluid flow by introducing a thin layer of extra charges near electrode surface. Therefore, the combination of these two methods is expected to generate velocity at mm/s level which is high enough to cause heat convection. A schematic is drawn below in order to illustrate this cooling idea (Fig 7-1). Asymmetric electrode patterns fabricated on ITO glass are used as the top boundary of channel. When applied biased ac voltage, faradaic current pass though the boundary letting more charges into the solution. At the same time, the effect of temperature gradient from bottom surface adds to the free charge generation. Together, a high pumping speed is expected with cooling of heated IC chips. Due to the small voltages applied to electrodes, the extra power consumption of this cooling device is expected to be at the range of mW.

- Comprehensive modeling of AC mechanisms

The two mechanisms, ACEO and ACET, have been introduced and compared in great detail in this dissertation. Upon our study, we figured that in many cases, two mechanisms co-exist when an ac potential is applied to a fluidic chamber and together contribute to the fluid flow. The dominance is dependent to operating conditions and fluid properties. Therefore, it is desirable to build a comprehensive numerical model

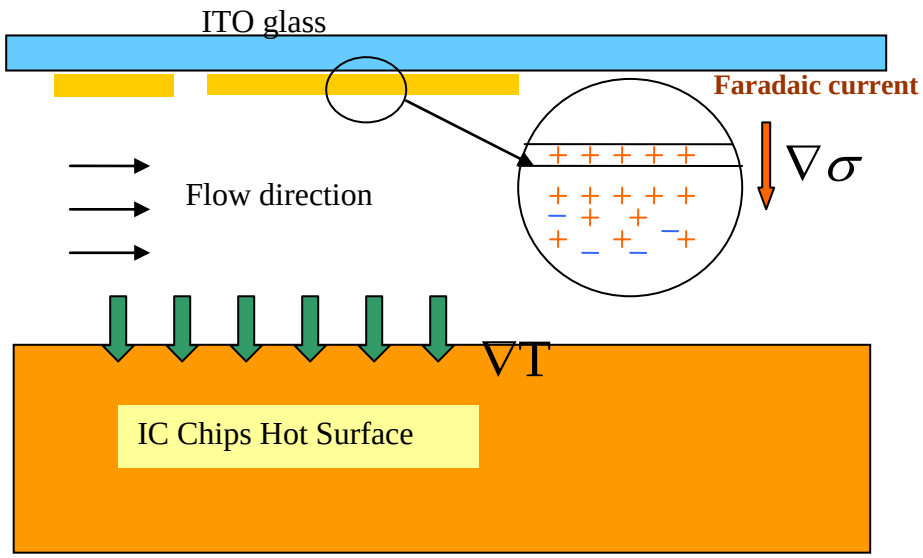

Figure 7-1Schematics of the microcooling plan

which accounts for both mechanisms, with considerations of possible influential factors such as frequency related impedance variation, surface heating or DEP force. Such a model would provide a comprehensive view of fluidic motion and assessment of individual force magnitude. This dissertation has laid the basis for numerical simulation of ACEO and ACET models alone. The combination of these two would set up a decent guideline for flow prediction in microchannels.

The preliminary simulation results of ACEO have been shown in our previous publications [36] (Fig 7-2). The flow pattern in streamline (Fig 7-1a) indicates four swirling vortices in a symmetric electrode system. Particle line formation as experimentally observed (Fig 7-1b) are shown by the stagnation points in simulation model. This model used a simplified ACEO velocity equation. Zeta potential is considered to be proportional to the normal electric field on surface. In the future plan, zeta potential is to be estimated from Eq (4-5). The component values in equivalence circuit can be derived from impedance analysis. Also, fixed electric potential is applied to

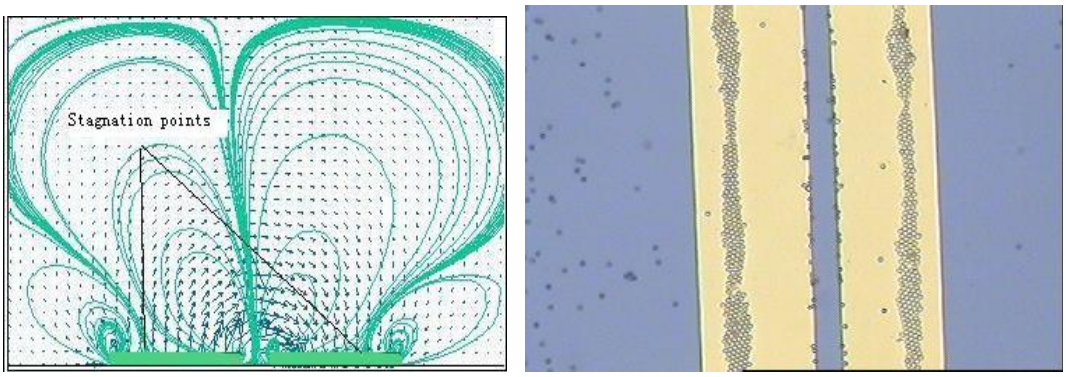

Figure 7-2 ACEO induced fluid flow in a symmetric electrode system (a) Simulation results (b) Experimentally observed two particle line formation on surface

electrode in Fig (7-1), which results in large tangential field component at both ends of electrode and zero for rest of the electrodes. In real, surface charge distribution on electrodes is not even. Charges closer to field maxima are more strongly attracted by electrostatic force than those far away from the highest field point. The variation in tangential field component on surface is expected. A more elaborate model will take this into account.

Reference

[1] A. Nisar, N. Afzulpurkar, B. Mahaisavariya, A. Tuantranont, "MEMS-based micropumps in drug delivery and biomedical applications", Sensors and Actuators B, 2008, 130, pp917-942

[2] V. Studer, A. Pepin, Y. Chen and A. Ajdari, "An integrated AC electrokinetic pump in a microfluidic loop for fast tunable flow control," Analyst, 2004, Vol. 129, pp. 944-949.

[3] B. M. Boyd, J. M. Prausnitz, H. W. Blanch, "High-frequency alternating-crossed-field gel electrophoresis with neutral or slightly charged interpenetrating networks to improve DNA separation", Electrophoresis, 2005, pp 3137-3148.

[4] T. Hermann, G. Wersch, E. Uhlemann, R Schmid, A. Burkovski, "Mapping and identification of Corynebacterium glutamicum proteins by two-dimensional gel electrophoresis and microsequencing", Electrophoresis, 2005, pp 3217-3221

[5] N. T. Nguyen, X. Huang, T. K. Chuan, "MEMS-micropumps: A Review", Journal of Fluids Engineering, Vol 124, 2, pp 384-393

[6] D. J. Laser, J. G. Santiago, "A review of micropumps", J Micromichine Microengineering, 2004, 14(6) pp 35-64

[7] B. D. Iverson, S. V. Garimella, "Recent advances in microscale pumping technologies:

a review and evaluation", Microfluidcs and Nanofluidics, 2008, 5(2), pp 145-172

[8] C. H. Ahn, M. G. Allen, "Fluid micropumps based on rotary magnetic actuators", Proc of IEEE Micro Electro Mechanical Systems (MEMS), 1995, pp 408-412

[9] http://www.rit.edu/research/research_highlights.php?s=15

[10] Y. S. Kim, J. H. Kim, K. H. Na, K. Rhee, "Experimental and numerical studies on the performance of a phlydimethylsiloxane valveless micropump", Proc Inst Mech Eng, Journal of Mech Eng Sci, 2005, 219(10), pp1139-1145

[11] A. Doll, M. Heinrichs, F. Goldschmidtboeing, H. J. Schrag, U. T. Hopt, P. Woias, " A high performance bidirectional micropump for a novel artificial sphincter system", Sensors & Actuators A, 2006, 130-131, pp 445-453.

[12]T. T. Nguyen, N. S. Goo, Y. S. Yoon, K. J. Yoon, "A novel lightweight piezo-composite actuator micropump", Proc of SPIE, 2006, San Diego, vol 6172, pp 617712.

[13]H. T. G. Van Lintel, F. C. M. Van De Pol, S. Bouwstra, "A piezoelectric micropump based on micromachining of silicon", Sens. Actuators, 1988, Vol15, pp153-167

[14]C. Cabuz, W. R. Herb, E. I. Cabuz, S. L. Lu, "The dual diaphragm pump", Proc of

IEEE Micro Electro Mechanical Systems (MEMS), 2001, pp 519-522

[15]T. Bourouina, A. Bossebuf, J. P. Grandchamp, “Design and simulation of an electrostatic micropump for drug-delivery applications”, J. Micromech. Microeng. 1997, Vol 10, pp 186-188

[16]S. Bohm, W. Olthuis, P. Bergveld, “A plastic micropump constructed with conventional techniques and materials”, Sens, Actuators, 1999, Vol A 77, pp 223-228

[17]A. Wego, H. W. Glock, L. Pagel, S. Richter, “Investigations on thermo-pneumatic volume actuators based on PCB technology”, Sens. Actuators, 2001, Vol A 93, pp 95-102

[18]J. G. Smits, “Piezoelectric micropump with three valves working peristaltically”, Sens. Actuators, 1990, Vol A21, pp 203-206

[19]T. K. Jun, C. J. Kim, “Valveless pumping using traversing vapor bubbles in microchannels”, J. Appl. Phys, 1998, Vol 83, pp 5658-5664

[20] K. S. Yun, I. J. Cho, J. U. Bu, G. H. Kim, Y. S. Jeon, C. J. Kim, E. Yoon, “A micropump driven by continuous electrowetting actuation for low voltage and low power operations”, Proc of IEEE Micro Electro Mechanical Systems (MEMS), 2001, pp 487-490

[21]V. Namsivayam, H. Kalyan, D. T. Burke, R. G. Larson, M. A. Burns, "Microfabricated valveless pump for delivering non-pulsatile flow", 2000, Proc of SPIE, Vol 4177, pp 220-228

[22]S. K. Cho, H. J. Moon, C. J. Kim, "Creating, transporting, cutting, and merging liquid droplets by electrowetting-based actuation for digital microfluidic circuits", J. Microelectromech, Syst. 2003, Vol 12, pp 70-74

[23]M. G. Pollack, A. D. Shenderov, R. B. Fair, "Electrowetting-based actuation of droplets for integrated microfluidics", Lab Chip, 2002, Vol 2, pp 96-101

[24]P. Paik, V. K. Pamula, M. G. Pollack, R. B. Fair, "Electrowetting-based droplet mixers for microfluidic systems", Lab Chip, 2003, Vol 3, pp 28-33

[25] http://www.devicelink.com/mdt/archive/07/05/001.html

[26] S. Zeng, C. H. Chen, J. C. Mikkelsen Jr., J. G. Santiago, "Fabrication and characterization of electroosmotic micropumps". Sensors Actuat. B, 2001, vol 79, pp 107-114.

[27] C. H. Chen, J. G. Santiago, "A planar electroosmotic micropump", Journal of Microelectromech System, 2002. vol 11. pp 672-683

[28]A. B. D. Brown, C. G. Smith, A. R. Rennie, “Pumping of water with ac electric fields applied to asymmetric pairs of microelectrodes”, Physical Review E, 2000, Vol 63, 016305

[29]M. Mpholo, C. G. Smith, A. B. D. Brown, “Low voltage plug flow pumping using anisotropic electrode arrays”, Sens Actuators B, 2003, Vol 92, pp 262-268

[30] P. G. Sanchez, A. Ramos, N. G. Green, H. Morgan, “Experiments on pumping of liquids using arrays of microelectrodes subjected to travelling wave potentials”, Electrostatics, 2007, 142, 012055

[31]A. Ramos, H. Morgan and N. G. Green, A. González, A. Castellanos, “Pumping of liquids with traveling-wave electroosmosis,” J. Appl. Phys. Vol. 97, 084906, 2005.

[32]M. Z. Bazant, Y. Ben, “Theoretical prediction of fast 3D AC electro-osmotic pumps”. Lab on a chip. Vol 6. 2006, pp1455-1461

[33]J. P. Urbanski, T. Thorsen, J. A. Levitan and M. Z. Bazant, “Fast AC electro-osmotic pumps with non-planar electrodes”, Applied Physics Letters. Vol 89. 2006, 143508

[34] W. Y. Ng, Y. C. Lam, L. Rodriguez, “ Experimental verification of faradaic charging in ac electrokinetics”, Biomicrofluidics, 2009, 3, 022405

[35]J. Wu, “Electrokinetic Microfluidics for On-Chip Bioparticle Processing,” *IEEE Trans. Nanotech*., 2006, **5**(2), pp. 84-89

[36]M. Lian, N. Islam and J. Wu, “Particle Line Assembly/Patterning by Microfluidic AC electroosmosis,” *J. Phys.: Conf. Series*, 2006, 34, pp. 589 – 594.

[37] A. Richter, H. Sandmaier, “An electrohydrodynamic pump”, IEEE MEMS, 1990, pp 99-104

[38] S. H. Ann, Y. K. Kim, “Fabrication and experiment of a planar micro ion drag pump”, Sensors and actuators A, Vol 70, 1998, pp 1-5

[39] J Darabi, M. Rada, M. Ohadi, J. Lawler, “Design, fabrication and testing of an electrohydrodynamic ion-drag micropump”, Journal of MEMS, 2002, 11(6), pp 684-690

[40] J. Darabi, H. Wang, “Development of an electrohydrodynamic injection micropump and its potential application in pumping fluids in cryogenic cooling system”, Journal of MEMS, 2005, 14(4) , pp747-755

[41] D. E. Lee, S. Soper, W. Wang, “Fabrication of a microfluidic system with integrated electrochemical pump and valves”, Proc of SPIE, 2007, San Jose, vol 6465, pp 64659B.

[42] J. M. Wang, L.J. Yang, “ Electrohydrodynamic(EHD) micropumps with electrode

protection by parylene and gelatin", Tamkang Journal of Science and Engineering, 2005, Vol 8, pp 231-236

[43] S. Moghaddam, M. M. Ohadi, "Effect of electrode geometry on performance of an EHD thin-film evaporator", Journal of MEMS, 2005, 14(5), pp 978-986

[44] C. W. Lin, J. Y. Jang, "3D numerical micro-cooling analysis for an electrohydrodynamic micropump", Sensors Actuators A, 2005, 122 (1 SPEC ISS): pp 167-176

[45] A. Ramos, H. Morgan, N. G. Green, A. Castellanos. "AC electrokinetics: a review of forces in microelectrode struct*ures"*. Journal of Physics. D: Applied. Physics. Vol 31. pp 2338-2353.1998

[46] A. Castellanos, A. Ramos, A Gonzalez, N.G. Green and H. Morgan, "Electrohydrodynamics and dielectrophoresis in microsystems: scaling laws," J. Phys. D: Appl. Phys., 36, 2584-97, 2003.

[47]N. G. Green, A. Ramos, A. Gonzalez, A. Castellanos and H. Morgan, "Electric field induced fluid flow on microelectrodes: the effect of illumination," J. Phys. D: Appl. Phys. 33 (2000) L13–L17.

[48]G. Fuhr, T. Schnelle and B. Wagner, "Traveling wave-driven microfabricated

electrohydrodynamic pumps for liquids". J. Micromech. Microeng., 1994, Vol. 4, pp. 217-226.

[49] P. Woias, "Micropumps – past, progress, and future prospects", Sensors & Actuators B Chem, 2005, 105(1), pp 28-38

[50]A. Gonzalez, A. Ramos, H. Morgan, N. Green, A. Castellanos, "Electrothermal flows generated by alternating and rotating electric fields in Microsystems". J. Fluid Mechanics. Vol. 564, 2006, pp 415-433.

[51] H. C. Feldman, M. Sigurdson, C. D. Meinhart, "AC Electrothermal enhancement of heterogeneous assays in microfluidics", Lab on a chip, 2007, 7, pp 1553-1559

[52] W. Y. Ng, S. Goh, Y. C. Lam, C. Yang, I. Rodriguez, " DC biased AC-electroosmotic and AC-electrothermal flow mixing in microchannels", Lab on a chip, 2009, 9, 802-809

[53] E. Gileadi, "Interfacial electrochemistry", Addison Wesley, 1975

[54] P. Dutta, A. Beskok, T. C. Warburton, "Electroosmotic flow control in complex microgeometries", Journal of MEMS, 2002, Vol 11, pp 36-44

[55] N. G. Green, A. Ramos, A. Gonzalez, H. Morgan, A. Castellanos, "Fluid flow

induced by nonuniform ac electric fields in electrolytes on microelectrodes. III. Observation of streamlines and numerical simulation", Physical review E. 2002, 66 026305

[56]A. Gonzalez, A. Ramos, N. G. Green, A. Castellanos, H. Morgan, "Fluid flow induced by nonuniform ac electric fields in electrolytes on microelectrodes, II. A linear double-layer analysis". Physical Review, 2001, Vol 61, 4, pp 4020-4028

[57] P. Mruetusatorn, M. R. Mahfouz and J. Wu, "Low voltage dynamic control for DE electro-osmotic micropumps," Sens. Actu. A, 2009, 153(2), pp. 237-243.

[58] M. Z. Bazant, Y. Ben, "Theoretical prediction of fast 3D AC electro-osmotic pumps", Lab on a chip, 2006, 6, 1455-1461

[59] M. Bazant, M. S. Kilic, B. D. Storey, A. Ajdari, " Towards an understanding of induced-charge electrokinetics at large applied voltages in concentrated solutions", ACIS, 2009, in press

[60]A. J. Stratton, Electromagnetic Theory (New York: McGraw Hill), 1941

[61]D. R. Lide. "CRD Handbook of chemistry and physics". *CRC press*, NY, 81st edn, 2000

[62] D. F. Chen, H. Du, “Simulation studies on electrothermal fluid flow induced in a dielectrophoretic microelectrode system”, Journal of MEMS, 2006, Vol 16, pp 2411-2419

[63]B. P. Cahill, L. J. Heyderman, J. Gobrecht, A. Stemmer, “Electroosmotic streaming on application of traveling-wave electric fields”, Physical Review E, 2004, Vol 70, 036305

[64]X. B. Wang, Y, Huang, X. J. Wang, F. F. Becker, P. R. C. Gascoyne, “Dielectrophoretic manipulation of cells with spiral electrodes”, Biophysical Journal, 1997, Vol 72, pp 1887-1899

[65] P. Kekicheff and B. W. Ninham, “ The double-layer interaction in asymmetric electrolytes”, Europhysics letters, Vol 12. 1990, pp471-477

[66] F. Fogolari, A. Brigo, H. Molinari, “The Poisson-Boltzmann equation for biomolecular electrostatics: a tool for structural biology”, Journal of Molecular Recognition, Vol 15, 2002, pp 377-392

[67] N. G. Green, A. Ramos, A. Gonzalez, H. Morgan, A. Castellanos, “ Fluid flow induced by nonuniform ac electric fields in electrolytes on microelectrodes. I. Experimental measurements”, Physical Review E, 2000, Vol 61, 4011-4018

[68] N. G. Green, A. Ramos, A. Gonzalez, A. Castellanos, H. Morgan, “Electrothermally induced fluid flow on microelectrodes”, J. Electrostatics, 2001, Vol 53, pp 71-87

[69] J. Wu, Y. Ben and H.-C. Chang, “Particle Detection by Micro- Electrical Impedance Spectroscopy with Asymmetric-Polarization AC Electroosmotic Trapping,” J. Microfluidics & Nanofluidics, 2005, 1(2), pp. 161-167.

[70] D. Lastochkin, R. Zhou, P. Wang, Y. Ben, and H. Chang, “Electrokinetic micorpump and micromixer design based on ac Faradaic polarization”, J. Appl. Phys., vol. 96, nr. 31, 2004

[71] K. Yang and J. Wu, “Investigation of Microflow Reversal by AC Electrokinetics in Orthogonal Electrodes for Micropump Design,” Biomicrofluidics, 2, 024101, 2008

[72] M. Gregersen, L. Olesen, A. Brask, M. Hansen, H. Bruus, “ Flow reversal at low voltage and low frequency in a microfabricated ac electrokinetic pump”, Physical Review, E76, 056305, 2007

[73] B. D. Storey, L. R. Edwards, M. S. Kilic, M. Z. Bazant, “Steric effects on ac electro-osmosis in dilute electrolytes”, Physical Review E, 2008, Vol 77, 036317

[74] M. S. Kilic, M. Z. Bazant, “Steric effects in the dynamics of electrolytes at large applied voltages. I. Double-layer charging”, Physical Review E, 2007, Vol 75, 021502

[75] I.R. Perch-Nielsen, N. G. Green, A. Wolff, "Numerical simulation of traveling wave induced electrothermal fluid flow", J. Phys, D: Appl. Phys, 2004, Vol 37, pp 2323-2330

[76] M. Lian, N. Islam and J. Wu, "Particle Line Assembly/Patterning by Microfluidic AC electroosmosis," Int'l MEMS Conf., May 9-12, 2006, Singapore, J. Phys.: Conf. Series, 2006, Vol 34, pp. 589 – 594.

[77] J. Wu, Y. Ben, D. Battigelli, and H. Chang, "Long-Range AC Electrokinetic Trapping and Detection of Bioparticles", Industr. Eng. Chem. Research, 2005, Vol 44(8), pp. 2815 – 2822.

[78] S Grimnnes, O. G. Martinsen, " Bioimpedance and bioelectricity basics", 2000

[79] J. Wu, "AC Electroosmotic Micropump by Asymmetric Electrode Polarization", J. Appl. Phys., 103, 024907, 2008.

[80] J. Wu, N. Islam, M. Lian, "High Sensitivity Particle Detection By Biased AC Electro-Osmotic Trapping on Cantilever," 19th IEEE Int'l Conf. Micro Electro Mechanical Systems (MEMS 2006), Jan. 22-26, Istanbul, Turkey, pp. 566 – 569.

[81] M. Lian, J. Wu, "Ultra Fast Micropumping by Biased AC Electrokinetics," Appl. Phys. Lett., Volume 94, Issue 6, id. 064101 . 2009

[82] N. Islam, M. Lian, J. Wu, R. Zhou, P. Wang and H.-C. Chang, "Bio/nano- particle Capture, Concentration and Detection by AC Electrokinetics," ORNL CNMS 2006 User Meeting, June 14-16, 2006, Oak Ridge, TN

[83] N. Islam, M. Lian, S. Swaminathan and J. Wu, "Micro/Nano- Particulate Fluid Manipulation in AC Electro-Kinetic Lab-on-a-Chip," 2nd ASM - IEEE EMBS Conf. Bio, Micro & Nanosyst., pp. 62-65, Jan. 15-18, 2006, San Francisco, CA, USA.

[84] M. Lian, N. Islam, J. Wu, "AC Electrothermal Manipulation of Conductive Fluids and Particles for Lab-chip Applications," IET Nanobiotechnology, 1(3), pp. 36-43. 2007.

[85] J. Wu, M. Lian, K. Yang, "Micropumping of Biofluids by AC Electrothermal Effects," Appl. Phys. Lett., 90, 234103, 2007.

[86] M. Lian, J. Wu, H.-Y. Jiang and H.-K. Yang, "Trapping and Manipulation of Nanoparticles by AC Electrothermal Effect in Laboratory-on-a-Chip Applications," J. Southeast Univ. (China), 2008

[87] M. Lian, J. Wu, "Microfluidic flow reversal at low frequency by AC electrothermal effect" J. Microfluidics & Nanofluidics , Vol 7, pp 757-765. 2009

[88] N. Islam, M. Lian, and J. Wu, “Enhancing Cantilever Capability with Integrated AC Electrokinetic Trapping Mechanism,” J. Microfluid & Nanofluid, 3(3), pp. 369-375, 2007.

VITA

Meng Lian received the B.S degree in Electrical Engineering from Chongqing University (CQU), Chongqing, China in June 2000. He continued his PHD study in the department of Electrical and Computer Engineering in the University of Tennessee after received his M.S degree there in August 2003. He is currently working as a PHD candidate student who expects to graduate in May 2010. He is also pursuing another M.S. degree in the department of statistics in the University of Tennessee and expects to finish in August 2010. His main research interest concentrates in the areas of microfluidics, Lab-on-a-chip design, MEMS system and applications towards biological and chemical problems. He has a good academic background and received CQU excellent student scholarship (1996,1998), Award of Excellent Undergraduate, the ChongQing University,2000 and Award of Extraordinary Professional Promises, The Univ of Tennessee, 2009.